IMAGING FEEDBACK FOR PULSED CAVITATIONAL ULTRASOUND THERAPY- HISTOTRIPSY

by

Tzu-Yin Wang

A dissertation submitted in partial fulfillment

of the requirements for the degree of

Doctor of Philosophy

(Biomedical Engineering)

In The University of Michigan

2011

Doctoral Committee:

Professor Charles A. Cain, Co-Chair

Associate Professor Cheri X. Deng, Co-Chair

Professor J. Brian Fowlkes

Associate Professor William W. Roberts

Assistant Professor Zhen Xu

To my family

ACKNOWLEDGMENTS

This thesis would not have been possible without the generous support, advice, inspiration, and encouragement from my advisor, colleagues, friends, and family.

I am heartily thankful to my advisor, Dr. Charles Cain, for his vision, wisdom, and guidance on my research. The “big pictures” Dr. Cain provided have kept me from getting lost in the day-to-day experiments, and directed me towards the completion of this thesis. More importantly, his enthusiasm and optimism have encouraged me to continue research in this field.

I would also like to thank my dissertation committee members, Drs. Cheri Deng, Brian Fowlkes, William Roberts, and Zhen Xu, for their willing to serve. I am grateful for their help not only at this final stage, but also through the years of my Ph.D. study.

I thank my colleagues and friends at the University of Michigan for the discussion and suggestions on the research and the enjoyable company. I’ve been very lucky to meet many wonderful people in the small cozy town. Among these people, I’d like to particularly thank Drs. Kim Ives, Tim Hall, Sheng-Wen Huang, Congxian Jia, Ron Kumon, Frank Winterroth, and the doctors-to-be: Zhenzhen Fan, Adam Maxwell, Ryan Miller, Yohan Kim, Kuang-Wei Lin, Alex Duryea, Simone Park, Eli Vlaisavljevich, and Steven Allen.

I am greatly indebted to my family. I thank them for raising me up with the deepest love, encouraging me to be brave and optimistic, and always being supportive no matter what.

Lastly, I'd like to acknowledge the funding from National Institutes of Health, the Hartwell Foundation, the Coulter Foundation, the Biomedical Engineering Department, and the Rackham Graduate School.

TABLE OF CONTENTS

LIST OF FIGURES

LIST OF TABLES

ABSTRACT

Histotripsy is a cavitational ultrasound therapy which mechanically fractionates soft tissue into subcellular debris using high intensity short ultrasound pulses. Histotripsy can be an effective tool for many clinical applications where non-invasive tissue removal is desired, including tumor therapy. For non-invasive tissue ablation therapy like histotripsy, image based feedback information allowing for accurate targeting, optimization of the on-going process, and prediction of the treatment efficacy in real time is the key to successful treatments.

The overall goal of this research is to develop image based feedback methods that can accurately predict the clinical outcomes during and after histotripsy treatments. To achieve this goal, the research was conducted in two stages.

In the first stage, new treatment strategies were investigated to produce homogeneous tissue fractionation. This ensures that feedback metrics obtained with any tissue characterization method are representative of the whole lesion instead of a misleading average of fully homogenized and non-homogenized zones. Specifically, two treatment strategies were developed. A focal zone sharpening technique, which limited the spatial extent of cavitation by preconditioning the cavitation nuclei in the surrounding area, was developed to create highly confined lesions with minimum scattered damage in the lesion boundaries. A cavitation memory removal strategy, which allowed for random

distribution of cavitation in response to each therapy pulse, was developed to produce homogeneously fractionated lesions with a dramatically reduced therapy dose.

In the second stage, three ultrasound image based methods were investigated to provide quantitative feedback information regarding the degree of tissue damage. These methods included ultrasound backscatter intensity analysis, ultrasound shear wave elasticity imaging, and characterization of shear wave propagation patterns. Strong correlations existed between the quantitative metrics derived from these methods and the degree of tissue fractionation as examined with histology, demonstrating the feasibility of using these metrics as quantitative feedback for histotripsy treatments.

In conclusion, this research demonstrates that histotripsy can be a highly controllable tissue ablation therapy via precise control of cavitation. Significant potential exists for histotripsy to be developed into an image-guided modality for noninvasive ultrasound tissue ablation therapy.

CHAPTER I. INTRODUCTION

1.1 Histotripsy: Cavitational Tissue Ablation Therapy

Acoustic cavitation induced by high intensity (peak negative pressure > 10 MPa) extremely short (< 50μs) ultrasound pulses at low duty cycles (<1%) has been shown to mechanically fractionate soft tissue in well-controlled manner [1-5]. This process results in soft tissue ('histo-') disruption ("-tripsy"), which has given rise to the term "histotripsy".

The causative agents of histotripsy are believed to be the energetic cavitation bubble clouds generated by ultrasound [6-11]. The micron-sized bubbles in the cloud act as "mini-scalpels" that fractionate the soft tissues into subcellular level, resulting in a highly homogenized volume with sharply demarcated boundaries [3, 4, 12]. The homogenized tissues remaining in the treatment volume appear to be "paste-like", which can be easily irrigated out to reveal a smooth cavity. In *in vivo* situations, the tissue homogenate can be reabsorbed by the body over time, leading to effective tissue removal [13]. Histotripsy produces precise, predictable, and effective local tissue fractionation in many *in vivo* models [14-19], demonstrating its potential for many clinical applications where non-invasive tissue removal is desired (e.g., treatments for benign prostatic hyperthermia).

1.2 Cavitation Nuclei Control for High Precision and Dose-efficient Treatments

For cavitation-based therapy, the initiation and maintenance of the cavitation process is highly affected by the small gas bubbles in a host medium that serve as nuclei for cavitation [20]. These nuclei may preexist in the host medium as gas pockets adhering to crevices on particles or stabilized with organic skin ("stabilized" nuclei). The nuclei may also form as fragments of bubbles that persist from collapse of transient cavities ("unstabilized" nuclei) [21-24]. The unstabilized nuclei may become new cavitation sites that sustain subsequent cavitation events, a phenomenon referred as the cavitation memory effect [21, 25-27].

Appropriate manipulation of the cavitation nuclei distribution allows for better control of the cavitation therapy. Various strategies have been proposed in the literature to enhance or suppress cavitation for desired treatment outcomes.

To enhance cavitation, artificial cavitation nuclei may be externally introduced to lower the cavitation threshold. This technique has been applied for applications, such as cell disruption, drug and gene delivery, etc [28-31]. Special insonation waveforms superimposing harmonic signals may be applied to further enhance cavitation activity [32, 33]. In lithotripsy or histotripsy where a large number of bubbles are generated in each pulse, advantages may be taken from the cavitation memory effect. For example, in lithotripsy, a second pulse may be delivered following the main pulse to induce more violent collapse of cavitation bubbles to improve the stone fragmentation efficiency in lithotripsy [34-38]. In histotripsy, low intensity pulses delivered after the high intensity

initiation pulses or interleaved between therapy pulses may sustain the cavitation process causing tissue erosion or fractionation [3, 39].

To suppress cavitation, overpressure may be applied to cause the dissolution of the cavitation nuclei. This approach prevents the unwanted cell or tissue injuries induced by shockwave lithotripsy [40-43]. The possible drawback of these approaches is global suppression of cavitation, which may cause less efficient treatments for target objects [40, 44]. To address this issue, local cavitation suppression is needed. The local cavitation suppression can be achieved either by injecting cavitation suppressing agents, as suggested by Kawabata *et al* [45], or by delivering specially designed insonation waveforms, as observed by Chapelon *et al* [46].

The concept of cavitation nuclei control is employed in this thesis to achieve two important treatment goals for histotripsy: 1) high-precision treatment where complete fractionation of the target tissue is achieved while scattered damage in the surrounding area is prevented; 2) dose-efficient treatment where homogeneous lesions are produced with minimum dose/energy.

High-precision treatment: Well-defined lesions with minimal collateral damage are important in many clinical applications, e.g., complete fractionation of the renal cancers while preserving the collecting system, or removing ablation of prostatic tissues while preserving the neurovascular bundles. Failure to protect the surrounding structures may lead to unwanted complications. An intuitive way to preserve the critical structures is to intentionally skip over those structures on treatment planning. For histotripsy, we further develop an active approach to "sharpen" the focal zone by actively

preconditioning the cavitation nuclei environment in the selected peripheral areas. As shown in the thesis, this approach results in complete fractionation in the treatment center with minimum damage in the surrounding areas.

Dose-efficient treatment: It has been observed that the inhomogeneous tissue fractionation with islands of intact tissues in the treatment volume may be produced when a small number of histotripsy pulses is applied [4, 47]. This phenomenon likely occurs as a downside of the cavitation memory effect. The cavitation memories, or the residual cavitation nuclei, likely accumulate in the same locations within the focal volume when the focal volume is repeatedly treated at high repetition rate. Because the spatial distribution of the cavitation nuclei may not be dense enough to cover the entire focal volume, the presence of the cavitation memory may result in over-treatment in the locations where the nuclei accumulated, and under-treatment in the rest areas. These islands of intact tissues could be detrimental for applications where complete tissue removal is desired (e.g., tumor therapy). Furthermore, when quantitative tissue characterization methods with ~mm spatial resolution (e.g., spectrum analysis [48] or elasticity imaging [49, 50]) are used to assess the treatment, a misleading metric may be produced as an average of fully homogenized and non-homogenized zones. Although this issue may be addressed by overdosing in the target volume, overdose may cause inefficient use of energy and prolonged treatment time. This thesis develops a dose-efficient strategy to achieve complete and homogeneous tissue fractionation by removing the cavitation memory, allowing for application of the imaging feedback metrics subsequently developed in this thesis.

1.3 Imaging Guidance and Feedback for Histotripsy

Image guidance and feedback information allowing accurate targeting, optimization of the on-going process, and predicting the treatment efficacy in real time is the key to successful treatments for non-invasive tissue ablation therapies. Being one of the non-invasive therapies, histotripsy has many favorable characteristics for development of image guidance and feedback strategies before, during, and after the treatments.

The causative agents of histotripsy, i.e., cavitation bubble clouds, serve as an inherent indicator for the treatment localization. These bubbles are strong ultrasound scatterers which appear as bright (hyperechoic) flickering spots on standard ultrasound B-mode images. They can be easily identified even in deep seated tissues, where image quality is substantially degraded due to attenuation in the overlying tissues. Their appearance ensures that the process is properly initiated and maintained.

The bubble clouds could also be useful for evaluation of the treatment efficacy via analysis of their dynamically changing patterns. The bubbles can be regarded as remotely induced contrast agents trapped in the tissues. Their motions or dynamics could be closely related to the tissue environment. For example, with increased mobility provided in a highly fractionated volume, the bubbles may migrate to different locations with the aid of acoustic radiation force from the therapy pulses. Therefore, increased spatial variability may be observed in the acoustic backscatter signals from the bubbles [51].

More direct measurement of the physical change in the tissue structures can be performed with various tissue characterization schemes. For example, the histotripsy

process may change the ultrasound scattering environment in the tissues as the fundamental scattering units (e.g., the cell nuclei, collagen, extracellular matrix, or functional tissue elements such as the glomerulus or renal tubules [52-58]) may be disrupted. This may result in substantial change in the backscatter intensity [12], or backscatter spectrum parameters related to the size and concentration of the scattering units [48]. In addition to damage to the fundamental unit, the histotripsy process may also disrupt the connective tissue structures, causing the lost of tissue restoration force and thus reduced tissue elasticity. Such change may be easily detected with ultrasound or MR elastography [49, 50, 59-63].

1.4 Contribution of Thesis

This overall goal of this thesis is to develop accurate imaging feedback metrics for accurate prediction of the clinical outcomes produced by histotripsy.

To achieve this goal, improved homogeneity of the lesions is needed. We first investigate a strategy that produces precise and well-defined lesions by locally suppressing cavitation in the periphery of the treatment focus. Such strategy produces lesions smaller than the natural size of the focal volume without sacrificing treatment efficiency in the center. Next, a strategy to produce homogeneous lesions with minimal dose is developed. Homogeneous lesions can be produced by removing the cavitation memory responsible for inhomogeneous fractionation. This strategy produces homogeneous lesions with a drastically lower dose compared to current treatments. The homogeneous and well-defined lesions produced with these two strategies allow for

accurate prediction of the treatment outcomes with the image-based tissue characterization methods subsequently developed in this thesis.

Three ultrasound image-based feedback approaches: 1) backscatter intensity analysis, 2) tissue elasticity imaging, and 3) shear displacement profile characterization, are developed in this thesis. The metrics derived from these methods can be quantitatively correlated to the degree of tissue fractionation as examined via histology. The strong correlations indicate that these metrics may provide feedback information regarding the treatment efficacy, allowing the prediction of local clinical outcomes, i.e. when a tissue volume has been sufficiently treated.

1.5 References

[1] Z. Xu, A. Ludomirsky, L. Y. Eun, T. L. Hall, B. C. Tran, J. B. Fowlkes, and C. A. Cain, "Controlled ultrasound tissue erosion," *IEEE Trans. Ultrason., Ferroelect., Freq. Contr.,* vol. 51, pp. 726-736, Jun 2004.

[2] K. Kieran, T. L. Hall, J. E. Parsons, J. S. Wolf, Jr., J. B. Fowlkes, C. A. Cain, and W. W. Roberts, "Refining histotripsy: defining the parameter space for the creation of nonthermal lesions with high intensity, pulsed focused ultrasound of the in vitro kidney," *J. Urol.,* vol. 178, pp. 672-676, Aug 2007.

[3] J. E. Parsons, C. A. Cain, G. D. Abrams, and J. B. Fowlkes, "Pulsed cavitational ultrasound therapy for controlled tissue homogenization," *Ultrasound Med. Biol.,* vol. 32, pp. 115-129, Jan 2006.

[4] W. W. Roberts, T. L. Hall, K. Ives, J. S. Wolf, Jr., J. B. Fowlkes, and C. A. Cain, "Pulsed cavitational ultrasound: a noninvasive technology for controlled tissue ablation (histotripsy) in the rabbit kidney," *J. Urol.,* vol. 175, pp. 734-738, Feb 2006.

[5] Z. Xu, J. B. Fowlkes, A. Ludomirsky, and C. A. Cain, "Investigation of intensity thresholds for ultrasound tissue erosion," *Ultrasound Med. Biol.,* vol. 31, pp. 1673-1682, Dec 2005.

[6] Z. Xu, J. B. Fowlkes, E. D. Rothman, A. M. Levin, and C. A. Cain, "Controlled ultrasound tissue erosion: the role of dynamic interaction between insonation and microbubble activity," *J. Acoust. Soc. Am.,* vol. 117, pp. 424-435, Jan 2005.

[7] Z. Xu, T. L. Hall, J. B. Fowlkes, and C. A. Cain, "Optical and acoustic monitoring of bubble cloud dynamics at a tissue-fluid interface in ultrasound tissue erosion," *J. Acoust. Soc. Am.,* vol. 121, pp. 2421-2430, Apr 2007.

[8] Z. Xu, T. L. Hall, J. B. Fowlkes, and C. A. Cain, "Effects of acoustic parameters on bubble cloud dynamics in ultrasound tissue erosion (histotripsy)," *J. Acoust. Soc. Am.,* vol. 122, pp. 229-236, Jul 2007.

[9] Z. Xu, M. Raghavan, T. L. Hall, C. W. Chang, M. A. Mycek, J. B. Fowlkes, and C. A. Cain, "High speed imaging of bubble clouds generated in pulsed ultrasound cavitational therapy--histotripsy," *IEEE Trans. Ultrason. Ferroelectr. Freq. Control,* vol. 54, pp. 2091-101, Oct 2007.

[10] Z. Xu, M. Raghavan, T. L. Hall, M. A. Mycek, J. B. Fowlkes, and C. A. Cain, "Evolution of bubble clouds induced by pulsed cavitational ultrasound therapy - histotripsy," *IEEE Trans. Ultrason. Ferroelectr. Freq. Control,* vol. 55, pp. 1122-32, May 2008.

[11] A. D. Maxwell, T. Y. Wang, C. A. Cain, J. B. Fowlkes, O. A. Sapozhnikov, M. R. Bailey, and Z. Xu, "Cavitation clouds created by shock scattering from bubbles during histotripsy," *J. Acoust. Soc. Am.,* 2011 (accepted).

[12] T. L. Hall, J. B. Fowlkes, and C. A. Cain, "A real-time measure of cavitation induced tissue disruption by ultrasound imaging backscatter reduction," *IEEE Trans. Ultrason., Ferroelect., Freq. Contr.,* vol. 54, pp. 569-575, Mar 2007.

[13] T. L. Hall, K. Kieran, K. Ives, J. B. Fowlkes, C. A. Cain, and W. W. Roberts, "Histotripsy of rabbit renal tissue in vivo: temporal histologic trends," *J. Endourol.,* vol. 21, pp. 1159-1166, Oct 2007.

[14] Y. Kim, S. K. Gelehrter, C. G. Fifer, J. C. Lu, G. E. Owens, D. R. Berman, J. Williams, J. E. Wilkinson, K. A. Ives, and Z. Xu, "Non-invasive pulsed cavitational ultrasound for fetal tissue ablation: feasibility study in a fetal sheep model," *Ultrasound Obstet Gynecol,* Nov 12 2010.

[15] A. D. Maxwell, G. Owens, H. S. Gurm, K. Ives, D. D. Myers, Jr., and Z. Xu, "Noninvasive treatment of deep venous thrombosis using pulsed ultrasound cavitation therapy (histotripsy) in a porcine model," *J Vasc Interv Radiol,* vol. 22, pp. 369-77, Mar 2010.

[16] G. E. Owens, R. M. Miller, G. Ensing, K. Ives, D. Gordon, A. Ludomirsky, and Z. Xu, "Therapeutic ultrasound to noninvasively create intracardiac communications in an intact animal model," *Catheter Cardiovasc Interv,* vol. 77, pp. 580-8, Mar 1 2010.

[17] Z. Xu, G. Owens, D. Gordon, C. Cain, and A. Ludomirsky, "Noninvasive creation of an atrial septal defect by histotripsy in a canine model," *Circulation,* vol. 121, pp. 742-9, Feb 16 2010.

[18] N. R. Styn, J. C. Wheat, T. L. Hall, and W. W. Roberts, "Histotripsy of VX-2 tumor implanted in a renal rabbit model," *J Endourol,* vol. 24, pp. 1145-50, Jul 2010.

[19] A. M. Lake, T. L. Hall, K. Kieran, J. B. Fowlkes, C. A. Cain, and W. W. Roberts, "Histotripsy: Minimally Invasive Technology for Prostatic Tissue Ablation in an In Vivo Canine Model," *Urology,* vol. 72, pp. 682-686, Mar 14 2008.

[20] T. G. Leighton, *The acoustic bubble*: Academic Press, 1997.

[21] H. G. Flynn and C. C. Church, "A mechanism for the generation of cavitation maxima by pulsed ultrasound," *J Acoust Soc Am,* vol. 76, pp. 505-12, Aug 1984.

[22] E. N. Harvey, D. K. Barnes, W. D. McElroy, A. H. Whiteley, D. C. Pease, and K. W. Cooper, "Bubble formation in animals. I. Physical factors," *J. Cell. Comp. Physiol.,* vol. 24, pp. 1-22, Aug. 1944 1944.

[23] F. E. Fox and K. F. Herzfeld, "Gas Bubbles with Organic Skin as Cavitation Nuclei," *J. Acoust. Soc. Am.,* vol. 26, pp. 984-989, 1954.

[24] E. N. Harvey, D. K. Barnes, W. D. McElroy, A. H. Whiteley, D. C. Pease, and K. W. Cooper, "Bubble formation in animals. II. Gas nuclei and their distribution in blood and tissues," *J. Cell. Comp. Physiol.,* vol. 24, pp. 23-34, Aug. 1944 1944.

[25] J. B. Fowlkes and L. A. Crum, "Cavitation threshold measurements for microsecond length pulses of ultrasound," *J Acoust Soc Am,* vol. 83, pp. 2190-201, Jun 1988.

[26] A. Henglein and M. Gutierrez, "Chemical reactions by pulsed ultrasound: memory effects in the formation of NO3- and NO2- in aerated water," *Int J Radiat Biol Relat Stud Phys Chem Med,* vol. 50, pp. 527-33, Sep 1986.

[27] O. Yavas, P. Leiderer, H. K. Park, C. P. Grigoropoulos, C. C. Poon, and A. C. Tam, "Enhanced acoustic cavitation following laser-induced bubble formation: Long-term memory effect," *Phys Rev Lett,* vol. 72, pp. 2021-2024, Mar 28 1994.

[28] E. C. Unger, E. Hersh, M. Vannan, T. O. Matsunaga, and T. McCreery, "Local drug and gene delivery through microbubbles," *Prog Cardiovasc Dis,* vol. 44, pp. 45-54, Jul-Aug 2001.

[29] D. L. Miller and R. M. Thomas, "Ultrasound contrast agents nucleate inertial cavitation in vitro," *Ultrasound Med Biol,* vol. 21, pp. 1059-65, 1995.

[30] W. J. Greenleaf, M. E. Bolander, G. Sarkar, M. B. Goldring, and J. F. Greenleaf, "Artificial cavitation nuclei significantly enhance acoustically induced cell transfection," *Ultrasound Med Biol,* vol. 24, pp. 587-95, May 1998.

[31] C. K. Holland and R. E. Apfel, "Thresholds for transient cavitation produced by pulsed ultrasound in a controlled nuclei environment," *J Acoust Soc Am,* vol. 88, pp. 2059-69, Nov 1990.

[32] S. Umemura, K. Kawabata, and K. Sasaki, "In vitro and in vivo enhancement of sonodynamically active cavitation by second-harmonic superimposition," *J Acoust Soc Am,* vol. 101, pp. 569-77, Jan 1997.

[33] S. D. Sokka, T. P. Gauthier, and K. Hynynen, "Theoretical and experimental validation of a dual-frequency excitation method for spatial control of cavitation," *Phys Med Biol,* vol. 50, pp. 2167-79, May 7 2005.

[34] M. Arora, L. Junge, and C. D. Ohl, "Cavitation cluster dynamics in shock-wave lithotripsy: part 1. Free field," *Ultrasound Med Biol,* vol. 31, pp. 827-39, Jun 2005.

[35] X. Xi and P. Zhong, "Improvement of stone fragmentation during shock-wave lithotripsy using a combined EH/PEAA shock-wave generator-in vitro experiments," *Ultrasound Med Biol,* vol. 26, pp. 457-67, Mar 2000.

[36] M. Delius and W. Brendel, "A model of extracorporeal shock wave action: tandem action of shock waves," *Ultrasound Med Biol,* vol. 14, pp. 515-518, 1988.

[37] A. M. Loske, F. E. Prieto, F. Fernandez, and J. van Cauwelaert, "Tandem shock wave cavitation enhancement for extracorporeal lithotripsy," *Phys Med Biol,* vol. 47, pp. 3945-57, Nov 21 2002.

[38] P. Huber, J. Debus, K. Jochle, I. Simiantonakis, J. Jenne, R. Rastert, J. Spoo, W. J. Lorenz, and M. Wannenmacher, "Control of cavitation activity by different shockwave pulsing regimes," *Phys Med Biol,* vol. 44, pp. 1427-37, Jun 1999.

[39] Z. Xu, J. B. Fowlkes, and C. A. Cain, "A new strategy to enhance cavitational tissue erosion using a high-intensity, initiating sequence," *IEEE Trans. Ultrason., Ferroelect., Freq. Contr.,* vol. 53, pp. 1412-1424, Aug 2006.

[40] M. R. Bailey, R. O. Cleveland, T. Colonius, L. A. Crum, A. P. Evan, J. E. Lingeman, J. A. McAteer, O. A. Sapozhnikov, and J. C. Williams, Jr., "Cavitation in shock wave lithotripsy: the critical role of bubble activity in stone breakage and kidney trauma," in *Proc. IEEE Ultrason. Symp.*, 2003, pp. 724-727.

[41] A. P. Evan, L. R. Willis, J. A. McAteer, M. R. Bailey, B. A. Connors, Y. Shao, J. E. Lingeman, J. C. Williams, Jr., N. S. Fineberg, and L. A. Crum, "Kidney damage and renal functional changes are minimized by waveform control that suppresses cavitation in shock wave lithotripsy," *J Urol,* vol. 168, pp. 1556-62, Oct 2002.

[42] J. A. McAteer, M. A. Stonehill, K. Colmenares, J. C. J. Williams, and A. P. Evan, "SWL cavitation damage in vitro: Pressurization unmasks a differential response of foil targets and isolated cells," in *J. Acoust. Soc. Amer.* vol. 103, 1998, p. 3038.

[43] O. A. Sapozhnikov, V. A. Khokhlova, M. R. Bailey, J. C. Williams, Jr., J. A. McAteer, R. O. Cleveland, and L. A. Crum, "Effect of overpressure and pulse repetition frequency on cavitation in shock wave lithotripsy," *J Acoust Soc Am,* vol. 112, pp. 1183-95, Sep 2002.

[44] M. Delius, "Minimal static excess pressure minimises the effect of extracorporeal shock waves on cells and reduces it on gallstones," *Ultrasound Med Biol,* vol. 23, pp. 611-7, 1997.

[45] K. Kawabata, K. Sasaki, and S. Umemura, "Agents promoting and suppressing acoustic cavitation," in *Proc. IEEE Ultrason. Symp.*, 1998, pp. 1443 - 1446.

[46] J. Y. Chapelon, F. Dupenloup, H. Cohen, and P. Lenz, "Reduction of cavitation using pseudorandom signals," *IEEE Trans. Ultrason., Ferroelect., Freq. Contr.,* vol. 43, pp. 623-625, 1996.

[47] T.-Y. Wang, Z. Xu, F. Winterroth, T. L. Hall, J. B. Fowlkes, E. D. Rothman, W. W. Roberts, and C. A. Cain, "Quantitative Ultrasound Backscatter for Pulsed Cavitational Ultrasound Therapy - Histotripsy," *IEEE Trans. Ultrason. Ferroelectr. Freq. Control.,* vol. 56, pp. 995-1005, 2009.

[48] F. L. Lizzi, M. Greenebaum, E. J. Feleppa, M. Elbaum, and D. J. Coleman, "Theoretical framework for spectrum analysis in ultrasonic tissue characterization," *J. Acoust. Soc. Amer.,* vol. 73, pp. 1366-1373, Apr. 1983.

[49] K. Nightingale, M. S. Soo, R. Nightingale, and G. Trahey, "Acoustic radiation force impulse imaging: in vivo demonstration of clinical feasibility," *Ultrasound Med Biol,* vol. 28, pp. 227-35, Feb 2002.

[50] L. Sandrin, M. Tanter, S. Catheline, and M. Fink, "Shear modulus imaging with 2-D transient elastography," *IEEE Trans Ultrason Ferroelectr Freq Control,* vol. 49, pp. 426-35, Apr 2002.

[51] J. E. Parsons, C. A. Cain, and J. B. Fowlkes, "Spatial variability in acoustic backscatter as an indicator of tissue homogenate production in pulsed cavitational ultrasound therapy," *IEEE Trans. Ultrason., Ferroelect., Freq. Contr.,* vol. 54, pp. 576-590, Mar 2007.

[52] M. O'Donnell, J. W. Mimbs, and J. G. Miller, "Relationship between collagen and ultrasonic backscatter in myocardial tissue," *J Acoust Soc Am,* vol. 69, pp. 580-8, Feb 1981.

[53] J. W. Hunt, A. E. Worthington, A. Xuan, M. C. Kolios, G. J. Czarnota, and M. D. Sherar, "A model based upon pseudo regular spacing of cells combined with the randomisation of the nuclei can explain the significant changes in high-frequency ultrasound signals during apoptosis," *Ultrasound Med Biol,* vol. 28, pp. 217-26, Feb 2002.

[54] M. C. Kolios, G. J. Czarnota, M. Lee, J. W. Hunt, and M. D. Sherar, "Ultrasonic spectral parameter characterization of apoptosis," *Ultrasound Med Biol,* vol. 28, pp. 589-97, May 2002.

[55] R. E. Baddour, M. D. Sherar, J. W. Hunt, G. J. Czarnota, and M. C. Kolios, "High-frequency ultrasound scattering from microspheres and single cells," *J Acoust Soc Am,* vol. 117, pp. 934-43, Feb 2005.

[56] A. S. Tunis, G. J. Czarnota, A. Giles, M. D. Sherar, J. W. Hunt, and M. C. Kolios, "Monitoring structural changes in cells with high-frequency ultrasound signal statistics," *Ultrasound Med Biol,* vol. 31, pp. 1041-9, Aug 2005.

[57] C. C. S. Hall, M. M. J. Scott, G. G. M. Lanza, J. J. G. Miller, and S. S. A. Wickline, "The extracellular matrix is an important source of ultrasound backscatter from myocardium," *The Journal of the Acoustical Society of America,* vol. 107, pp. 612-9, 2000.

[58] M. M. F. Insana, T. T. J. Hall, and J. J. L. Fishback, "Identifying acoustic scattering sources in normal renal parenchyma from the anisotropy in acoustic properties," *Ultrasound in medicine & biology,* vol. 17, pp. 613-26, 1991.

[59] K. J. Parker, S. R. Huang, R. A. Musulin, and R. M. Lerner, "Tissue response to mechanical vibrations for "sonoelasticity imaging"," *Ultrasound Med Biol,* vol. 16, pp. 241-6, 1990.

[60] J. Ophir, I. Cespedes, H. Ponnekanti, Y. Yazdi, and X. Li, "Elastography: a quantitative method for imaging the elasticity of biological tissues," *Ultrason Imaging,* vol. 13, pp. 111-34, Apr 1991.

[61] M. O'Donnell, A. R. Skovoroda, B. M. Shapo, and S. Y. Emelianov, "Internal displacement and strain imaging using ultrasonic speckle tracking," *IEEE Trans Ultrason Ferroelectr Freq Control,* vol. 41, pp. 314-325, 1994.

[62] R. Muthupillai, D. J. Lomas, P. J. Rossman, J. F. Greenleaf, A. Manduca, and R. L. Ehman, "Magnetic resonance elastography by direct visualization of propagating acoustic strain waves," *Science,* vol. 269, pp. 1854-7, Sep 29 1995.

[63] T. A. Krouskop, T. M. Wheeler, F. Kallel, B. S. Garra, and T. Hall, "Elastic moduli of breast and prostate tissues under compression," *Ultrason Imaging,* vol. 20, pp. 260-74, Oct 1998.

CHAPTER II. ACTIVE FOCAL ZONE SHARPENING FOR HIGH PRECISION TREATMENT USING HISTOTRIPSY

2.1 Introduction

The goal of this chapter is to develop a focal zone sharpening strategy that produces highly confined lesions compared with the natural size of the focal zone without sacrificing the treatment efficiency. Our previous studies have suggested that the bubble clouds generated by histotripsy pulses are the causative agents of the mechanical tissue disruption [1-6]. Thus, the size and shape of the lesions matches well with the dimensions of the bubble clouds [7]. In most clinical applications, bubbles cloud with the dimensions matching with those of the focal zone can produce fairly precise lesions. In some specific applications (e.g., fetal surgery), the target volume can be smaller than the natural size of the focal zone. This requires treatments with higher precision treatment. Since the bubble dimensions match well with the lesion dimensions, we hypothesize that highly confined lesions may be produced by limiting the spatial extent of the cavitation bubble clouds. This may be achieved using local cavitation suppression in the periphery of the focus.

Various schemes have been proposed to suppress excess cavitational damage in cavitation-based therapies. Willis *et al* have found that, in lithotripsy, the protection of a local selected area is possible by delivering several pretreatment low-intensity

shockwaves [8]. Using this strategy, the renal damage produced by shockwave lithotripsy can be significantly reduced. The mechanism is hypothesized to be physiologic, i.e., vasoconstriction triggered by the low-intensity shockwaves. Other researchers have demonstrated that application of overpressure or time reversed waveform may suppress the cavitation bubble activity, thus reducing cell or tissue injuries induced by shockwave lithotripsy [9-12]. The possible drawback of these approaches is global suppression of cavitation, which may cause less efficient treatments for target objects [9, 13]. To address this issue, local suppression of cavitation is necessary. The local suppression of cavitation may be achieved either by injecting cavitation suppressing agents, as suggested by Kawabata *et al* [14], or by delivering specially designed insonation waveforms, as observed by Chapelon *et al* [15].

We propose a strategy for focal zone sharpening, where cavitation in the periphery of the focus may be suppressed using cavitation nuclei preconditioning. Since cavitation depends on a distribution of appropriately sized cavitation nuclei [16, 17], it is plausible that cavitation may be actively suppressed by altering the cavitation nuclei distribution. Our unpublished work shows that the distribution of the cavitation nuclei (possibly the microbubbles persisting from previous therapy pulses [18, 19]) may be changed using histotripsy pulses at a reduced intensity. Based on this observation, we propose a concurrent spatial-temporal pulsing strategy for focal zone sharpening. An ultrasound pulse is delivered to the periphery of the focus prior to each therapy pulse. This pulse is hypothesized to precondition the cavitation nuclei such that cavitation may be locally suppressed in the periphery.

In this chapter we investigated the feasibility of focal zone sharpening using the proposed pulsing strategy. We first explored effective pulse parameters by which complete damage in the focal center and minimum damage in the peripheral region occurred. To study effects of nuclei preconditioning on the spatial extent of cavitation, the cavitating bubble clouds generated with and without nuclei preconditioning were observed using high speed photography. Experiments were performed both in red blood cell (RBC) phantoms and *ex vivo* livers. The former allowed for rapid evaluation of the effective pulse parameters; the latter provided validation in real tissues. The focal zone sharpening technique could have significant clinical applications where a target tissue is to be disrupted while the critical structures immediately adjacent to it are preserved.

2.2 Materials and Methods

2.2.1 Cavitation damage indication phantom preparation

Cavitational damage indication phantoms consisted of a thin (< 1 mm) RBC-gel layer suspended in between two 2-cm-thick transparent gel layers. The phantoms were prepared using a mixture of high-clarity low-gelling-temperature agarose powder (Type-VII, Sigma-Aldrich, St. Louis, MO) and canine RBCs in 0.9% isotonic saline. Canine blood was obtained from healthy adult subjects and preserved with an anticoagulant solution (citrate-phosphate-dextrose C1765, Sigma-Aldrich, St. Louis, Missouri, USA) at 4ºC. The RBCs were extracted from the whole blood prior to the preparation of the phantoms. The agarose powder was mixed with saline at a 1% w/v concentration, and heated until the agarose powder completely melted. The solution was placed in a vacuum

chamber for 20 minutes to remove excess air bubbles in the solution. After air bubbles were removed, a 2-cm layer of agarose solution was poured in a 13 cm (width) × 7.5 cm (length) × 4 cm (height) polycarbonate holder which had a thin optically and acoustically transparent polyester membrane on the bottom. The holder was stored at 4ºC to allow the agarose layer to solidify. A small volume of agarose solution was taken from the remaining solution, and the RBCs were mixed in this volume using 5% v/v concentration at 42ºC. A thin layer of the RBC-gel solution was uniformly deposited onto the bottom layer. After the RBC-gel layer solidified, the remaining agarose solution was poured to completely fill the holder. More details on the RBC phantom are described in [7].

2.2.2 Experimental setup

The experimental setup is shown in **Figure II-1**. A 1-MHz 513-element 2-D therapeutic phased array transducer (Imasonic, Voray sur l'Ognon, France) was used to generate both the therapy and preconditioning pulses. The 2-D phased array is a 145 mm diameter section of a spherical shell, and has a 150 mm geometric focal length and a 50 mm diameter hole in the center (**Figure II-2a**).

Before experimentation, the geometric focus of the therapeutic array was located using a field scan with a custom-built fiber optic probe hydrophone (FOPH) [20]. The fiber tip was placed at the geometric focus after the field scan. Two 1-mm-wide 5-mW laser beams were generated using laser diode modules (Calpac lasers, Steamboat Springs, CO). The two laser beams, one along and the other perpendicular to the ultrasound beam, were placed to cross at the tip of the FOPH, indicating the geometric focus of the

therapeutic array. The FOPH was then removed from the tank. The location of the geometric focus was confirmed by generating bubble clouds at the cross-section of the two lasers with a brief excitation of the transducer. After locating the geometric focus, the RBC phantom was placed in the tank such that the RBC-gel layer was perpendicular to the ultrasound beam. Multiple treatments were performed in a single RBC phantom. Each lesion was generated using multiple pulses delivered to a single focal location. The spacing between the adjacent lesions was at least 10 mm in order to avoid interference from different treatments.

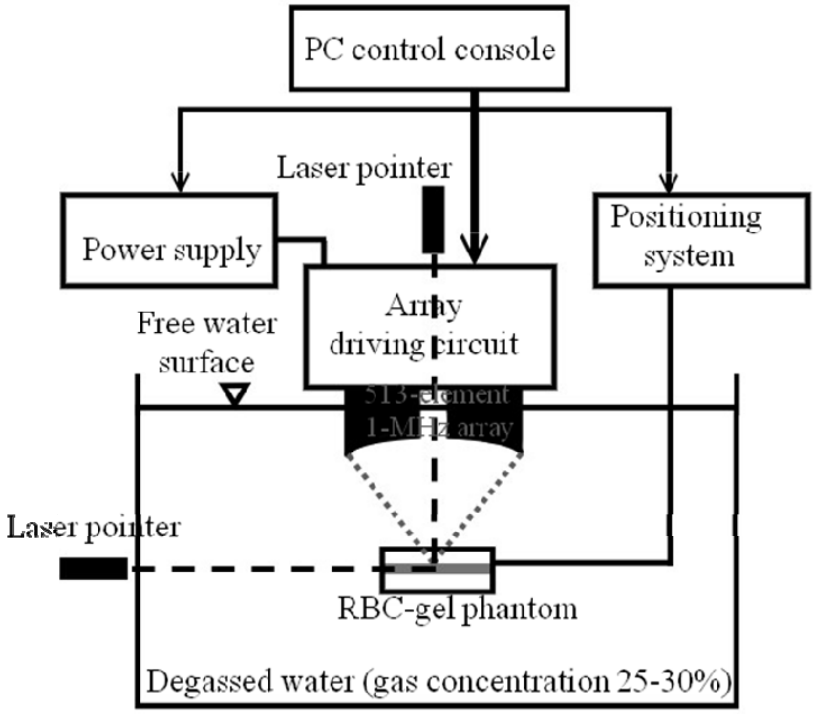

Figure II-1: Experimental setup. The 513-element therapeutic array and the motorized positioning system are controlled on a PC console. The therapeutic array is mounted to the tank, facing the RBC phantom. The cross of two laser beams, one along and the other perpendicular to the ultrasound beam, indicates the focus of the therapeutic array. The RBC layer is placed on the focal plane.

2.2.3 Ultrasound generation and focal pattern synthesis

The driving phase and intensity of each element on the 513-element 2-D phased array can be individually controlled by an array control system designed and constructed in our group [21]. Therapy pulses were generated with all elements driven in phase focused at the geometric focus.

To deliver preconditioning pulses to the annular region immediately surrounding the treatment center, a direct focal pattern synthesis technique was used. The array elements were divided into four sectors as a sector vortex array, which produces multiple foci patterns by applying a specially designed phase delay to each sector [22, 23]. In the present study, a phase delay of 0, $\pi/2$, π, or $3\pi/2$ was assigned to each sector (**Figure II-2b**). This particular phasing simultaneously excited 4 foci in the annular region surrounding the central axis while maintaining a zero intensity all along the central axis. **Figure II-2c** shows the 4-foci pattern simulated by summing the contribution from each rectangular radiator on the array using the Rayleigh-Sommerfeld integral [24]. It is noted that continuous wave source and linear propagation were assumed for the simulation. Nonlinear propagation and transient response were not incorporated. As shown in **Figure II-2c**, gaps exist between the four "hot spots" in the annular region. The annular region would not be uniformly treated with a single 4-foci pattern. To more uniformly treat the entire annular region, 4 multi-foci patterns were generated. Each pattern contained 4 foci as shown in **Figure II-2c**, but was rotated 0º, 22.5º, 45º or 67.5º around the central axis of the array. The four patterns were fired sequentially with zero delay between patterns.

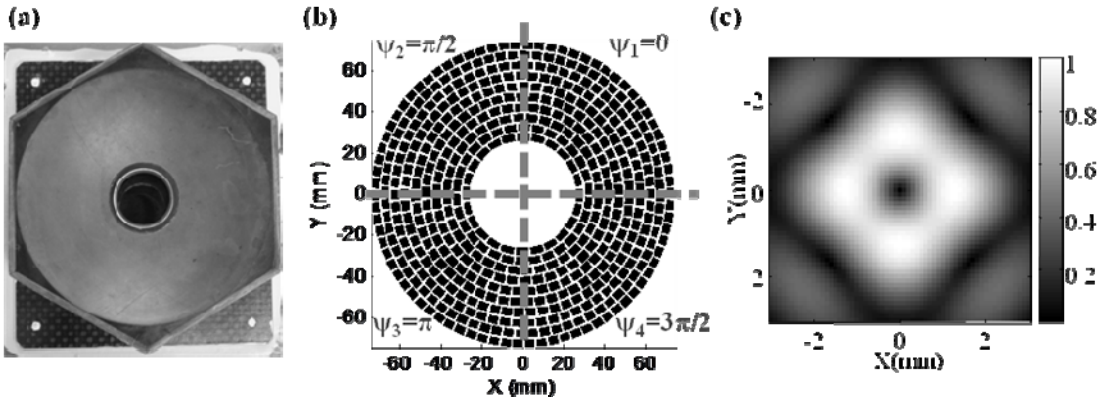

Figure II-2: Photograph (a) and element configuration (b) of the 513-element phased array. Using a sector vortex phasing as indicated in (b), an annular focal pattern can be produced. Panel (c) shows the simulation of the annular focal pattern with color bar indicating the normalized pressure in linear scale.

2.2.4 Ultrasound calibration

Acoustic waveforms were calibrated in degassed water using the FOPH with an active element of 100 μm in diameter. The peak negative (P−) and peak positive (P+) pressures were measured. The −6-dB beamwidths were calculated on both P− and P+ pressure profiles.

For therapy pulses, the P−/P+ pressures were measured 21/76 MPa (**Figure II-3a**). The lateral and axial −6-dB beamwidths were measured at a reduced P−/P+ pressure of 10/45 MPa. The lateral −6-dB beamwidth measured on the P− and P+ pressure profiles were 2.0 mm and 0.7 mm, respectively. The axial −6-dB beamwidth measured on the P− and P+ pressure profiles were 19.0 mm and 7.5 mm, respectively. The beamwidths at higher pressures could not be successfully measured because cavitation may occur within a few pulses and damage the fiber tip during the pressure profile scan. The measurements were performed both with and without the therapeutic array firing the preconditioning pulses. The beamwidths were identical in both cases. A small variation in the peak

pressures (< 1 MPa) was found to occur when preconditioning pulses were fired. Since the pressure of the therapy pulse was far beyond the threshold for producing histotripsy lesions [25], this pressure variation was considered negligible.

For preconditioning pulses, a full 2-D field scan on the focal plane was performed with total pulse duration of 20 cycles (i.e., 5 cycles for each pattern) at P−/P+ pressure of 7.2/13.6 MPa. At each sample location on the focal plane, the pressure waveforms of the preconditioning pulse was recorded (a representative waveform is shown in **Figure II-3b**). Spatial pressure distributions of the preconditioning pulses are displayed in **Figure II-3c, d**. The −6-dB beamwidth on the P− pressure profile approximately covered an annular region with a 0.7 mm inner diameter and a 4.3 mm outer diameter; the −6-dB beamwidth on the P+ pressure profile approximately covered an annular region with a 1.3 mm inner diameter and a 3.5 mm outer diameter.

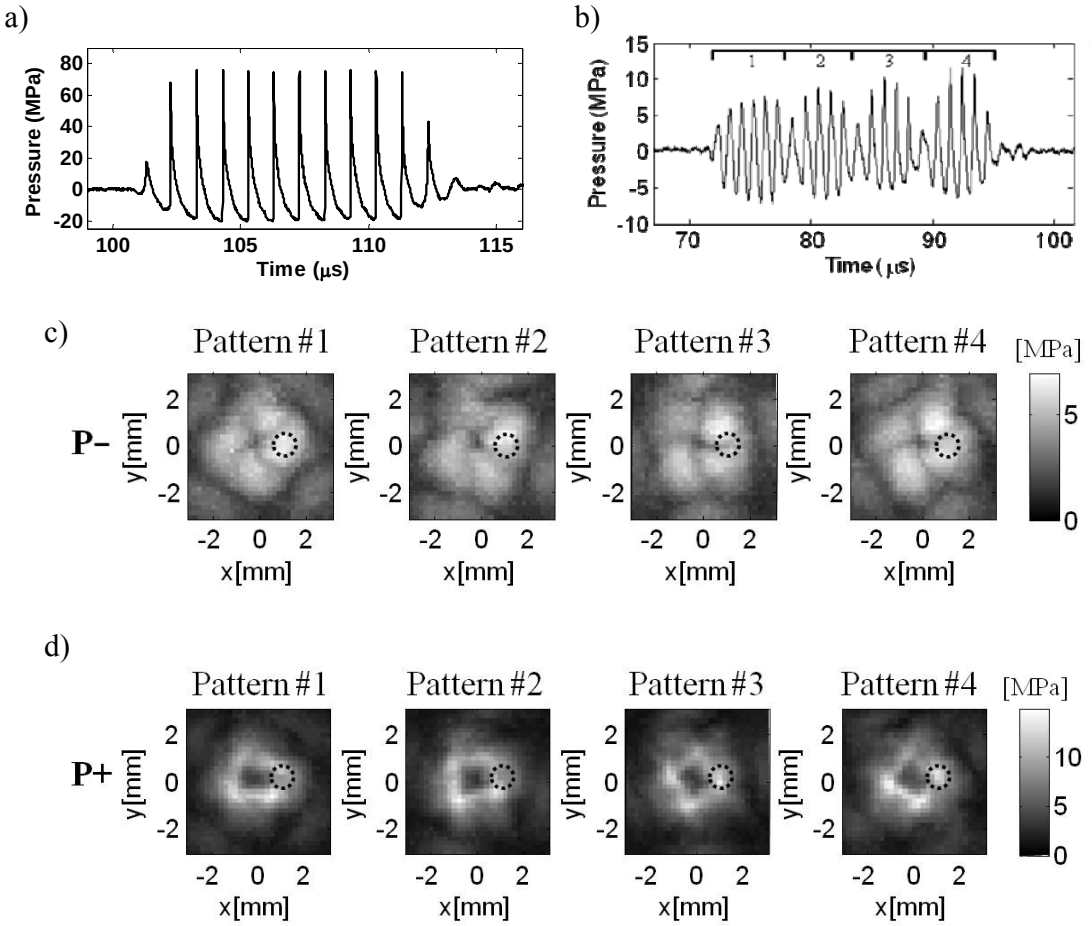

Figure II-3: Calibration of the therapy pulse (panel (a)) and the preconditioning pulse (panels (b)-(d)). The waveform of the therapy pulse is shown in panel (a). A representative waveform of the preconditioning pulse is shown in panel (b). The waveform of the preconditioning pulse is composed of 4 segments which correspond to the 4 sequentially fired multi-foci patterns. Panels (c) and (d) show the spatial peak negative (P−) and peak positive (P+) pressure distributions on the focal plane of the 4 sequentially fired multi-foci patterns in the preconditioning pulse. The waveform in panel (b) was measured at the location indicated by the circles in panels (c) and (d).

2.2.5 Ultrasound exposure conditions

A concurrent pulsing strategy was investigated for focal zone sharpening. A preconditioning pulse was delivered to the annular region surrounding the focus prior to each therapy pulse. A schematic of the pulse sequence is illustrated in **Figure II-4**. In all experiments, 10-cycle therapy pulses were delivered to the geometric focus with a constant pressure at P−/P+ pressure of 21/76 MPa. The pulse repetition frequency (PRF) in this chapter refers to the repetition frequency of the entire two-pulse sequence, and was held constant at 100 Hz. Both the therapy and the preconditioning pulses were delivered at 1 MHz. Each lesion was produced by a total of 5000 pulse sequences.

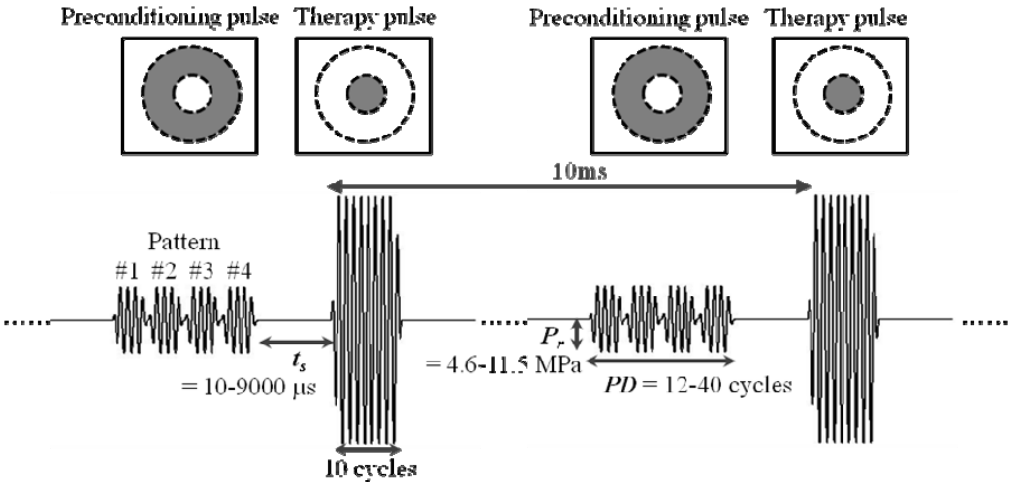

Figure II-4: A schematic drawing of the concurrent spatial-temporal pulsing sequence for active focal zone sharpening. The upper panels indicate the region where ultrasound pulses were focused (marked in gray). The lower panels show the temporal pulsing sequence. A total of 4 multi-foci patterns were sequentially delivered to the peripheral annular region prior to each therapy pulse. Effects of the pressure, P_r, and total pulse duration, PD, of the preconditioning pulses, and the separation time between preconditioning and therapy pulses, t_s, were studied.

To find effective pulse parameters for focal zone sharpening, a parametric study was performed on the effects of 1) pressure, 2) pulse duration, and 3) delivery time of the preconditioning pulses. The pressures of the preconditioning pulses ranged from below to slightly above the threshold for inducing histotripsy lesions (P−/P+ pressure ~ 8/17 MPa as suggested in [25]). The pulse durations were tested in the range commonly used in histotripsy (< 50μs). The delivery times of the preconditioning pulse were tested within the pulse repetition period of the therapy pulse. A total of 107 treatments in the RBC phantoms were included for the parametric study. The exposure conditions of the three experimental series are summarized in **Table II-1**. Effective pulse parameters for focal zone sharpening were derived from the parametric study and used in the subsequent studies.

Table II-1: Ultrasound exposure parameters for nuclei preconditioning pulses.

	Peak positive pressure (MPa)	Peak negative pressure (MPa)	Pulse duration per pattern (cycles)	Total pulse duration (cycles)	Separation time between preconditioning and therapy pulses, t_s (μs)	Sample size
Control	N/A	N/A	N/A	N/A	N/A	24
Series 1. Variable pressure	8.8	4.6	5	20	10	6
	13.6	7.2				23
	30.2	11.5				12
Series 2. Variable pulse duration	13.6	7.2	3	12	10	6
			5	20		23
			7	28		6
			10	40		6
Series 3. Variable separation time between preconditioning and therapy pulses	13.6	7.2	5	20	10	23
					100	10
					500	12
					5000	7
					9900	6

2.2.6 Lesion analysis

Because the RBCs were lysed in the local area treated with histotripsy, more light could penetrate through the damaged area, resulting in increased brightness. Therefore, the damaged area could be clearly visualized through the transparent gel layers (**Figure II-5 a-c**). The lesions were imaged using a digital camera (Coolpix 4500, Nikon, Tokyo, Japan) with backlighting provided from a white light table (Porta-Trace, Gagne, Johnson City, NY, USA). Quantitative analysis of the lesion images was performed using Matlab (Mathworks, Natick, MA, USA). The presence of damage at each pixel was determined when the pixel intensity exceeded a threshold of mean + 3×standard deviation intensity in the unaffected area. Using this threshold, the original bright-field lesion images were converted to binary lesion images (**Figure II-5 d-f**). The damaged areas in the treatment center and in the peripheral annular region were measured separately. To define the treatment center and the peripheral annular region, the centroid of the entire lesion was located on the binary lesion images. A ring centered at the centroid of the lesion with a 1.3 mm inner diameter and a 3.5 mm outer diameter was defined as the peripheral annular region (**Figure II-5 e-f**). This ring area was the overlapped region of the −6-dB beamwidths on the P− and P+ pressure profiles, i.e., approximate focal zone, of the preconditioning pulses. The area surrounded by the ring was defined as the treatment center. The damaged area was calculated by integrating the pixels in the presence of damage for each region.

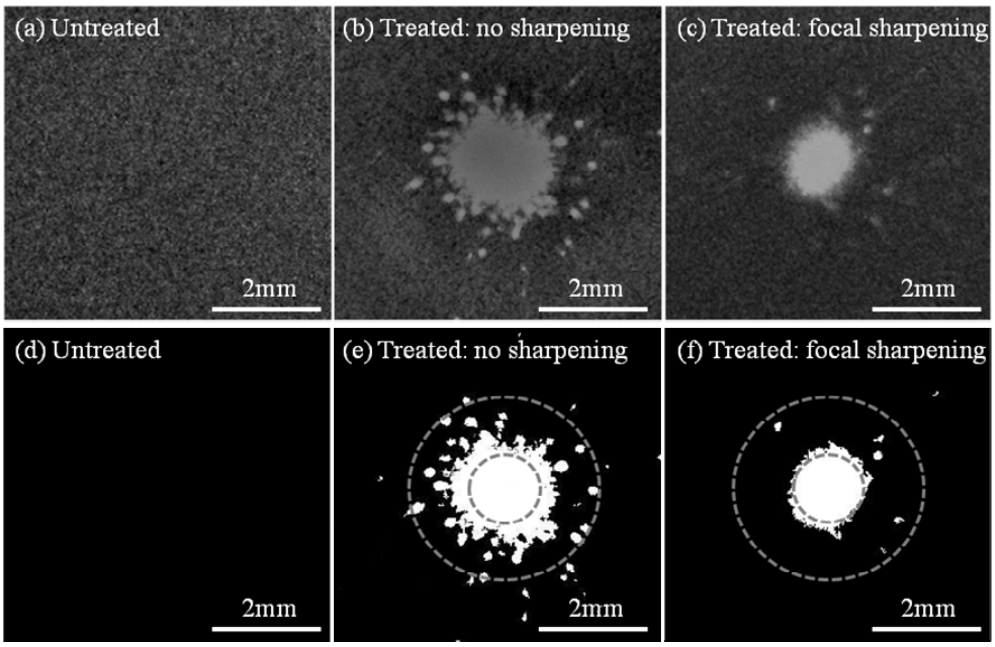

Figure II-5: Representative images of the lesions in RBC phantoms are shown in panels (a)-(c). The corresponding binary lesion images are shown in panels (d)-(f), where the damaged area is marked in white and the unaffected area is marked in black. The ring area outlined by the dashed lines indicates the focal zone (overlapped region of the −6-dB beamwidths on the P− and P+ pressure profiles) of the preconditioning pulses.

2.2.7 High speed photography of bubble clouds

Bubble clouds generated with or without focal zone sharpening were imaged over two time periods with two setups: 1) during a pulse using an ultra high speed camera (SIM02, Specialised Imaging Ltd., Hertfordshire, UK), and 2) over the treatments using a medium high speed camera (Phantom 210, Vision Research, Wayne, NJ). The bubble clouds were generated in the agarose phantom prepared with or without the RBCs. Backlighting was provided using a high power short duration white light flash lamp (SIL 500, Specialised Imaging Ltd., Hertfordshire, UK). A projection of the bubble cloud (and

the corresponding lesion if the RBC-gel layer was embedded in the phantoms) on an axial-lateral plane of the therapeutic array was captured.

In the first setup, the bubble clouds were imaged from 6 μs prior to the therapy pulse's arrival at the focus, to 14 μs after the pulse ended, with an interframe delay of 2 μs and an exposure time of 100 ns. This imaging duration ensured the observation of the maximum spatial extent of the bubble cloud, since the maximum size of the bubble cloud has been found to occur at the end of the pulse [6, 26].

In the second setup, the bubble cloud was imaged at the end of the therapy pulse when the maximum extent of the bubble cloud was reached. The bubble cloud was imaged at each therapy pulse for 1000 pulses so that the change in the bubble dynamics during the entire treatment was revealed. The lesion was imaged at 9 ms after each therapy pulse. At this time, very few bubbles persisted in the treatment volume, and the persistent bubbles were very small. Therefore, the lesion can be clearly visualized without interference from the persistent bubbles.

The spatial extent of the bubble cloud was measured using the maximum width of the bubble cloud in the lateral direction of the therapeutic array. The pixels representing bubbles were determined as those for which the pixel intensity was below a threshold of mean – 3 × standard deviation of the background pixel intensity. A histogram was calculated for the lateral positions of the pixels representing bubbles. The width of the bubble cloud was defined as distance between the 5^{th} and 95^{th} percentile of the histogram. A maximum width of the bubble cloud was calculated for each bubble cloud. A mean and standard deviation of the maximum width were obtained from 8

independently generated bubble clouds with and without focal zone sharpening. Because the area of the lesion matched well with that of the bubble cloud [7], the maximum width of the bubble cloud should be proportional to the square root of the maximum lesion area.

2.2.8 Treatments in ex vivo tissues

A total of 4 *ex vivo* treatments were performed in freshly excised canine livers to validate the effects of focal zone sharpening in real tissues. The canine liver tissues were obtained from healthy adult research subjects, preserved in degassed saline at room temperature, and used within 3 hours of harvest. The liver tissues were sectioned into 9 cm (width) × 5 cm (length) × 5 cm (thickness) samples, sealed in Ziploc bags filled with saline, and placed where the RBC phantom was in **Figure II-1**. The acoustic parameters used for the *ex vivo* tissue treatments were also derived from the parametric study above. Each lesion was produced using 5000 therapy pulses. After treatments, the tissue samples were fixed in formalin and prepared for hematoxylin and eosin (H&E) sections. The lesions were sectioned transversely with respect to the ultrasound beam. Multiple 5-μm thick H&E sections were made through the entire lesion. The sections with the maximum spatial extent of damage were examined with comparisons between those with and without focal zone sharpening.

2.3 Results

2.3.1 Parametric study for pulse sequence development

Representative lesion images are shown in **Figure II-5**. In an untreated area, the RBC phantom appeared translucent (**Figure II-5a**). The RBCs in this area also appeared intact under microscopic examination. In a treated area, the lesion was clearly visualized as the damaged locations turned transparent. The lesions produced with and without focal zone sharpening appeared significantly different. Lesions produced without focal zone sharpening had a ~ 2 mm diameter damaged area in the center with an irregular boundary. Immediately surrounding the center was a ~ 1 mm transition zone of round or elliptical-shaped scattered damaged spots. The diameters of these scattered damaged spots ranged from 50 to 200 μm each. Very few, if any, damage spots were observed outsides the transition zone (**Figure II-5b**). In contrast, highly confined lesions were produced using focal zone sharpening. The damaged area was ~ 1.5 mm in diameter with a smoother boundary and very few peripheral damaged spots (**Figure II-5c**).

1) *Effects of pressure of preconditioning pulses:* **Figure II-6** shows representative binary lesion images, and the damaged area as a function of the peak negative pressure of the preconditioning pulses. Student's *t*-test and one-way analysis of variance (ANOVA) were performed to compare the calculated damaged area for each case. Results indicated that: 1) the damaged area in the center was similar for all pressures except for the lowest pressure, 4.6 MPa ($p < 0.01$, N = 7 – 24; ANOVA); 2) the damaged area in the peripheral annular region was reduced for all pressures, and decreased with decreasing pressures within 4.6 – 11.5 MPa ($p < 0.01$ for each pair, N

= 7 – 24; *t*-test). The preconditioning pulses at the lowest pressure (4.6 MPa) reduced the damage in the peripheral annular region most significantly but also resulted in incomplete treatment in the center. Therefore, a medium pressure level, 7.2 MPa, was chosen to achieve focal zone sharpening without interfering treatment in the center.

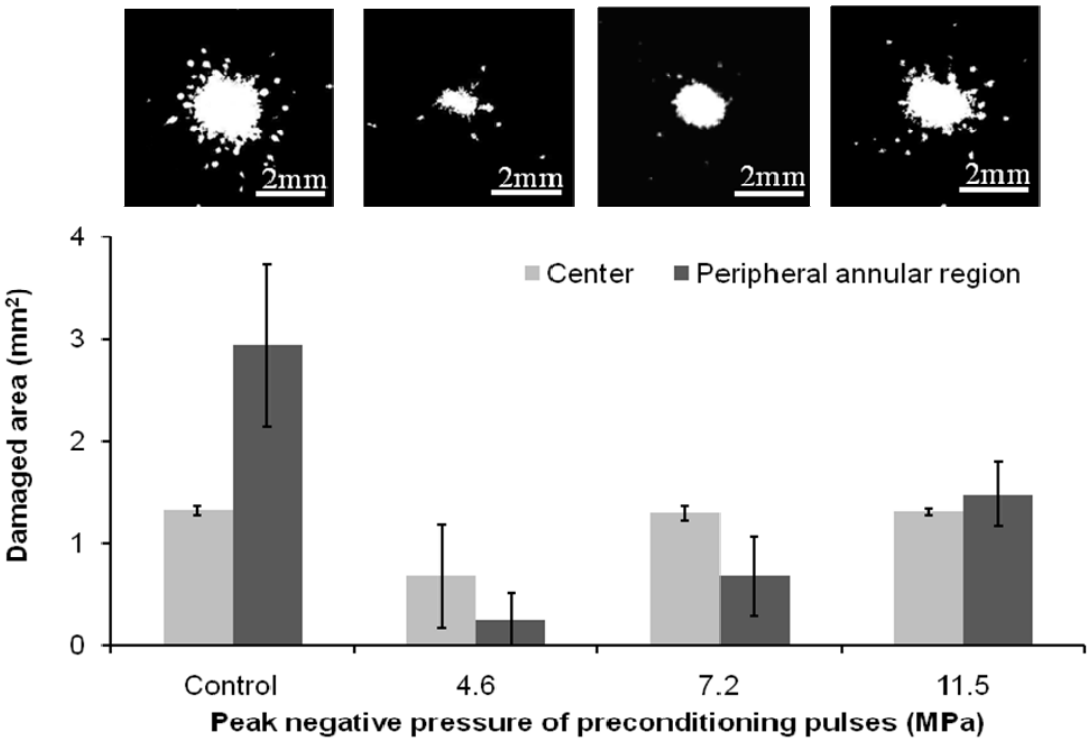

Figure II-6: Representative lesion patterns and calculated damaged area in the center and the peripheral annular region using preconditioning pulses at varying pressures. Data points are expressed in mean ± standard deviation (N = 6 – 24).

2) *Effects of pulse duration of preconditioning pulses:* **Figure II-7** shows representative binary lesion images, and the damaged area as a function of the pulse duration of the preconditioning pulses. Results showed that: 1) the damaged area in the center was similar for all cases ($p > 0.2$, N = 6 – 24; ANOVA); and 2) the damaged area in the peripheral annular region was reduced with preconditioning pulses using all 4 pulse

durations, and the smallest damaged area was achieved at pulse duration of 20 cycles ($p < 0.06$ for each pair, N = 6 – 24; *t*-test).

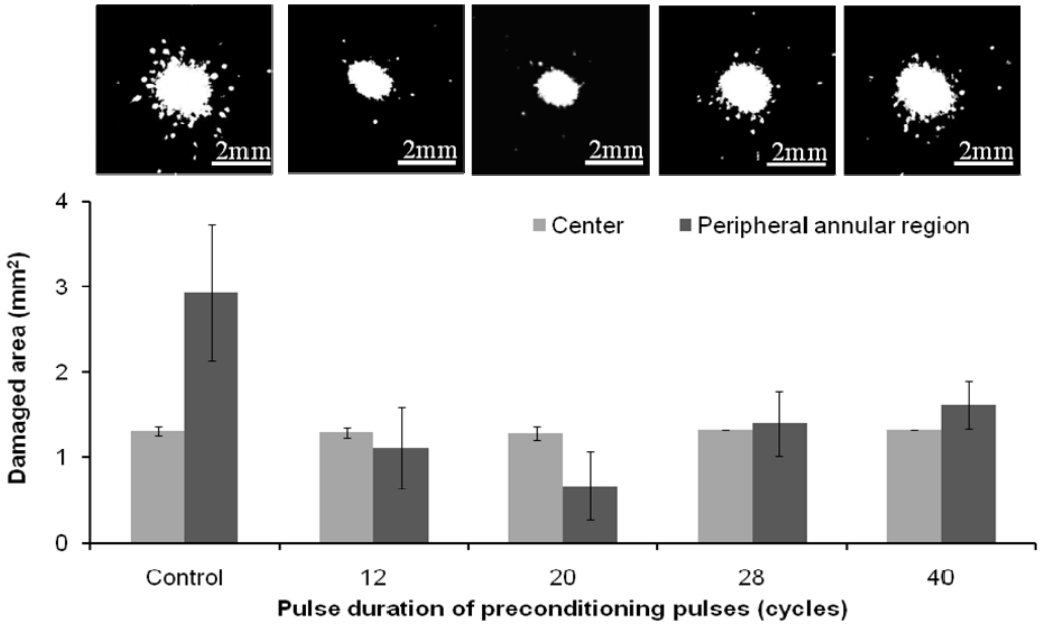

Figure II-7: Representative lesion patterns and calculated damaged area in the center and the peripheral annular region using preconditioning pulses at varying pulse durations. Data points are expressed in mean ± standard deviation (N = 6 – 24).

3) *Effects of separation time between preconditioning and therapy pulses:* **Figure II-8** shows representative binary lesion images, and the damaged area as a function of the separation time between preconditioning and therapy pulses. Here, the separation time refers to the interval from the end of the preconditioning pulse to the beginning of the therapy pulse. Results indicated that: 1) the damaged area in the center was similar for all cases ($p > 0.05$, N = 6 – 24; ANOVA); 2) the damaged area in the peripheral annular region was reduced with a separation time no longer than half pulse repetition period, i.e., 5000 μs ($p < 0.01$ for each pair, N = 6 – 24; *t*-test); the

minimum was found at the shortest tested separation time- 10 μs ($p < 0.01$ for each pair, N = 6 – 24; *t*-test); no discernible difference was found among separation times of 100 – 5000 μs ($p > 0.2$, N = 6 – 24; ANOVA); the damaged area in the periphery was similar to the control when the preconditioning pulse was delivered far (9900 μs) before the therapy pulse, or shortly (100 μs) after the previous therapy pulse ($p > 0.6$, N = 6 – 24; *t*-test).

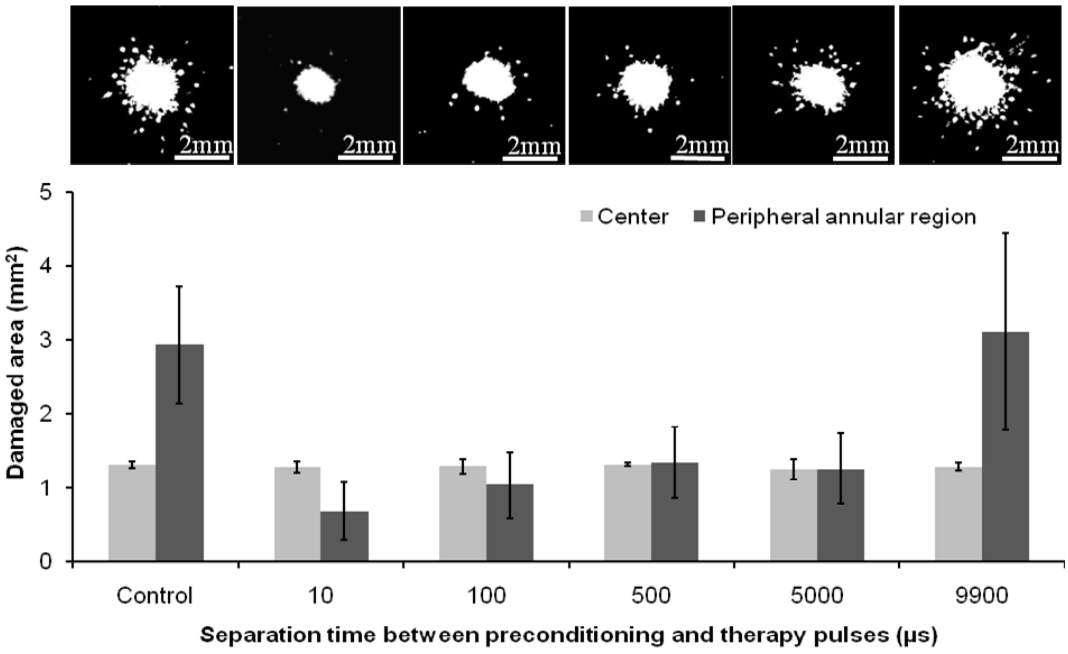

Figure II-8: Representative lesion patterns and calculated damaged area in the center and the peripheral annular region at varying separation times between preconditioning and therapy pulses. Data points are expressed in mean ± standard deviation (N = 6 – 24).

Based on these results, we found an effective pulse sequence for focal zone sharpening consisting of a 20 cycle pulse delivered to the peripheral annular region at

P−/P+ pressure of 7.2/13.6 MPa prior to the therapy pulses with a separation time of 10 μs. This pulse sequence was used for the subsequent studies.

2.3.2 High speed photography of bubble clouds

<u>During a pulse</u>

The bubble clouds produced with and without focal zone sharpening shared the same evolutionary trend (**Figure II-9**). The bubble cloud grew along the direction of ultrasound as the ultrasound pulse propagated through the focus. After the ultrasound pulse was ceased, the bubble cloud shrunk in size and gradually disappeared on the optical images. The maximum spatial extent of the bubble cloud was achieved at the end of the ultrasound pulse. Individual bubbles in the cloud formed and grew during the pulse. The individual bubbles grew to ≤ 200 μm in radius by the end of the pulse, and gradually dissolved after the pulse ended.

The shape and size of the bubble clouds produced with and without focal zone sharpening were significantly different. Without focal zone sharpening, the bubble cloud was composed of sparsely distributed individual bubbles in a cigar-shaped region (**Figure II-9a**). With focal zone sharpening, the majority of individual bubbles appeared in a more confined region along the central axis, resulting in a much narrower and denser bubble cloud. Fewer bubbles were present in the periphery (**Figure II-9b**). The maximum width of the bubble cloud was calculated with and without focal zone sharpening (**Table II-2**). The results indicated that the maximum width of the bubble cloud decreased by 48 ± 24% using focal zone sharpening ($p < 0.01$, N = 8; *t*-test).

(a) Without focal zone

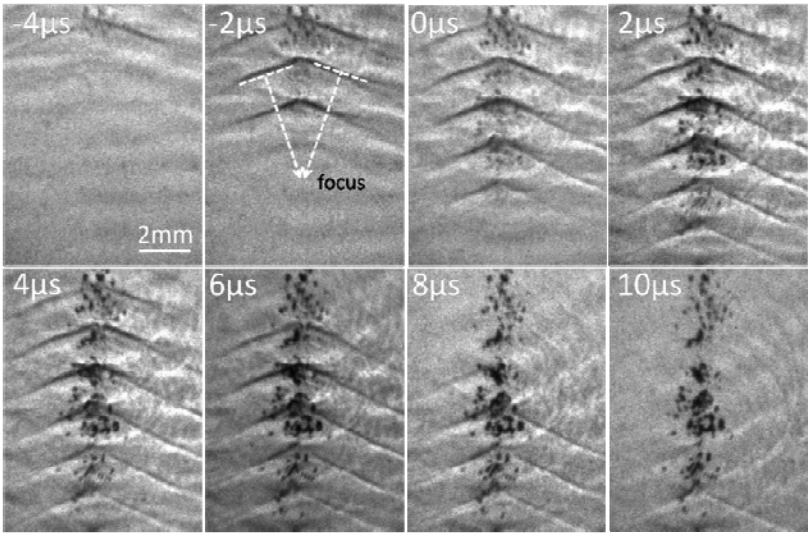

(b) With active focal zone

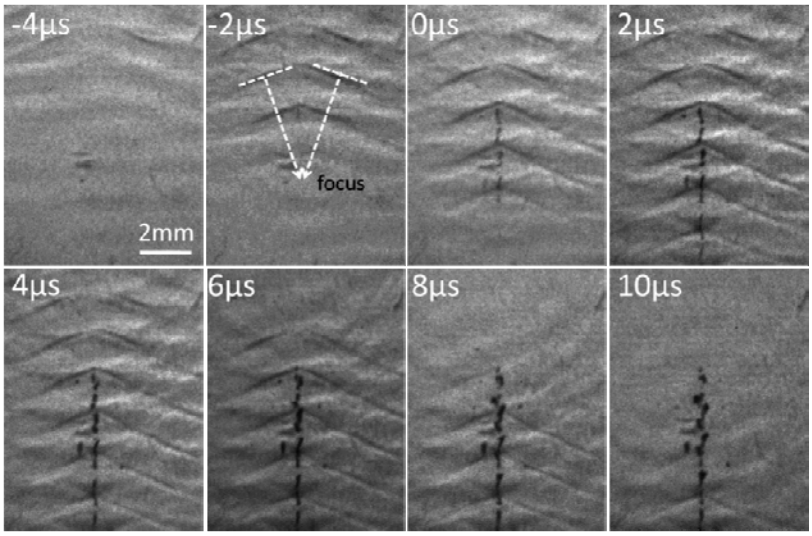

Figure II-9: High speed optical images of bubble clouds generated (a) without or (b) with focal zone sharpening. The time is displayed with respect to the first cycle's arrival at the focus. The dark crossed lines are the shockfronts of the ultrasound.

Table II-2: Maximum width of bubble clouds

	Maximum width of bubble clouds (mm)	Sample size
No focal zone sharpening	1.35 ± 0.22	8
Focal zone sharpening	0.70 ± 0.32	8

Over the entire treatment

Without nuclei preconditioning, the spatial extent of the bubble cloud remained unchanged during the entire 1000-pulse treatment. Individual bubbles in a bubble cloud were generated at random locations in the oval-shaped focal zone (**Figure II-10a**). The bubbles lasted for > 100 pulses, and slowly migrated in the direction of ultrasound propagation at an average velocity of 0.7±0.5 mm/s.

With nuclei preconditioning, a decreasing trend of the spatial extent of the bubble cloud was observed. The width of the bubble cloud was similar to that produced without nuclei preconditioning in the first several pulses. The width quickly decreased as the pulse number increased. Within 200 pulses, the minimum width of the bubble cloud, approximately 1/3 of the original width, was reached. The width remained unchanged from 200 to 1000 pulses (**Figure II-10b, c**). The individual bubbles in the periphery disappeared within 22±35 pulses. Or they quickly migrated away from the periphery, mostly toward the focal center, at an average velocity of 5.0±2.6 mm/s. The bubble migration was likely induced by the radiation force of the nuclei preconditioning pulses applied to the periphery.

(a) Control

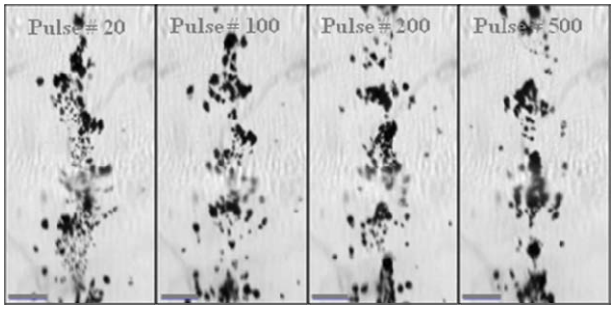

(b) Nuclei preconditioning

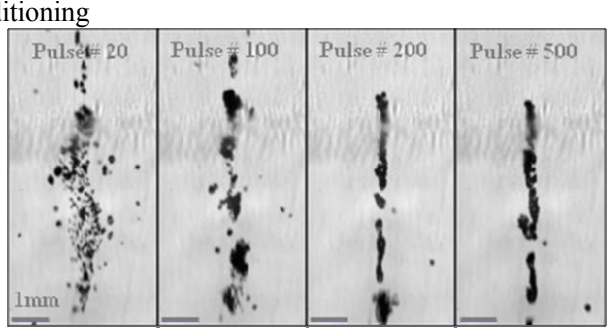

(c)

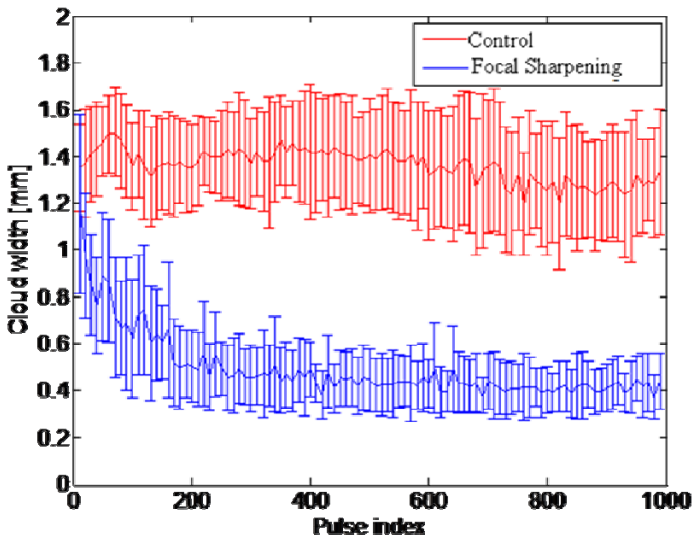

Figure II-10: Progressive change in spatial extent of the bubble clouds produced (a) without and (b) with nuclei preconditioning. In panels (a) and (b), ultrasound propagated from top to bottom of the image. An axial-lateral projection of the bubble cloud was shown. The width of the bubble cloud was calculated in panel (c). Data expressed in mean ± standard deviation (N=12)

Figure II-11 shows the lesion development process in the red blood cell phantoms without and with nuclei preconditioning. Before treatment, the target treatment zone appeared intact (shown as gray on the images). As the treatment started, cells in the damaged area were lysed, and the damaged area turned transparent (shown as white on the images). The damaged area increased as the pulse number increased.

The lesion development process was different without and with nuclei preconditioning. Without nuclei preconditioning, several subvolumes of damage were first formed separately along the central axis of the focus. The separated clusters of damage occurred constantly in treatments without nuclei preconditioning, and were likely induced due to shadowing of ultrasound from the bubble clusters closer to the therapy transducer. As the pulse number increased, these subvolumes gradually expanded, and fused to form an oval-shaped lesion at 2000 pulses. The lesion appeared inhomogeneous during the treatment when <1000 pulses were delivered. The focal center was not completely damaged until 2000 pulses (**Figure II-11a**). With nuclei preconditioning, a homogeneous lesion was observed during the entire treatment. As the pulse number increased, the lesion expanded in a highly controlled manner. A cylindrical-shaped lesion was clearly visible at 100 pulses. The focal center was completely damaged within 1000 pulses (**Figure II-11b**).

(a) Control

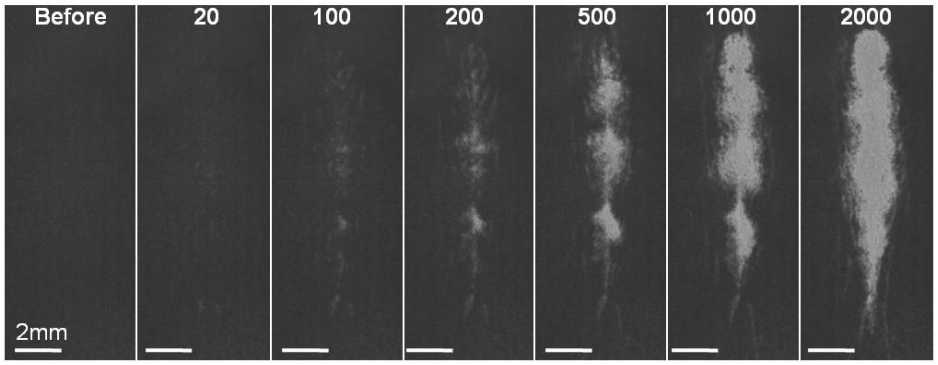

(b) Nuclei preconditioning

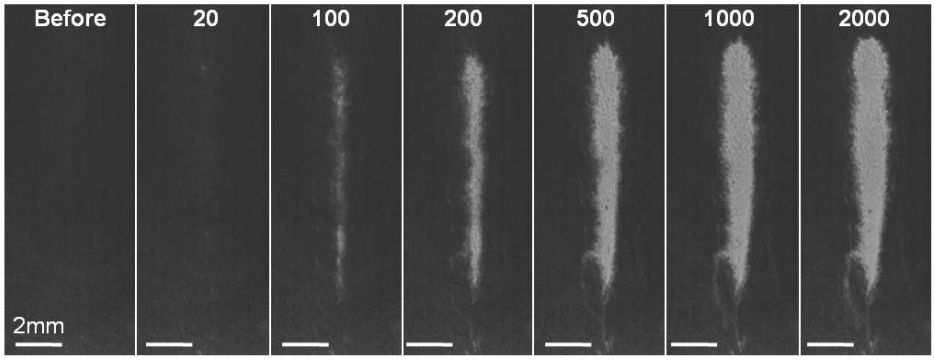

Figure II-11: Lesion development process (a) without and (b) with nuclei preconditioning. The intact area appears gray while the damaged area appears white. The pulse number of each frame was indicated on top of the images.

2.3.3 Treatments in ex vivo tissues

The lesion histology demonstrated that highly confined lesions were produced in real tissues using focal zone sharpening as well as in the RBC phantoms.

Without focal zone sharpening, a completely fractionated region approximately 1.5 mm in diameter was observed in the center of the lesion. No recognizable tissue or cellular components were found in this region (**Figure II-12a**). Scattered damaged spots were present in a ~ 0.8 mm transition zone outside the central damaged region (**Figure**

II-12c, for example). The diameter of the peripheral damaged spots ranged from 60 – 200 μm each.

With focal zone sharpening, the central damage region was narrowed to approximately 0.8 mm in diameter (**Figure II-12b**). Much smoother lesion boundaries with no significant scattered damaged spots were observed (**Figure II-12d**).

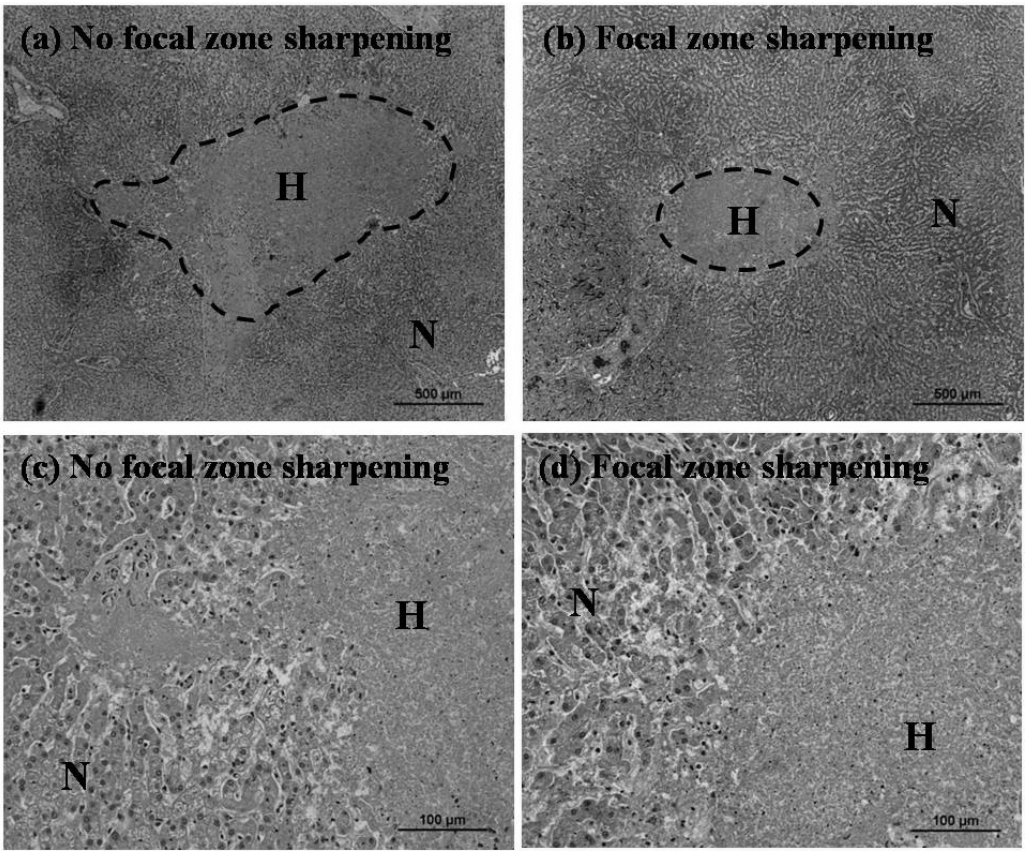

Figure II-12: Histology of lesions produced without (panels (a) and (c)), and with focal zone sharpening (panels (b) and (d)) at different magnifications. At lower magnification (panels (a) and (b)), a completely homogenized area (H) was observed in the centers with and without focal zone sharpening. Tissue outside this transition zone appeared normal (N). At higher magnification, an irregular lesion boundary with radial projections was observed in lesions produced without focal zone sharpening (panel (c)). Lesions produced with focal zone sharpening present a more regular boundary with no significant peripheral damaged spots (panel (d)).

2.4 Discussion and Conclusions

We have demonstrated that highly confined lesions can be produced using spatial control of the bubble cloud in histotripsy. While damage in the periphery was suppressed, complete fractionation in the treatment center was achieved. The effect of focal zone sharpening has been demonstrated both in RBC phantoms and in *ex vivo* tissues. This technique could be useful in many clinical applications where precise and confined tissue ablation is needed, such as fetal or neonate surgery [1].

High speed imaging of the bubble clouds illustrated that the preconditioning pulses substantially altered the appearance of the bubble clouds. The cigar-shaped bubble cloud produced without focal zone sharpening is consistent with our previous observations [5, 6] and with the general shape of the focal zone of the geometrically focused field. Since the lesion most likely occurred where the cavitation bubbles appeared [7], this cigar-shaped bubble cloud may account for the cigar-shaped lesions observed in our previous *in vitro* and *in vivo* studies [27, 28]. Using focal zone sharpening strategy, much narrower and denser bubble clouds were generated. The significant change in the spatial extent of the bubble cloud may explain why more confined lesions were produced.

High speed photography of the bubble clouds and the cavitation nuclei suggested two possible mechanisms for local cavitation suppression in the periphery. First, the nuclei preconditioning pulses may shift the size distribution of the cavitation nuclei (an effect similar to [29-31]), such that appropriately sized nuclei were reduced. Our previous study suggested that violent cavitation activities ceased to occur when bubbles were

larger than 45 μm [26]. In the present study, the sizes of the cavitation nuclei in the periphery were close to this range. This may prevent further cavitation in the periphery. Another possible mechanism is that the cavitation nuclei may have been propelled away from the periphery by the radiation force generated in the acoustic field of the sector vortex configuration [32]. This may remove the available cavitation nuclei and prevent cavitation in the periphery. In addition, researchers have observed that the spatial extent of the bubble cloud may decrease with increased cavitation nuclei concentration [33]. It is possible that the preconditioning pulses may have excited excess cavitation nuclei such that a dense and narrow bubble cloud was formed. An investigation on the underlying mechanisms is underway.

The lesion morphology depends on the acoustic parameters of the preconditioning pulses. For example, the lowest acoustic pressure (4.6MPa) reduced the damaged area both in the periphery and in the center. This could be because lower pressures more likely destruct cavitation nuclei rather than excite them [34-36]. Therefore, cavitation is further suppressed and the damaged area is reduced at lower pressures. Unfortunately, effects of pressures lower than 4.6MPa could not be studied because the range of amplitude modulation is limited on the therapeutic array driving system.

The demonstration of local suppression of cavitational damage in a selected zone implies a more general application: active protection of an arbitrarily selected zone. Complete fractionation of target tissue volume while preserving critical structures has been an important issue for tissue ablation therapies. An intuitive way to protect the critical structures is to intentionally skip over those structures on treatment planning. With the local nuclei preconditioning technique, we may not only passively skip the

critical structures, but also actively protect them using appropriate ultrasound pulses. The method would locally raise the threshold for cavitation damage in the selected tissue. As a result, the selected protection zone may be resistant to cavitation damage. Active protection for an arbitrarily selected zone is our ultimate goal and will be pursued in the future.

2.5 References

[1] Z. Xu, A. Ludomirsky, L. Y. Eun, T. L. Hall, B. C. Tran, J. B. Fowlkes, and C. A. Cain, "Controlled ultrasound tissue erosion," *IEEE Trans. Ultrason., Ferroelect., Freq. Contr.,* vol. 51, pp. 726-736, Jun 2004.

[2] Z. Xu, T. L. Hall, J. B. Fowlkes, and C. A. Cain, "Effects of acoustic parameters on bubble cloud dynamics in ultrasound tissue erosion (histotripsy)," *J. Acoust. Soc. Amer.,* vol. 122, pp. 229-236, Jul 2007.

[3] Z. Xu, T. L. Hall, J. B. Fowlkes, and C. A. Cain, "Optical and acoustic monitoring of bubble cloud dynamics at a tissue-fluid interface in ultrasound tissue erosion," *J. Acoust. Soc. Amer.,* vol. 121, pp. 2421-2430, Apr 2007.

[4] Z. Xu, J. B. Fowlkes, E. D. Rothman, A. M. Levin, and C. A. Cain, "Controlled ultrasound tissue erosion: the role of dynamic interaction between insonation and microbubble activity," *J. Acoust. Soc. Amer.,* vol. 117, pp. 424-435, Jan 2005.

[5] Z. Xu, M. Raghavan, T. L. Hall, C. W. Chang, M. A. Mycek, J. B. Fowlkes, and C. A. Cain, "High speed imaging of bubble clouds generated in pulsed ultrasound cavitational therapy--histotripsy," *IEEE Trans Ultrason Ferroelectr Freq Control,* vol. 54, pp. 2091-101, Oct 2007.

[6] Z. Xu, M. Raghavan, T. L. Hall, M. A. Mycek, J. B. Fowlkes, and C. A. Cain, "Evolution of bubble clouds induced by pulsed cavitational ultrasound therapy - histotripsy," *IEEE Trans Ultrason Ferroelectr Freq Control,* vol. 55, pp. 1122-32, May 2008.

[7] A. D. Maxwell, T.-Y. Wang, L. Yuan, A. P. Duryea, Z. Xu, and C. A. Cain, "A tissue phantom for evaluation of mechanical damage caused by cavitation," in submission.

[8] L. R. Willis, A. P. Evan, B. A. Connors, R. K. Handa, P. M. Blomgren, and J. E. Lingeman, "Prevention of lithotripsy-induced renal injury by pretreating kidneys with low-energy shock waves," *J Am Soc Nephrol,* vol. 17, pp. 663-73, Mar 2006.

[9] M. R. Bailey, R. O. Cleveland, T. Colonius, L. A. Crum, A. P. Evan, J. E. Lingeman, J. A. McAteer, O. A. Sapozhnikov, and J. C. Williams, Jr., "Cavitation in shock wave lithotripsy: the critical role of bubble activity in stone breakage and kidney trauma," in *Proc. IEEE Ultrason. Symp.*, 2003, pp. 724-727.

[10] A. P. Evan, L. R. Willis, J. A. McAteer, M. R. Bailey, B. A. Connors, Y. Shao, J. E. Lingeman, J. C. Williams, Jr., N. S. Fineberg, and L. A. Crum, "Kidney damage and renal functional changes are minimized by waveform control that suppresses cavitation in shock wave lithotripsy," *J Urol,* vol. 168, pp. 1556-62, Oct 2002.

[11] J. A. McAteer, M. A. Stonehill, K. Colmenares, J. C. J. Williams, and A. P. Evan, "SWL cavitation damage in vitro: Pressurization unmasks a differential response of foil targets and isolated cells," in *J. Acoust. Soc. Amer.* vol. 103, 1998, p. 3038.

[12] O. A. Sapozhnikov, V. A. Khokhlova, M. R. Bailey, J. C. Williams, Jr., J. A. McAteer, R. O. Cleveland, and L. A. Crum, "Effect of overpressure and pulse repetition frequency on cavitation in shock wave lithotripsy," *J Acoust Soc Am,* vol. 112, pp. 1183-95, Sep 2002.

[13] M. Delius, "Minimal static excess pressure minimises the effect of extracorporeal shock waves on cells and reduces it on gallstones," *Ultrasound Med Biol,* vol. 23, pp. 611-7, 1997.
[14] K. Kawabata, K. Sasaki, and S. Umemura, "Agents promoting and suppressing acoustic cavitation," in *Proc. IEEE Ultrason. Symp.*, 1998, pp. 1443 - 1446.
[15] J. Y. Chapelon, F. Dupenloup, H. Cohen, and P. Lenz, "Reduction of cavitation using pseudorandom signals," *IEEE Trans. Ultrason., Ferroelect., Freq. Contr.,* vol. 43, pp. 623-625, 1996.
[16] C. K. Holland and R. E. Apfel, "An improved theory for the prediction of microcavitation thresholds," *IEEE Trans Ultrason Ferroelectr Freq Control,* vol. 36, pp. 204-8, 1989.
[17] C. K. Holland and R. E. Apfel, "Thresholds for transient cavitation produced by pulsed ultrasound in a controlled nuclei environment," *J Acoust Soc Am,* vol. 88, pp. 2059-69, Nov 1990.
[18] M. Delius and W. Brendel, "A model of extracorporeal shock wave action: tandem action of shock waves," *Ultrasound Med Biol,* vol. 14, pp. 515-8, 1988.
[19] A. Henglein and M. Gutierrez, "Chemical reactions by pulsed ultrasound: memory effects in the formation of NO3- and NO2- in aerated water," *Int J Radiat Biol Relat Stud Phys Chem Med,* vol. 50, pp. 527-33, Sep 1986.
[20] J. E. Parsons, C. A. Cain, and J. B. Fowlkes, "Cost-effective assembly of a basic fiber-optic hydrophone for measurement of high-amplitude therapeutic ultrasound fields," *J. Acoust. Soc. Amer.,* vol. 119, pp. 1432-1440, Mar 2006.
[21] T. Hall and C. A. Cain, "A Low Cost Compact 512 Channel Therapeutic Ultrasound System For Transcutaneous Ultrasound Surgery," in *Amer. Inst. Phys. Conf. Proc.*, 2006, pp. 445-449.
[22] C. A. Cain and S. Umemura, "Concentric-ring and sector-vortex phased-array applicators for ultrasound hyperthermia," *IEEE Trans. Microwave Theory Tech.,* pp. 542-551, May, 1986 1986.
[23] S. Umemura and C. A. Cain, "The sector-vortex phased array: acoustic field synthesis for hyperthermia," *IEEE Trans Ultrason Ferroelectr Freq Control,* vol. 36, pp. 249-57, 1989.
[24] K. B. Ocheltree and L. A. Frizzel, "Sound field calculation for rectangular sources," *IEEE Trans Ultrason Ferroelectr Freq Control,* vol. 36, pp. 242-8, 1989.
[25] Z. Xu, J. B. Fowlkes, A. Ludomirsky, and C. A. Cain, "Investigation of intensity thresholds for ultrasound tissue erosion," *Ultrasound Med. Biol.,* vol. 31, pp. 1673-1682, Dec 2005.
[26] T.-Y. Wang, A. D. Maxwell, S. Park, Z. Xu, J. B. Fowlkes, and C. A. Cain, "Why Are Short Pulses More Efficient in Tissue Erosion Using Pulsed Cavitational Ultrasound (Histotripsy)?," in *Int. Symp. Therapeutic Ultrasound*, Aix en Provence, France, 2009.
[27] J. E. Parsons, C. A. Cain, G. D. Abrams, and J. B. Fowlkes, "Pulsed cavitational ultrasound therapy for controlled tissue homogenization," *Ultrasound Med. Biol.,* vol. 32, pp. 115-129, Jan 2006.
[28] W. W. Roberts, T. L. Hall, K. Ives, J. S. Wolf, Jr., J. B. Fowlkes, and C. A. Cain, "Pulsed cavitational ultrasound: a noninvasive technology for controlled tissue

ablation (histotripsy) in the rabbit kidney," *J. Urol.,* vol. 175, pp. 734-738, Feb 2006.
[29] C. C. Church, "A theoretical study of cavitation generated by an extracorporeal shock wave lithotripter," *J Acoust Soc Am,* vol. 86, pp. 215-27, Jul 1989.
[30] Y. Matsumoto and S. Yoshizawa, "Behaviour of a bubble cluster in an ultrasound field," *International journal for numerical methods in fluids,* vol. 47, p. 591, 2005.
[31] N. de Jong, M. Emmer, A. van Wamel, and M. Versluis, "Ultrasonic characterization of ultrasound contrast agents," *Med Biol Eng Comput,* May 26 2009.
[32] S. T. Kang and C. K. Yeh, "Potential-well model in acoustic tweezers," *IEEE Trans Ultrason Ferroelectr Freq Control,* vol. 57, pp. 1451-1459, Jun 2010.
[33] M. Arora, C. D. Ohl, and D. Lohse, "Effect of nuclei concentration on cavitation cluster dynamics," *J Acoust Soc Am,* vol. 121, pp. 3432-6, Jun 2007.
[34] W. T. Shi, F. Forsberg, P. Vaidyanathan, A. Tornes, J. Ostensen, and B. B. Goldberg, "The influence of acoustic transmit parameters on the destruction of contrast microbubbles in vitro," *Phys Med Biol,* vol. 51, pp. 4031-45, Aug 21 2006.
[35] C. K. Yeh and S. Y. Su, "Effects of acoustic insonation parameters on ultrasound contrast agent destruction," *Ultrasound Med Biol,* vol. 34, pp. 1281-91, Aug 2008.
[36] J. E. Chomas, P. Dayton, J. Allen, K. Morgan, and K. W. Ferrara, "Mechanisms of contrast agent destruction," *IEEE Trans Ultrason Ferroelectr Freq Control,* vol. 48, pp. 232-48, Jan 2001.

CHAPTER III. A DOSE-EFFICIENT TREATMENT STRATEGY FOR HISTOTRIPSY BY REMOVING CAVITATION MEMORY

3.1 Introduction

For cavitation-based therapy like histotripsy, the initiation and maintenance of the cavitation process is highly affected by the small gas bubbles in a host medium that serve as nuclei for cavitation [1]. These nuclei may preexist in the host medium as gas pockets adhering to crevices on particles or stabilized with organic skin ("stabilized" nuclei), or they may form as fragments of bubbles that persist from collapse of transient cavities ("unstabilized" nuclei) [2-5]. The unstabilized nuclei may become new cavitation sites that sustain subsequent cavitation events. This phenomenon, which has been discussed in the literature [2, 6-8], is referred as the cavitation memory effect.

The cavitation memory effect may be advantageous for cavitation-based therapies when the acoustic pressure is insufficient to consistently produce cavitation with each single pulse. In this case, the existence of the cavitation memory, or the persistent nuclei, may help sustain or enhance the cavitation process. This concept has been applied to improve the stone fragmentation efficiency in lithotripsy [9-13], or to enhance the tissue fractionation in histotripsy [14-16].

Despite the advantage of sustaining the cavitation process, the cavitation memory could be disadvantageous in some cases. One possible disadvantage is that the cavitation bubbles may repeatedly occur at the same locations within a focal volume in response to each pulse due to the presence of the cavitation nuclei. If the spatial distribution of the bubbles is not sufficiently dense, the areas where the cavitation bubbles repeatedly occur are over-treated while the rest areas remain under-treated. This can result in inhomogeneous tissue disruption even within a single focal volume, producing islands of structurally intact tissues in the treatment volume when a small dose is applied [17, 18]. These islands of intact tissues could be detrimental for applications where complete tissue removal is desired (e.g., tumor therapy). In addition, when quantitative tissue characterization methods (e.g., ultrasound spectrum analysis [19]) are used to assess the treatment outcomes, a misleading metric may be produced as an average of fully homogenized and non-homogenized zones.

To completely and homogeneously fractionate the target volume, strategies to break the memory-induced repeated cavitation pattern are needed. One strategy is to overdose the target volume until the cavitation bubbles migrate (sometimes slowly) to different locations in the target volume. However, this may cause inefficient use of energy and prolonged treatment time. Here we propose a dose-efficient strategy to achieve complete and homogeneous tissue fractionation by removing the cavitation memory. The removal of the memory should cause cavitation bubbles to occur at random locations in response to each pulse. As long as the pressure amplitude is high enough so that the cavitation can be consistently induced in each pulse, this random pattern would allow the target volume to be homogeneously fractionated for fewer pulses.

This study investigates the cavitation pattern, i.e., spatial distribution of the cavitation bubbles, in response to each histotripsy pulse and the corresponding lesion development process for different levels of cavitation memory. It is hypothesized that the cavitation memory would decrease with time as the persistent bubbles diffuse, dissolve, and redistribute to new random locations. As such, the level of the persistent memory can be manipulated (passively) by increasing the time interval between successive pulses. Experiments were performed both in the red blood cell (RBC) tissue phantoms [20] and in *ex vivo* liver tissues. The former allowed for direct visualization of the locations of the cavitation bubbles and the corresponding lesion development process in real time using high speed photography; the latter provided validation of the memory effect in real tissues with histological examinations. This study illustrates a significant effect of cavitation memory on the treatment progression, providing basis for future design of dose-efficient treatments.

3.2 Materials and Methods

3.2.1 Sample Preparation

An agarose-based RBC tissue phantom that allows for direct visualization of cavitation and the resulting damage was used to study the impact of the cavitation patterns on the lesion development process. The phantom was prepared with 1% agarose powder (Type-VII, Sigma-Aldrich, St. Louis, MO) and 5% v/v RBCs mixed in normal saline following the protocol described in our previous publication [20]. The phantom was constructed such that a thin (~0.5 mm) RBC-gel layer was suspended between two

thick (~2.5 cm) transparent gel layers. The RBC-gel layer becomes transparent in the locations where the RBCs are damaged by cavitation, likely because the cell content (hemoglobin) is released. The transparent damaged regions are visible within a few milliseconds, and become fully developed within 1 s. This period is likely the time required for sufficient hemoglobin to be released to the medium so that the light can penetrate through the damaged locations. The cavitation bubbles induced in the RBC phantom can be easily detected as dark shadows on backlit optical images. During the treatments, the cavitation bubbles and the lesions can be concurrently recorded, allowing for studying the direct impact of cavitation on the lesion development process.

To validate the cavitation memory effect on treatments in real tissues, experiments were also performed in freshly excised canine livers. The canine livers were obtained from healthy research canines, placed in degassed (20-30% gas saturation) saline at room temperature, and used within 3 hours of harvest. The liver tissues were sectioned into approximately 9 cm × 9 cm × 6 cm blocks and sealed in plastic bags filled with saline before experimentation.

3.2.1 Ultrasound generation and calibration

A custom-built 1-MHz F#-0.6 transducer was used to generate therapeutic ultrasound pulses. The transducer has 8 identical 2-inch diameter PZT disks mounted in an elliptical concaved plastic housing with 18 cm diameter in the long axis, 16 cm diameter in the short axis, and a radius of curvature of 106 mm (**Figure III-1a**). In the center of the housing is a 7 cm × 4 cm rectangular hole for the insertion of imaging

probes. The transducer was driven by electronic input signals generated by a programmed FPGA board (Altera cyclone II, San Jose, CA), and amplified by a custom-built class D amplifier.

The pressure waveform and beam profiles of the therapeutic ultrasound were obtained in degassed water under free field conditions using a custom-built fiber optic hydrophone with an active element of 100 μm in diameter [21]. Ultrasound pulses of 10 cycles in duration at 1 MHz center frequency were used in all treatments. The peak negative (P−) and peak positive (P+) pressures were 21 and 59 MPa, respectively (**Figure III-1b**). The −6-dB beamwidths were estimated on both P− and P+ pressure profiles at P−/P+ pressure of 18/48 MPa. The −6-dB beamwidths measured 1.2 mm along the long lateral axis, 1.3 mm along the short lateral axis, and 6.9 mm along the axial direction on the P− pressure profile. For the P+ profile, the −6-dB beamwidths measured 1.0 mm along the long lateral axis, 1.2 mm along the short lateral axis, and 4.8 mm along the axial direction. The beam profiles at the experimental pressure level could not be measured because of the interference from the bubble cloud at the fiber tip. In the experimental setting, the acoustic intensity could be attenuated during the propagation path in the tissues. Given the 0.5 dB/cm/MHz attenuation in the liver [22], and a 1 cm mean propagation path, the P− pressure was likely 20 MPa. The P+ pressure was likely decayed more significantly to <56 MPa due to nonlinear attenuation.

(a) (b)

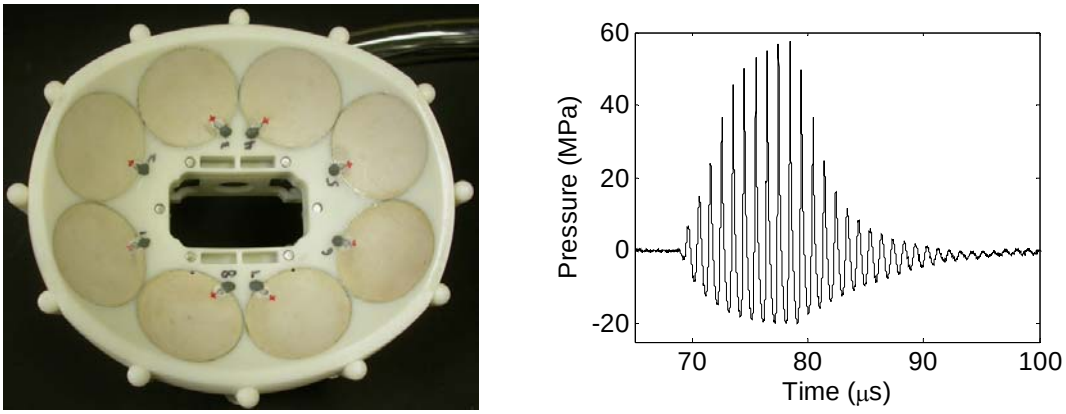

Figure III-1: (a) a picture of the therapeutic transducer, and (b) pressure waveform of the therapy pulse measured under free-field conditions in water.

3.2.2 Ultrasound treatment parameters

The treatments were performed using various time intervals (Δt) between successive pulses, with fixed doses of 500 pulses for the RBC phantoms and 1000 pulses for the *ex vivo* tissues. The intervals, Δt, varied from 2, 10, 20, 50, 100, to 200 ms in different treatments, as our previous study showed that the cavitation nuclei can persist up to several tens of ms after a histotripsy pulse [23]. These intervals were equal to or longer than those commonly used in the histotripsy treatments such that minimal thermal effects would occur in this study. A total of 65 treatments were performed on the RBC phantoms, resulting in a sample size of 10 – 12 for each Δt. A total of 26 *ex vivo* treatments were performed on the livers, resulting in a sample size of 4 – 5 for each.

3.2.3 Ultrasound treatment and monitoring

Before the treatment, the focus of the transducer was aligned with the RBC layer in the phantom using the following approach. A bubble cloud was first generated in the water using brief excitation of the transducer. The location of the bubble cloud was indicated using two 1-mm-wide 5-mW laser beams (Calpac lasers, Steamboat Springs, CO), one along and the other perpendicular to the ultrasound beam, crossed at the middle of the bubble cloud. The phantom was then placed in the tank such that the RBC layer was aligned with the laser beams and thus to the ultrasound beam and along the long axis of the transducer (**Figure III-2b**). For the *ex vivo* treatments, the tissue samples were positioned in a similar fashion.

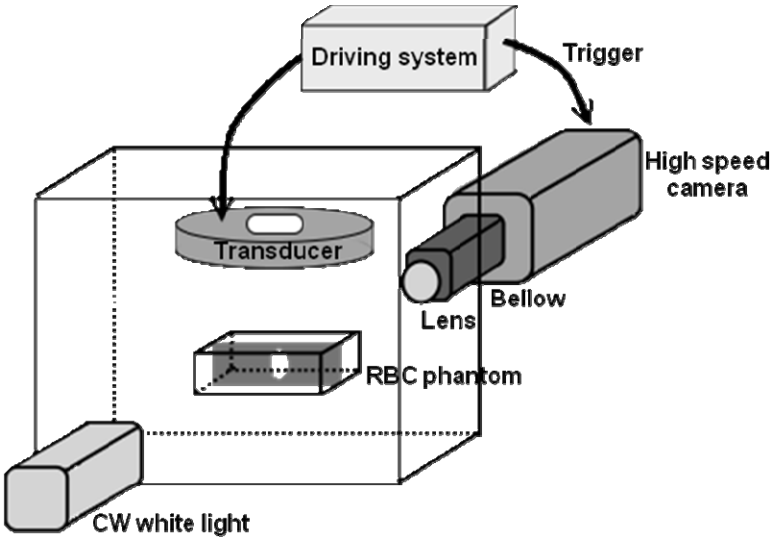

Figure III-2: Experimental setup. The transducer and the RBC phantom are submerged in a tank filled with degassed water (30% of normal saturation determined by pO_2). The high speed camera was mounted perpendicular to the ultrasound beam such that a projection of the bubble cloud and the lesions on the axial-lateral plane of the transducer were recorded.

During the treatment, the cavitataion bubble clouds and the lesions were imaged with a 12 bit, 1280 × 960 pixel high speed photography (Phantom 210, Vision Research, Wayne, NJ). Backlighting was provided using a 300 W continuous white light lamp. This lighting allowed for a short exposure of 2 μs for each frame. The frame size was adjusted to be 16 mm × 12 mm using a Tominon macro-bellows lens (Kyocera Optics, Nagano, Japan) attached to the camera. This image size ensured imaging of the overall bubble cloud and the entire lesion.

The imaging was performed after each pulse throughout the entire treatment. The bubbles were imaged 10 μs after the pulse because the spatial extent of the bubble cloud at this time corresponds well with that of the lesion [20]. The lesion image was taken at mid-period after the pulse when the cavitation bubbles disappeared on the optical images. This timing allowed for imaging of the lesions without interference from the bubbles for all Δt's used in this study. Because the lesions may take several milliseconds and up to 1 s to become fully developed, another lesion image was taken approximately 5 seconds after the entire treatments to ensure that the maximum extent of the damage was imaged.

3.2.4 Cavitation pattern analysis

The cavitation bubbles appeared as dark shadows on the backlit images (e.g., **Figure III-3a**), which can be easily distinguished from the background by the brightness. To detect the cavitation bubbles on the images, a pixel brightness threshold was set at the mean – 5 × standard deviation of the pixel brightness in a 2 mm × 2 mm region in the

intact background area (light gray area on the images). The pixels with intensities lower than this threshold were considered in the areas of the cavitation bubbles. Using this threshold, the grayscale image was converted to a binary bubble image where 1 (white) represented the presence of bubbles and 0 (black) represented the absence of bubbles (**Figure III-3b**).

The effects of varying intervals between successive pulses on the cavitation patterns were studied by measuring: 1) the similarity, i.e. cross correlation coefficient, between cavitation patterns in successive pulses, and 2) the integrated bubble area as the pulse number accumulated. The former assessed the level of the persistent cavitation memory. The latter indicated how fast the target volume can be completely "exposed" to or treated with the bubbles. The cross correlation coefficient between cavitation patterns was calculated using the following equation:

$$Cross\ correlation\ coefficient = \frac{\sum_i X_k(i) X_{k+1}(i)}{\sqrt{\sum_i X_k(i)^2}\sqrt{\sum_i X_{k+1}(i)^2}}$$

where $X_k(i)$ and $X_{k+1}(i)$ are the binary bubble images in the k-th and $(k+1)$-th pulses, and i is the pixel index on the images. This coefficient was computed for each pair of successive pulses through the entire treatment, i.e., $1 \leq k < 500$. To measure the integrated bubble area, an overlay of the bubble images was first formed for the k-th pulse by overlaying the binary bubble images from the first to the k-th pulse. The overlay image was also expressed in a binary format, where 1 indicated the presence of bubbles and 0 indicated the absence of bubbles in any pulse between the first and the k-th pulses. The integrated bubble area was computed by summing the areas with the presence of the

bubbles on the overlay of the bubble images. The overlay outlined a region that could potentially be damaged in the treatments. The increasing trend of the integrated bubble area as the pulse number accumulated may predict the lesion developing trend.

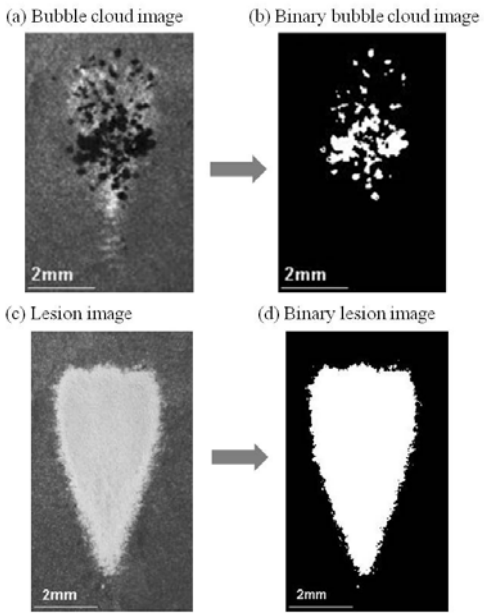

Figure III-3: Examples of converting the grayscale images to binary images for the cavitation bubble clouds (panel (a) to (b)) and the lesions (panel (c) to (d)).

3.2.5 Lesion analysis

The damaged areas were significantly brighter than the intact areas (e.g., **Figure III-3c**), and could be detected using a similar threshold approach. A pixel brightness threshold was set at the mean + 5 × standard deviation of the pixel brightness in a 2 mm × 2 mm region in the intact background area. Pixels with brightness higher than this threshold were considered "damaged." Using this threshold, the grayscale images were

converted to binary lesion images where 1 (white) represented “damaged area” and 0 (black) represented “intact area” (**Figure III-3d**).

To study the lesion development process, the following analysis procedures were performed. First, the treatment zone was selected on the post-treatment lesion image by outlining a region which encompassed the maximal extent of the lesion, and shaped like the overlay bubble image obtained in the previous section (*cavitation pattern analysis*). Next, the damaged area was calculated for each lesion image captured during the treatment by integrating the areas identified as “damaged” in the treatment zone. The damaged area was further normalized to the area of the treatment zone, resulting in the normalized damaged area. This normalized damaged area was compared for treatments using different time intervals between pulses.

3.2.6 Histological examination

Histological examination was conducted for the lesions produced in *ex vivo* tissues. After the treatments, the tissues were fixed in formalin and prepared for hematoxylin and eosin (H&E) sections. The lesions were sectioned longitudinally along the ultrasound beam. Multiple 4-μm thick H&E sections were made through the lesions with a 1-mm step size. The sections with the maximum spatial extent of damage both laterally and axially were examined.

3.3 Results

3.3.1 Cavitation patterns

Representative cavitation patterns induced during the treatments with decreasing time intervals between successive pulses are shown in **Figure III-4**. The locations of the cavitation bubbles in response to each pulse were highly dependent on the time interval. When Δt was $\geq$ 100 ms, the cavitation bubbles were induced at distinctly different locations in response to each pulse. As Δt was decreased to less than 100 ms, many bubbles appeared at the same locations in each pulse. This repeated pattern was most prominent at the beginning of the treatment, and became less significant as the pulse number increased.

The spatial extent of the bubble cloud was also affected by Δt. The bubble cloud appeared in a more confined area when Δt was $\geq$ 100 ms, and expanded as Δt decreased from 100 to 10 ms. As Δt further decreased to 2 ms, the bubble cloud was as large as that produced with Δt ranging between 100 - 10 ms at the beginning of the treatment, but appeared in a much smaller area around the center of the focus as the pulse number increased.

The cross correlation coefficients between the cavitation patterns produced in successive pulses with varying Δt's are plotted in **Figure III-5**. The cross correlation coefficient decreased exponentially with increasing Δt's. This exponential decrease was particularly significant at the beginning of the treatment (i.e., within 100 pulses). For example, the correlation coefficient at the 10^{th} pulses during the treatments with varying Δt's deceased from 0.5 ± 0.1 to 0.1 ± 0.1 as Δt increased from 2 to 200 ms. These data

were well fitted by an exponential curve (R^2=0.96, **Figure III-5a**). The exponential decay in the correlation coefficient became less significant as the treatment continued because the correlation coefficient might change with increasing numbers of pulses (**Figure III-5 b-f**). At the longest Δt (i.e., 200 ms), the cross correlation coefficient remained low at 0.1 ± 0.1 throughout the entire treatment. When Δt decreased to ≤ 20 ms, the correlation coefficient decreased from ~0.5 to ~0.1 as the pulse number increased from 0 to 500.

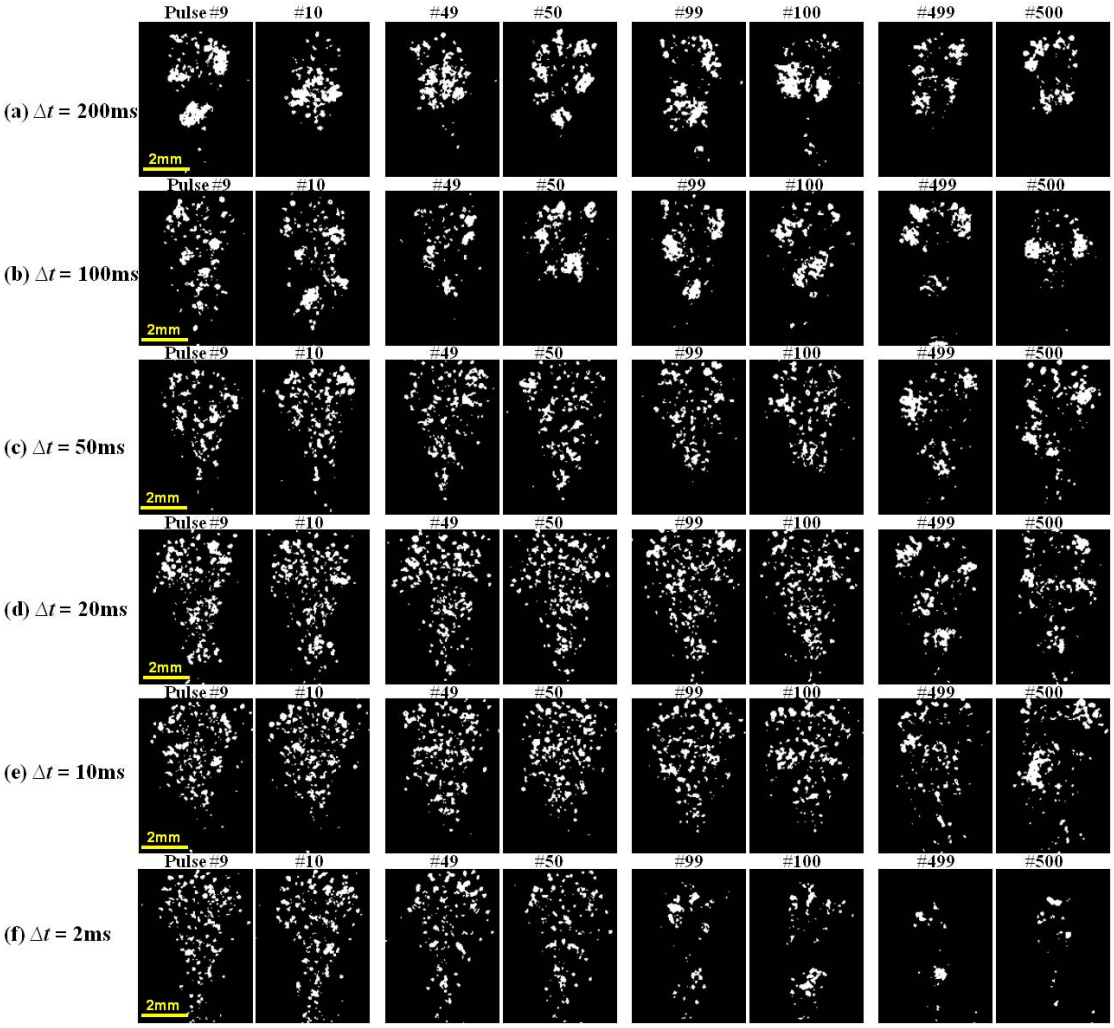

Figure III-4: Cavitation patterns generated by successive pulses (pulses #9 and #10, #49 and #50, #99 and #100, #499 and #500) during the treatments when the time interval between pulses, Δ*t*, decreased from (a) 200 to (f) 2 ms. The cavitation patterns in successive pulses appeared distinctly different in response to each pulse when Δ*t* was long (e.g., panel (a)), but they were relatively similar when Δ*t* was decreased (e.g., panel (f)).

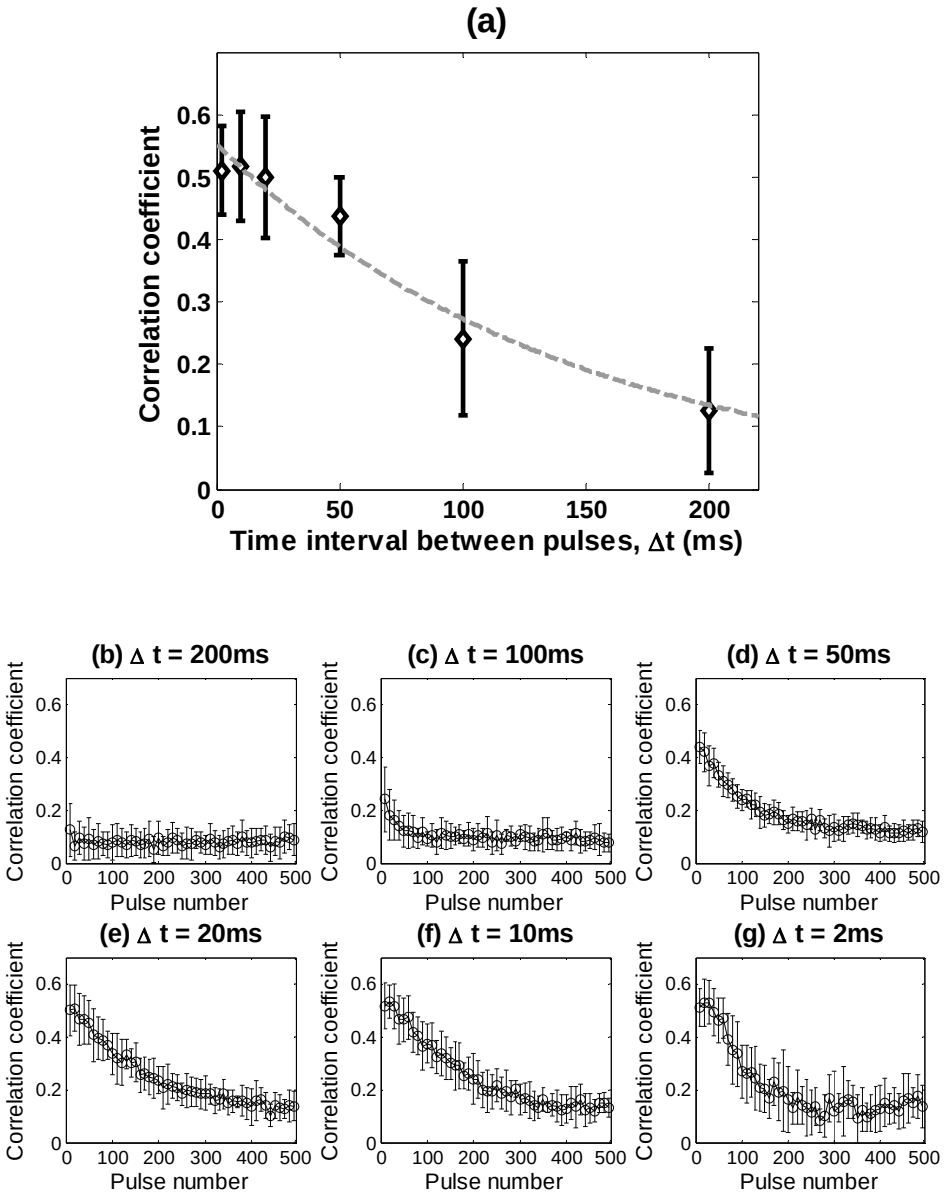

Figure III-5: Cross correlation coefficients of cavitation patterns induced in successive pulses for decreasing time intervals between pulses. The correlation coefficient decreased exponentially with increasing Δt's at the beginning of the treatment (<100 pulses). As an example, the correlation coefficients at the 10th pulse is shown in panel (a) (dashed line: $y=0.55e^{-7.06t}$, $R^2=0.96$). The exponential decay in the correlation coefficient became less significant later as the pulse number increased because the correlation coefficient might change (panels (b)-(f)). Data is presented in mean ± standard deviation (N = 10-12 each).

The overlay of the bubble images during the treatments with decreasing Δt's are shown in **Figure III-6**. When Δt was long, the bubbles occurred at random locations in each pulse. Therefore, the focal volume was fully exposed to the cavitation bubbles within a small number of pulses. When Δt was decreased, the focal volume was not fully exposed to the cavitation bubbles until a larger number of pulses were delivered. For instance, the focal volume was fully exposed to the bubbles within 100 pulses at Δt = 200 ms (**Figure III-6a**); however, it was not fully exposed until 500 pulses were delivered when Δt was decreased to 50 ms (**Figure III-6c**). When Δt was further decreased, some regions in the focal volume were never exposed to the cavitation bubbles during the entire treatment (**Figure III-6e** and **f**).

The integrated bubble areas during the treatments with varying Δt's are shown in **Figure III-7**. When Δt was $\geq$ 100 ms, the integrated bubble area rapidly increased with each additional pulse at the beginning of the treatment, and reached a plateau at 100 pulses (**Figure III-7a** and **b**). This trend indicated that the target volume was fully exposed to the cavitation bubbles within a small number of pulses. As Δt was decreased from 100 to 10 ms, the increase in the integrated bubble areas slowed down, and a plateau was never observed within 500 pulses (**Figure III-7c** and **e**). When Δt was decreased to 2ms, a plateau in the integrated bubble area was observed again (**Figure III-7f**). This plateau occurred for a different reason: the spatial extent of the bubble cloud decreased as the pulse number increased, thus limiting the growth of the overall bubble coverage area. This behavior is evidenced in **Figure III-4f** as well where the spatial extent of the bubble cloud is limited in later pulses.

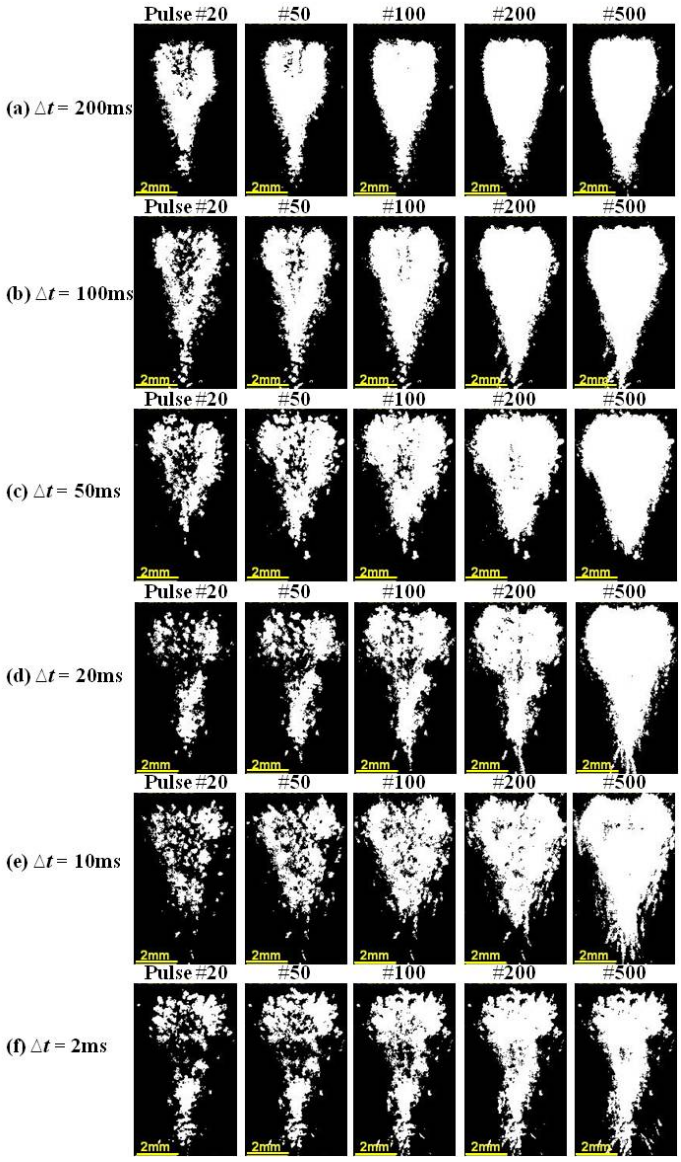

Figure III-6: Overlay of the bubble images during the treatments when the time intervals between pulses decreased from (a) 200 to (f) 2 ms. When Δ*t* was long, the focal volume was fully exposed to the cavitation bubbles within a small number of pulses (panel (a)). The number of pulses needed for the focal volume to be fully exposed to cavitation increased when Δ*t* was decreased. When Δ*t* was too short, full exposure could not be achieve within 500 pulses, and islands of untreated areas were present after the treatments (panels (e) and (f)).

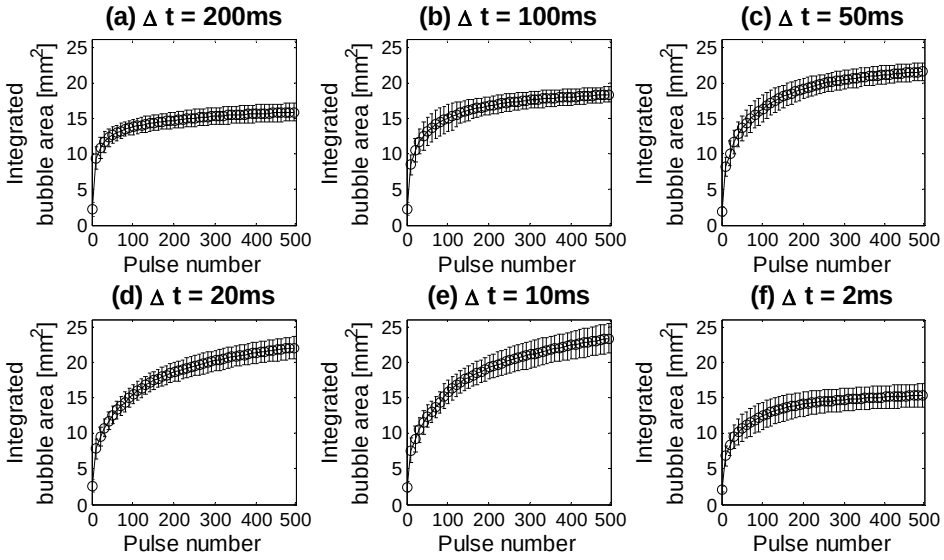

Figure III-7: Integrated bubble areas with increasing pulse numbers when the time intervals between pulses decreased from (a) 200 to (f) 2 ms. The integrated bubble area increased rapidly and reached a plateau when Δt was long. When Δt was decreased, the increasing trend slowed down, and the plateau was not observed. When Δt was decreased to 2 ms, a plateau occurred again because the decreased spatial extent of the bubble cloud limited the growth of the integrated bubble area. Data is presented in mean ± standard deviation (N = 10-12).

3.3.2 Lesion development process

Representative lesion images during the treatment illustrate the lesion development process with decreasing Δt's (**Figure III-8**). In all treatments, damaged areas were detected after each pulse. The damaged area increased with increasing pulse numbers. The lesion developed more rapidly with each pulse for longer Δt's. Furthermore, the lesion appeared to be homogeneously treated, and possessed a smooth and well-defined boundary with no or very few residual intact areas in the treatment zone. As Δt was decreased, the lesions presented a ragged boundary with many residual intact areas.

The normalized damaged areas during the treatments with different Δt's are shown in **Figure III-9**. The normalized damaged area increased more rapidly with each pulse when Δt was $\geq$ 100 ms. This increase slowed down as Δt decreased from 100 to 10 ms. The slowest increase was found at the shortest Δt, i.e., 2 ms. After the treatments, complete fractionation of the treatment zone (i.e., 100% damage) was achieved only when Δt was $\geq$ 50 ms. The normalized damaged area decreased when Δt was decreased. At Δt = 2 ms, only 50% of the treatment zone was damaged after the treatment. To compare the treatment efficiency for different Δt's, the dose required to achieve 25% damage was calculated (**Figure III-9b**). As Δt increased from 2 to 200 ms, the dose required for 25% damage decreased from 199 ± 50 to 17 ± 9 pulses, approximately a 12-fold difference. This indicated that the treatment efficiency (defined as damage per pulse) was significantly higher for long Δt's.

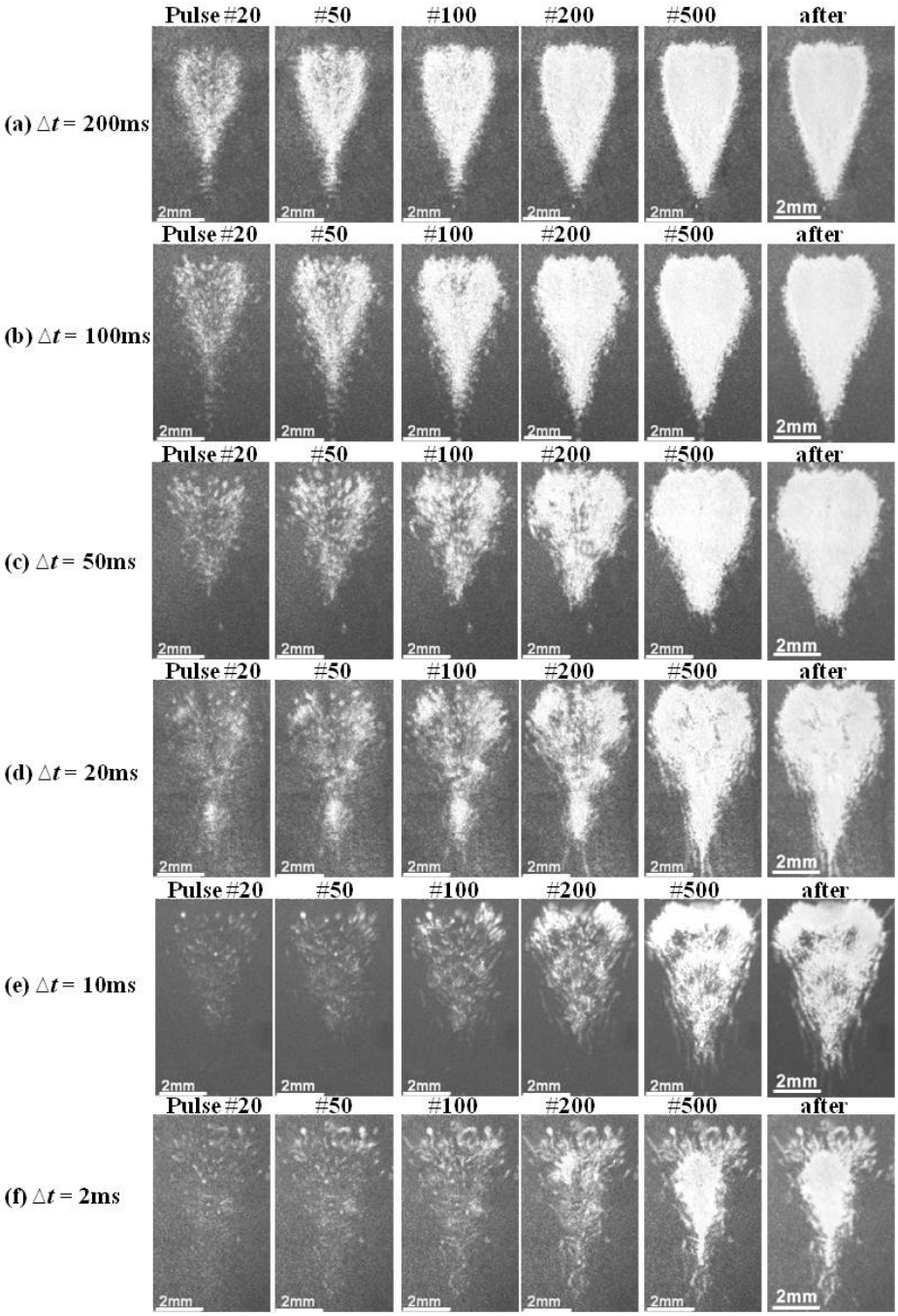

Figure III-8: The lesion patterns observed during and after the treatments when the time intervals between pulses decreased from (a) 200 to (f) 2 ms. At long Δt's, the damaged area rapidly expanded with each pulse; completely fractionated lesions were observed after the treatments. At short Δt's, the damaged area developed slowly with each pulse; incompletely treated lesions with islands of untreated areas were observed after the treatments.

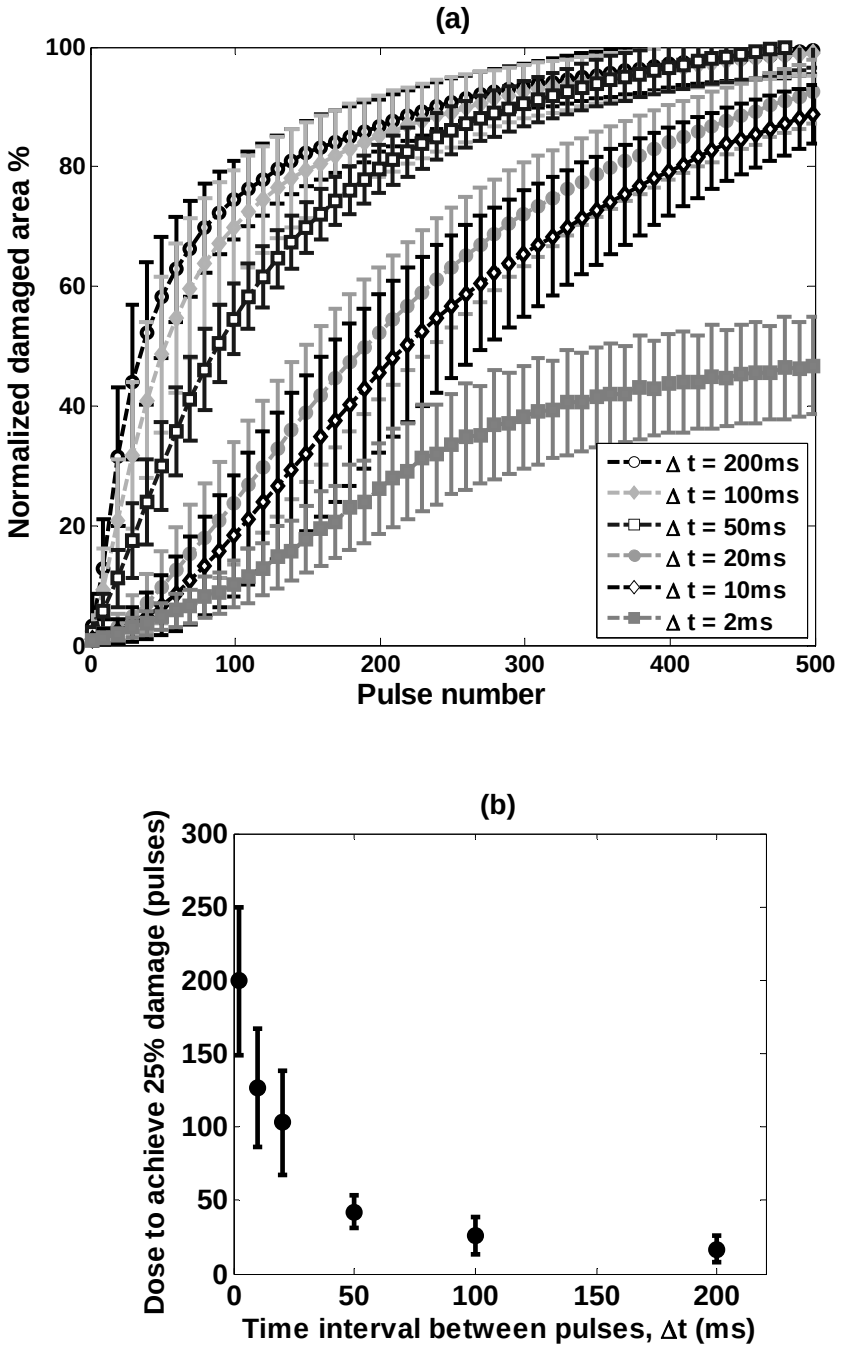

Figure III-9: (a) Normalized damaged areas during the treatments with different time intervals between pulses, Δt's. Lesions produced with longer Δt's developed significantly faster with each pulse than those produced with shorter Δt's. Complete disruption of the treatment zone was achieved only when Δt was ≥ 50ms. (b) Dose to achieve 25% damage for different Δt's. The required dose was reduced by approximately 12 fold as Δt increased from 2 to 200 ms. Data is presented in mean ± standard deviation (N = 10-12).

3.3.3 Ex vivo study

The *ex vivo* treatment results confirmed that the lesion morphology was highly dependent on the time intervals between pulses. With 1000 pulses applied, when Δt was $\geq$ 100 ms, the lesions appeared to be homogeneously and completely disrupted with no or very few recognizable tissue structures in the treatment zone (**Figure III-10a** and **b**). As Δt decreased to 50 − 20 ms, islands of incompletely disrupted structures were present in the midst of the mostly treated zone (**Figure III-10c** and **d**). As Δt further decreased to below 20 ms, a significant amount of structurally intact tissues remained in the treatment zone (**Figure III-10e** and **f**). These results demonstrated that when the dose was held small, complete tissue disruption was more likely achieved when Δt was increased.

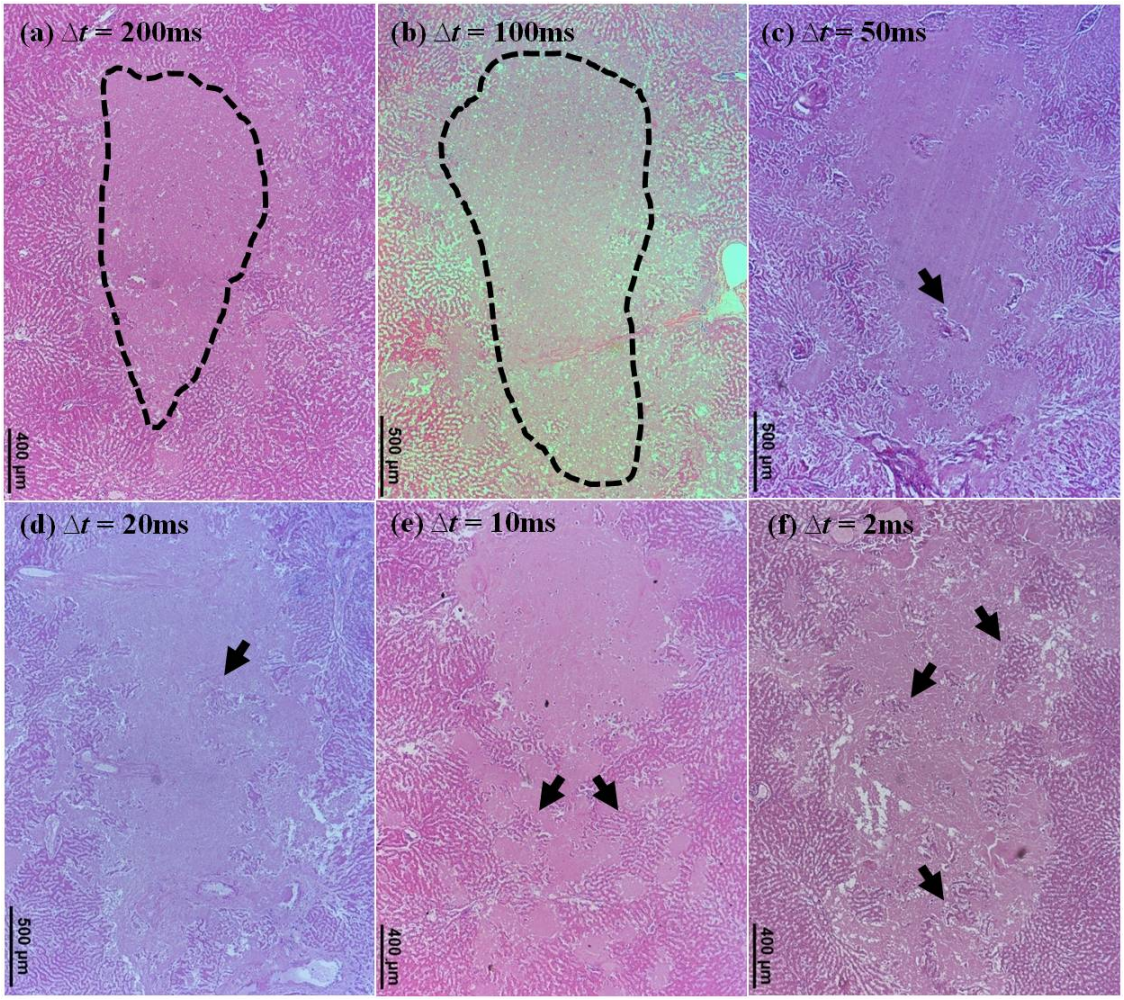

Figure III-10: Lesions produced in *ex vivo* livers using 1000 pulses when the time intervals between pulses decreased from (a) 200 to (f) 2 ms. When Δt was ≥100 ms, completely homogenized lesions were observed (outlined by the dashed lines in panels (a) and (b)). As Δt decreased, isolated islands of structurally intact areas were observed in the treatment volume (for example, the areas indicated by the arrows in panels (c)-(f)). More islands of structurally intact areas appeared as Δt further decreased.

3.4 Discussion and Conclusions

We hypothesized that the cavitation memory may be removed by applying the subsequent pulse after a sufficiently long time interval following the previous pulse and that the removal of the memory may lead to complete and homogeneous tissue fractionation with fewer pulses. These hypotheses were supported by the results. At short time intervals between pulses, the highly correlated cavitation patterns indicated the presence of the cavitation memory. When the time interval between pulses was increased, the memory disappeared. As a result, the cavitation bubbles occurred in random locations in response to each pulse. The random patterns allowed the target volume to be fully exposed to cavitation within a significantly smaller number of pulses, leading to complete and homogeneous tissue fractionation with dramatically fewer pulses.

Despite the benefits of treatments with increased time interval between pulses, the total treatment time can be long if a large volume of tissue is treated by one single focal spot at a time. Since histotripsy pulses are only a few microseconds long, we propose using a 2-D phased-array to steer the focus electronically to other locations within the treatment volume during the time between pulses (~100ms). As such, the entire volume can be completely fractionated using the same time that is needed to fractionate a single focal spot. In this way, the treatment time to ablate a large tissue volume may be significantly reduced by increasing the duty cycle of the phased array transducer.

To remove the cavitation memory, this study used a passive approach by increasing the time interval between pulses. In addition to this passive approach, active approaches can be used. For example, we have previously demonstrated that the persistent bubbles in the periphery of the focus can be actively removed by a nuclei

preconditioning pulse delivered before each therapy pulse [24, 25]. A similar pulsing sequence may be developed to remove the persistent nuclei in the treatment volume. This pulsing sequence, if successfully developed, uses a special pulse to remove the cavitation memory immediately after each pulse. As soon as the cavitation memory is removed, the next therapy pulse can be delivered. Therefore, the time interval between successive pulses for the memory effect to disappear may be substantially reduced.

Although the presence of the cavitation memory caused highly correlated cavitation patterns at the beginning of the treatment, this correlation gradually decreased as the treatment continued. This decreasing correlation likely occurred because the progressive fractionation of the treatment volume, which eventually turned the treatment tissue volume to liquefied homogenate, provided increased mobility for the persistent cavitation nuclei. The similarity between cavitation patterns was therefore decreased. Since this change only occurred in the later stage of the treatment, the overall treatment efficiency remained low compared to that of the treatments with uncorrelated cavitation patterns during the entire treatment.

The decreasing trend in the correlation coefficient of the cavitation patterns with increasing Δt's indicated that the memory effects decayed exponentially with time and disappeared in several tens to hundreds of ms. The decay trend and period corresponded well with those of the residual bubbles that persisted in the treatment volume after a histotripsy pulse [23]. The decay period also corresponded well with the dissolution time of micron size gas bubbles [26-28]. These suggested that the persistent gas bubbles are an important source causing the memory effect. It is not excluded that the fragments of

fractionated tissues or tissue phantoms may also serve as potential cavitation nuclei that contribute to the memory effect.

The normalized damaged area measured during the treatments (**Figure III-9a**) may be slightly underestimated due to the limitation in the temporal response of the RBC phantoms. The damage was imaged 1 – 100 ms after each pulse; however, it may take several milliseconds for the lesions to become fully developed. This latency could have caused different amount of underestimation for various Δt's. To evaluate the amount of underestimation, the damaged areas measured at the last pulse of the treatments and 5 s after the treatments (two rightmost columns in **Figure III-8**) were compared. The difference between the two measurements were found to be 0.1 - 1.2 mm^2, with the maximum occurring for Δt = 2ms. In the worst case, this difference would cause an underestimation of the normalized damaged area by 7%. This amount is small compared to the difference caused by different experimental conditions, and thus should have minimal influence on the trends observed in **Figure III-9**.

An interesting evolutionary trend of the bubble cloud induced at the shortest time interval between pulses (i.e., 2ms), or the highest pulsing rate, was observed. The spatial extent of the bubble cloud decreased to a smaller area around the focal center as the pulse number increased. This phenomenon may have resulted from significant decrease in the available cavitation nuclei in the treatment volume. The available cavitation nuclei in the target volume could have been quickly depleted after repetitive pulsing at a high pulsing rate [29]. In addition, the short interval between pulses could have impeded the replenishment of new cavitation nuclei from the surrounding area. The depletion of the available nuclei may have raised the cavitation threshold in the treatment volume,

therefore restricting bubbles in a smaller area where the pressure amplitude remained above the new threshold. Further investigation is needed to distinguish the mechanisms behind this phenomenon.

3.5 Conclusions

This study demonstrated that cavitation memory may have distinct influence on the lesion development process in histotripsy. The cavitation memory effect resulted in highly correlated cavitation patterns, leading to slow development of lesions with each pulse. The removal of the memory effect caused cavitation bubbles to occur in new random locations in response to each pulse, resulting in complete and homogeneous tissue disruption with significantly fewer pulses, .i.e., more dose-efficient treatments. Moreover, in real-time monitoring of lesion development, homogeneously disrupted lesions should result in tissue characterization metrics representative of the whole lesion instead of a misleading average of fully homogenized and non-homogenized zones. This may be potentially important in image-guided cancer therapy.

3.6 References

[1] T. G. Leighton, The acoustic bubble: Academic Press, 1997.

[2] H. G. Flynn and C. C. Church, "A mechanism for the generation of cavitation maxima by pulsed ultrasound," J Acoust Soc Am, vol. 76, pp. 505-12, Aug 1984.

[3] E. N. Harvey, D. K. Barnes, W. D. McElroy, A. H. Whiteley, D. C. Pease, and K. W. Cooper, "Bubble formation in animals. I. Physical factors," J. Cell. Comp. Physiol., vol. 24, pp. 1-22, Aug. 1944 1944.

[4] F. E. Fox and K. F. Herzfeld, "Gas Bubbles with Organic Skin as Cavitation Nuclei," J. Acoust. Soc. Am., vol. 26, pp. 984-989, 1954.

[5] E. N. Harvey, D. K. Barnes, W. D. McElroy, A. H. Whiteley, D. C. Pease, and K. W. Cooper, "Bubble formation in animals. II. Gas nuclei and their distribution in blood and tissues," J. Cell. Comp. Physiol., vol. 24, pp. 23-34, Aug. 1944 1944.

[6] J. B. Fowlkes and L. A. Crum, "Cavitation threshold measurements for microsecond length pulses of ultrasound," J Acoust Soc Am, vol. 83, pp. 2190-201, Jun 1988.

[7] A. Henglein and M. Gutierrez, "Chemical reactions by pulsed ultrasound: memory effects in the formation of NO3- and NO2- in aerated water," Int J Radiat Biol Relat Stud Phys Chem Med, vol. 50, pp. 527-33, Sep 1986.

[8] O. Yavas, P. Leiderer, H. K. Park, C. P. Grigoropoulos, C. C. Poon, and A. C. Tam, "Enhanced acoustic cavitation following laser-induced bubble formation: Long-term memory effect," Phys Rev Lett, vol. 72, pp. 2021-2024, Mar 28 1994.

[9] M. Arora, L. Junge, and C. D. Ohl, "Cavitation cluster dynamics in shock-wave lithotripsy: part 1. Free field," Ultrasound Med Biol, vol. 31, pp. 827-39, Jun 2005.

[10] X. Xi and P. Zhong, "Improvement of stone fragmentation during shock-wave lithotripsy using a combined EH/PEAA shock-wave generator-in vitro experiments," Ultrasound Med Biol, vol. 26, pp. 457-67, Mar 2000.

[11] M. Delius and W. Brendel, "A model of extracorporeal shock wave action: tandem action of shock waves," Ultrasound Med Biol, vol. 14, pp. 515-518, 1988.

[12] A. M. Loske, F. E. Prieto, F. Fernandez, and J. van Cauwelaert, "Tandem shock wave cavitation enhancement for extracorporeal lithotripsy," Phys Med Biol, vol. 47, pp. 3945-57, Nov 21 2002.

[13] P. Huber, J. Debus, K. Jochle, I. Simiantonakis, J. Jenne, R. Rastert, J. Spoo, W. J. Lorenz, and M. Wannenmacher, "Control of cavitation activity by different shockwave pulsing regimes," Phys Med Biol, vol. 44, pp. 1427-37, Jun 1999.

[14] J. E. Parsons, C. A. Cain, G. D. Abrams, and J. B. Fowlkes, "Pulsed cavitational ultrasound therapy for controlled tissue homogenization," Ultrasound Med. Biol., vol. 32, pp. 115-129, Jan 2006.

[15] Z. Xu, J. B. Fowlkes, and C. A. Cain, "A new strategy to enhance cavitational tissue erosion using a high-intensity, initiating sequence," IEEE Trans. Ultrason., Ferroelect., Freq. Contr., vol. 53, pp. 1412-1424, Aug 2006.

[16] Z. Xu, J. B. Fowlkes, E. D. Rothman, A. M. Levin, and C. A. Cain, "Controlled ultrasound tissue erosion: the role of dynamic interaction between insonation and microbubble activity," J. Acoust. Soc. Am., vol. 117, pp. 424-435, Jan 2005.

[17] W. W. Roberts, T. L. Hall, K. Ives, J. S. Wolf, Jr., J. B. Fowlkes, and C. A. Cain, "Pulsed cavitational ultrasound: a noninvasive technology for controlled tissue ablation (histotripsy) in the rabbit kidney," J. Urol., vol. 175, pp. 734-738, Feb 2006.

[18] T.-Y. Wang, Z. Xu, F. Winterroth, T. L. Hall, J. B. Fowlkes, E. D. Rothman, W. W. Roberts, and C. A. Cain, "Quantitative Ultrasound Backscatter for Pulsed Cavitational Ultrasound Therapy - Histotripsy," IEEE Trans. Ultrason. Ferroelectr. Freq. Control., vol. 56, pp. 995-1005, 2009.

[19] F. L. Lizzi, M. Astor, T. Liu, C. Deng, D. J. Coleman, and R. H. Silverman, "Ultrasonic spectrum analysis for tissue assays and therapy evaluation," Intl. J. Imaging Sys. Tech., vol. 8, pp. 3-10, 1997.

[20] A. D. Maxwell, T.-Y. Wang, L. Yuan, A. P. Duryea, Z. Xu, and C. A. Cain, "A tissue phantom for evaluation of mechanical damage caused by cavitation," Ultrasound Med. Biol., vol. 36, pp. 2132-2143, Dec 2010.

[21] J. E. Parsons, C. A. Cain, and J. B. Fowlkes, "Cost-effective assembly of a basic fiber-optic hydrophone for measurement of high-amplitude therapeutic ultrasound fields," J. Acoust. Soc. Am., vol. 119, pp. 1432-1440, Mar 2006.

[22] K. J. Parker, M. S. Asztely, R. M. Lerner, E. A. Schenk, and R. C. Waag, "In-vivo measurements of ultrasound attenuation in normal or diseased liver," Ultrasound Med Biol, vol. 14, pp. 127-36, 1988.

[23] Z. Xu, T. L. Hall, J. B. Fowlkes, and C. A. Cain, "Optical and acoustic monitoring of bubble cloud dynamics at a tissue-fluid interface in ultrasound tissue erosion," J. Acoust. Soc. Am., vol. 121, pp. 2421-2430, Apr 2007.

[24] T.-Y. Wang, T. L. Hall, Z. Xu, J. B. Fowlkes, and C. A. Cain, "Local cavitation suppression using cavitation nuclei preconditioning for precise treatment in histotripsy," in Proc. IEEE Ultrason. Symp., 2010.

[25] T.-Y. Wang, Z. Xu, T. Hall, J. B. Fowlkes, W. W. Roberts, and C. A. Cain, "Active focal zone sharpening for high precision treatment using histotripsy " IEEE Trans. Ultrason., Ferroelect., Freq. Contr., pp. 305 - 315, Feb. 2011.

[26] P. S. Epstein and M. S. Plesset, "On the Stability of Gas Bubbles in Liquid-Gas Solutions," J. Chem. Phys., vol. 18, pp. 1505-1509, 1950.

[27] W. S. Chen, T. J. Matula, and L. A. Crum, "The disappearance of ultrasound contrast bubbles: observations of bubble dissolution and cavitation nucleation," Ultrasound Med Biol, vol. 28, pp. 793-803, Jun 2002.

[28] K. Ferrara, R. Pollard, and M. Borden, "Ultrasound Microbubble Contrast Agents: Fundamentals and Application to Gene and Drug Delivery " Annu. Rev. Biomed. Eng., vol. 9, pp. 415-447, 2007.

[29] B. M. Borkent, M. Arora, and C. D. Ohl, "Reproducible cavitation activity in water-particle suspensions," J Acoust Soc Am, vol. 121, pp. 1406-12, Mar 2007.

CHAPTER IV. IMAGING FEEDBACK FOR HISTOTRIPSY WITH BACKSCATTER INTENSITY ANALYSIS

4.1 Introduction

Imaging feedback of the tissue treatment effects is critical for non-invasive tissue ablation techniques. It allows the operating clinician to monitor the treatment progress and determine the endpoint of the treatment. In order to estimate tissue damage, several methods have been investigated for ultrasound thermal therapies. Magnetic resonance (MR) imaging has been shown to provide accurate estimation of the temperature change in the treated tissue [1-4]. The drawback of the magnetic resonance imaging is the relatively high cost and the requirement of MR compatible ultrasound system. Several ultrasound imaging methods have also been investigated to monitor the thermal tissue damage by measuring the changes in tissue elasticity, sound velocity, and acoustic attenuation [5-10]. These techniques are still in being researched for feasibility and efficacy.

In comparison, the fractionated tissue volume produced by histotripsy can be visualized clearly as a hypoechoic region using standard ultrasound B-mode imaging. This hypoechoic region implies significant reduction in ultrasound backscatter from the histotripsy-treated volume. The backscatter reduction can be seen in real-time during and

immediately after the treatment. This phenomenon likely occurs because tissue is mechanically subdivided into small fragments that cannot effectively scatter ultrasound at the imaging frequency used [11]. Based on this finding, we hypothesize that ultrasound backscatter gradually decreases as histotripsy progressively fractionates the sources of ultrasound scattering in tissue. Therefore, the change in ultrasound backscatter may be used to quantitatively predict the degree of tissue fractionation in real time, i.e., the treatment effect and progression of histotripsy.

This chapter studies the quantitative relationship between the ultrasound backscatter intensity and the degree of tissue fractionation. Each histotripsy pulse is hypothesized to fractionate a portion of tissue. An increasing number of successive histotripsy pulses can result in cumulative tissue fractionation. With a sufficient number of pulses, a tissue volume can be completely fractionated. Therefore, different degrees of tissue fractionation may be produced by varying the number of histotripsy pulses.

The degree of tissue fractionation is evaluated histologically by the percentage of intact cells remaining in the treatment volume. The intactness of a cell is determined by the appearance of its cell nucleus on histology. The cell nucleus is selected because it is a common indication of cell damage or death. More importantly, it has been observed to be more resistant to mechanical damage generated by histotripsy than other cellular components or organelles [12]. The quantitative correlation between the percentage of remaining normal appearing cell nuclei and backscatter intensity may provide the basis for a real-time image-based feedback metric for a histotripsy treatment, predicting a local clinical outcome.

4.2 Materials and Methods

4.2.1 Tissue preparation

In vitro experiments were conducted in fresh porcine kidneys obtained from a local abattoir. The kidneys were preserved in degassed saline at room temperature and used within 6 hours of harvest. The renal capsule was removed, and the collecting system of each kidney was flushed with degassed saline through the ureter to remove trapped air. More details of the kidney preparation process were described in our previous publication [13]. The flushed kidneys were then sealed in Ziploc bags filled with saline, mounted to a motorized 3-axis positioning system (Parker Hannifin, Rohnert Park, CA), and submerged in a tank of degassed, deionized water during experimentation.

4.2.2 Histotripsy therapeutic ultrasound

A 1-MHz annular array transducer (Imasonic, Besancon, France) was used to generate therapeutic ultrasound pulses. The transducer has a 100-mm outer diameter, a 40-mm inner diameter, and a 90-mm geometric focal length. The 16 annular elements were driven synchronously to work as a single element transducer focused at the geometric focus. The input electronic signals to the therapeutic ultrasound were delivered by a function generator (Model 3314A, Agilent Technology, Palo Alto, CA, USA), and amplified by a custom-built driving circuit. The therapeutic transducer driving circuit shares similar design with our other transducer driving systems [14, 15].

The acoustic field was calibrated in degassed water with a custom-built fiber optic hydrophone system with a 100-μm diameter sensitive element [16]. Ultrasound pulses of 15 acoustic cycles in duration delivered at a pulse repetition frequency (PRF) of 100 Hz were used in all treatments. The peak negative and positive pressures were measured to be 19 MPa and 125 MPa, respectively (**Figure IV-1**). The -6dB beamwidths were measured 1.9 mm laterally and 15 mm axially at 5 MPa peak negative pressure. The beamwidths decreased with increasing pressures. The beamwidths at the pressure used for tissue treatment could not be successfully measured because the high pressure would induce cavitation at the fiber tip within a few pulses. The fiber tip would be damaged after several cavitation events during the pressure profile scan. The spatial peak pulse average intensity (I_{SPPA}) and the spatial average temporal average intensity (I_{SATA}) were calculated from the free field measurements using the definitions described by the American Institute of Ultrasound in Medicine [17]. The I_{SPPA} was calculated 39 kW/cm^2. The I_{SATA} calculated based on the -6dB cross-sectional beam area at 5MPa was 27 W/cm^2. The above measurements reported here were obtained under free-field conditions. Given the 1 dB/cm/MHz sound attenuation in the porcine kidney [18], a 1-cm mean path length in tissue, and a 1-MHz center frequency, the peak negative pressure in tissue is likely 17 MPa. However, this calculation only accounts for the absorption of the fundamental harmonic but not that of the higher harmonics generated at high pressures due to the nonlinearity of the medium. These higher harmonics should attenuate faster than lower frequencies, resulting in a substantial decay of the positive pressures.

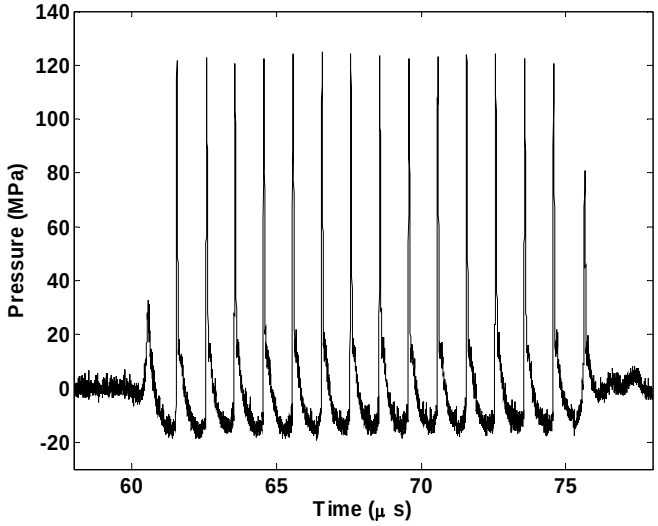

Figure IV-1: 15 cycle pulse at 1 MHz measured in water with a fiber optic hydrophone system.

4.2.3 Ultrasound image guidance for histotripsy treatment

The histotripsy treatment consisted of three general steps, all of which were guided by ultrasound imaging. First, the therapy focus was localized to the targeted tissue region prior to the treatment. Histotripsy pulses were used to create a bubble cloud in water, which appeared as a hyperechoic zone on the ultrasound image, and was marked as the therapy focus (**Figure IV-2a**). Targeting was achieved by aligning the focus marker to the tissue to be treated on ultrasound image (**Figure IV-2b**). A small number of histotripsy pulses (<100 pulses) at the treatment pressure level were applied again to generate a bubble cloud in the tissue to verify the targeting accuracy (**Figure IV-2c**). The number of targeting pulses is small compared to the lowest dose (2700 pulses/lesion) for tissue treatment. No significant tissue damage was generated by this targeting procedure

alone on histology. Second, histotripsy treatment was applied, and the treatment was monitored by actively cavitating bubble clouds, which appeared as a dynamically changing hyperechoic region on ultrasound images. Third, the treatment was completed when the designated number of pulses was achieved in the target volume.

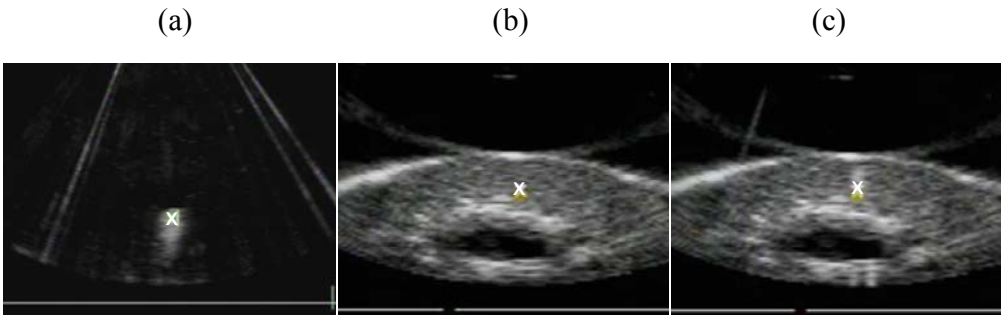

Figure IV-2: Ultrasound imaging of targeting and monitoring of histotripsy treatment using the 5-MHz imaging probe. Therapeutic ultrasound propagated from top to bottom of the images. (a) Prior to the treatment, a bubble cloud was generated in water and seen on ultrasound image as a hyperechoic region, which was marked as the treatment focus ("X"). (b) The focus marker was aligned with the targeted volume in the kidney on a pre-treatment ultrasound image. (c) A bubble cloud was generated in the target volume to verify the target accuracy.

Ultrasound imaging of the treatment plane was achieved using two imaging probes, a 5 MHz phased array and a 10 MHz linear array, both used with a clinical diagnostic ultrasound system (GE System Five, Milwaukee, WI, USA). The 5 MHz probe has 96 elements and an aperture size of 14 mm, focused 8 cm at the targeted tissue region. The 5 MHz imaging probe was used for target localization and monitoring of the treatment. It ensured that the bubble cloud activity occurred within the targeted volume, and that the lesions were successfully generated. It was inserted in the center hole of the therapy

transducer, and imaged the therapy plane during the treatment using unsynchronized real-time B-mode imaging. The cloud activity and lesion formation could be clearly visualized using unsynchronized B-mode imaging because the therapy pulses were so short that only a few scanlines were corrupted with the interference from the therapy pulse (e.g., the radial lines in **Figure IV-2c**). The 10 MHz imaging probe was used to collect higher-resolution backscatter signals before and immediately after the treatment. The 10-MHz probe has 64 elements, a full array size of 44 mm, and an aperture size of 9.3 mm. It was positioned close to the tissue (3 cm from the tissue surface) and focused at 4 cm in the targeted treatment volume. The positions of the two imaging probes and the therapy transducer with respect to the tissue are illustrated in **Figure II-1**. The tissue was moved to be scanned by the 10-MHz imaging probe before and immediately after treatments according to a pre-determined displacement. To measure the displacement between the imaging planes of the two probes, two crossed wires, one along the lateral axis and the other along the elevational axis of the imaging probes, were mounted to the positioning system and placed where the kidney would be in **Figure II-1**. The relative displacement of the positions at which the wire intersection appeared in the centers of the two imaging planes was determined as the displacement of the two imaging probes. Standard ultrasound B-scan IQ image frames were collected from the 10 MHz imaging probe, and stored in the built-in EchoPac image archive system for later processing. The transmit power and receive gain of the imaging system were adjusted for clear visualization of the kidney cortex and remained unchanged during the experiments. This setup permitted comparisons between pre- and post-treatment ultrasound backscatter intensity.

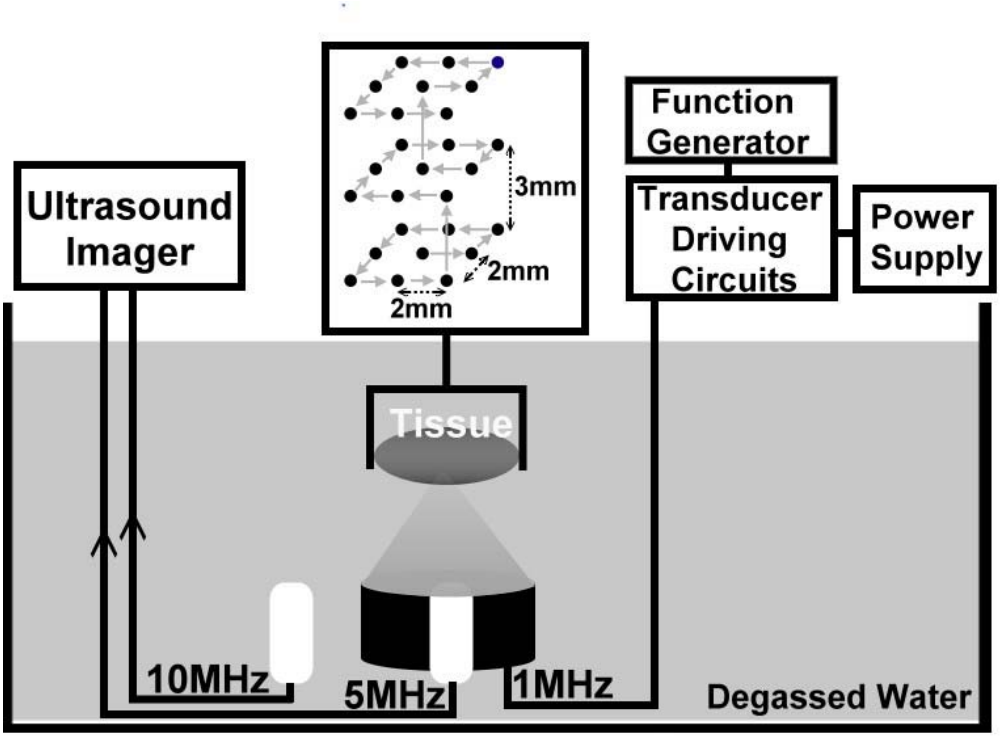

Figure IV-3: Experimental setup of histotripsy treatments *in vitro*. The tissue is mounted to a 3-D positioning system and moved to be scanned with histotripsy pulses along a 3×3×3 scanning grid. Each treatment location in this grid is exposed to 100, 300, 500, 700, 1000, 1500, or 2000 pulses in order to produce different degrees of tissue fractionation.

4.2.4 Histotripsy treatment plan

Lesions of approximately 6 mm × 6 mm × 15 mm each were generated by mechanically scanning the therapy focus in a 3 × 3 × 3 grid spaced 2 mm laterally and 3mm axially (**Figure II-1**). To produce different degrees of tissue fractionation, lesions were created with different numbers of ultrasound pulses. The number of pulses applied per treatment location, the total treatment time for each lesion, the total propagated energy and the sample size were listed in **Table IV-1**.

Table IV-1: Ultrasound treatment parameters for each treatment location or each lesion.

Each treatment location			Each lesion (volume ~0.5cm^3)		
# of pulses	Treatment time (s)	Delivered energy (J)*	Total treatment time	Total delivered energy (J)**	Sample size
0	0	0	0	0	9
100	1	0.8	27 s	20.7	6
300	3	2.3	1.4 min	62.0	6
500	5	3.8	2.3 min	103.3	6
700	7	5.4	3.2 min	144.7	6
1000	10	7.7	4.5 min	206.7	9
1500	15	11.5	6.8 min	310.0	7
2000	20	15.3	9 min	413.4	6

* The delivered energy per treatment location is calculated by $I_{SATA} \times A_{BCS} \times T$ where A_{BCS} is the -6-dB beam cross-sectional area measured in free field, and T is the treatment time per treatment location.

** The total delivered energy for each lesion is calculated by (Delivered energy to each treatment location)×(Total number of treatment locations)

4.2.5 Ultrasound backscatter intensity analysis

The ultrasound backscatter was collected from a 4 mm × 6 mm region-of-interest (ROI) from an imaging plane centered in the planned treatment volume before and immediately after the treatment. The size of the ROI was chosen to be the same as the treatment grid so that the ROI covered the majority of the lesion. This selection of ROI ensured that the signals collected for backscatter analysis were from the treated tissue and not interfered with those from the untreated tissue. To quantitatively compare backscatter change across treatments, normalized backscatter intensity was calculated as follows. The backscatter intensity of a lesion was defined as the median backscatter intensity in a ROI within the lesion. The median backscatter intensities before and after treatment were calculated for each lesion. Normalized backscatter intensity of the lesion was estimated as the ratio of the post-treatment to the pre-treatment backscatter intensity.

In 22 of 58 lesions, some small hyperechoic regions appear within the treatment volume on the post-treatment ultrasound images. These hyperechoic regions are assumed to be air bubbles generated during treatment, and they persisted for minutes after treatment. In most lesions, the area occupied by the bubbles was small and easily identified, since its echogenecity was 15 dB higher than that of the untreated tissue. The pixels in the bubble regions were excluded by manual segmentation for backscatter intensity analysis. In 3 lesions, however, the hyperechoic area occupied by the bubbles was too large. Excluding the pixels in the hyperechoic regions would affect the statistical significance for backscatter intensity analysis. These 3 lesions were therefore excluded for data analysis.

4.2.6 Degree of tissue fractionation assessment

The hematoxylin and eosin (H&E) staining was used here for histological assessment of tissue fractionation based on its separable staining of nucleic and cytoplasmic components. Treated kidneys were fixed in 10% neutral buffered formalin and processed for H&E staining. Histological sections of 5-μm thickness were made at 500-μm interval through the tissue with slices oriented in parallel with the ultrasound imaging plane. The H&E slides were examined under a bright-field optical microscope (Galen III, Leica Microsysems, Bannockburn, IL, USA). Slide images were captured with a digital microscope camera (ProgRes C10plus, JENOPTIK Laser, Optik Systeme GmbH, Jena, Germany) connected to the microscope. Five 320 μm × 240 μm regions were imaged at a 400X magnification in a treated area. Locations of these five regions were

selected to form a grid pattern with a 1-mm spacing as shown in **Figure IV-4**. As a control, five regions with the same size, magnification, and spacing were imaged in an untreated area.

The degree of tissue fractionation was quantified by the percentage of normal appearing cell nuclei remaining in the treated area in comparison to the untreated area. The number of normal appearing nuclei was counted in the five regions in the treated area indicated in **Figure IV-4** as well as in the untreated area. The five counts were then averaged to obtain a representative nuclei count. The percentage of the remaining normal appearing nuclei was calculated by dividing the average nuclei count in the treated area by that in the untreated area, as in the following equation.

$$Remaining\ normal\ appearing\ nuclei\ \% = \frac{normal\ appearing\ nuclei\ count_{treated}}{normal\ appearing\ nuclei\ count_{untreated}} \times 100\%$$

The percentage of remaining normal appearing nuclei was therefore used as an indication of the degree of tissue fractionation.

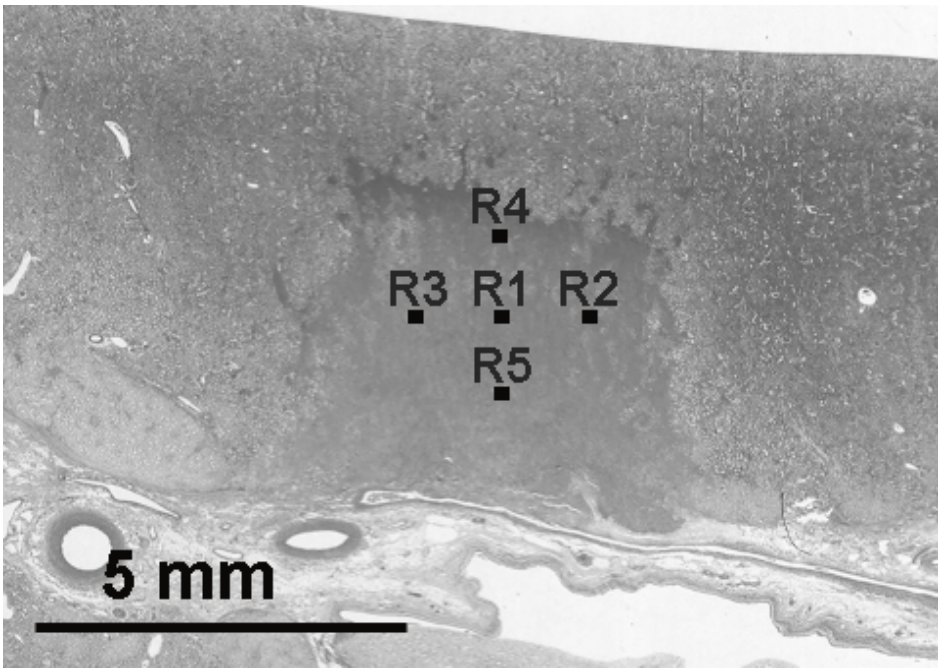

Figure IV-4: The homogeneous area in the center of the histology image indicates a lesion generated by histotripsy. Five regions (R1-R5) in the lesion were selected to examine the percentage of normal appearing cell nuclei in the treated volume. The numbers of normal appearing cell nuclei in each image were counted. The means and standard deviations of nuclei count from these five regions were calculated.

4.3 Results

A total of 58 lesions were produced in nine porcine kidneys using seven different numbers of therapeutic ultrasound pulses per treatment location as given in Table I. Results collected from 55 of 58 lesions were included for our data analysis, resulting in a sample size of 6 to 9 for each number of pulses. Data from 3 out of the 58 treatments were excluded because of a relatively large number of bubbles persisting in the lesions after treatment, interfering significantly with the backscatter analysis.

4.3.1 Ultrasound backscatter intensity analysis

Within the treated area, a localized hypoechoic zone was discernable for all the different numbers of pulses used (**Figure IV-5**). Furthermore, for all of the different pulse numbers tested, Student's T-tests performed on the treated vs. untreated areas indicated a significant ($p < 0.001$) decrease in the normalized backscatter intensity in the treated area. For example, the normalized backscatter intensity decreased to 0.7 when 100 pulses per treatment location were delivered, and 0.1 when 2000 pulses per treatment location were delivered. Correspondingly, the normalized backscatter intensity decreased with increasing number of pulses (**Figure IV-6**). Regression analysis showed that the normalized backscatter intensity decreased exponentially as the number of pulses increased (R^2=0.94).

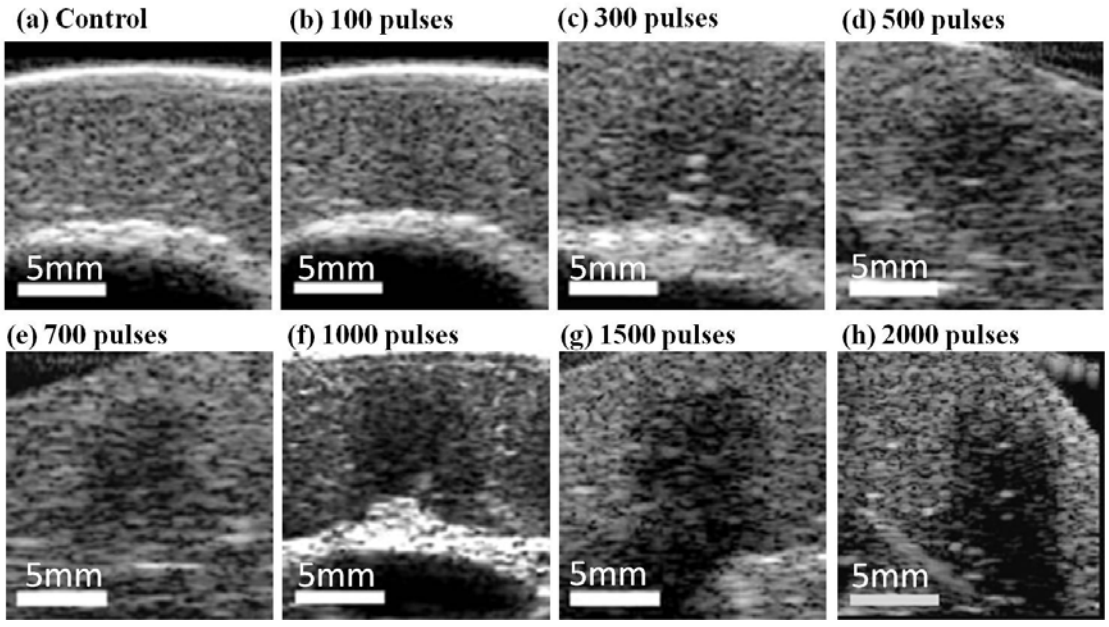

Figure IV-5: B-mode images of different lesions generated with increasing numbers of pulses: (a) control (b) 100, (c) 300, (d) 500, (e) 700, (f) 1000, (g) 1500, and (h) 2000 pulses/treatment location. A progressive decrease in backscatter intensity is observed. Images are displayed with a dynamic range of 50 dB.

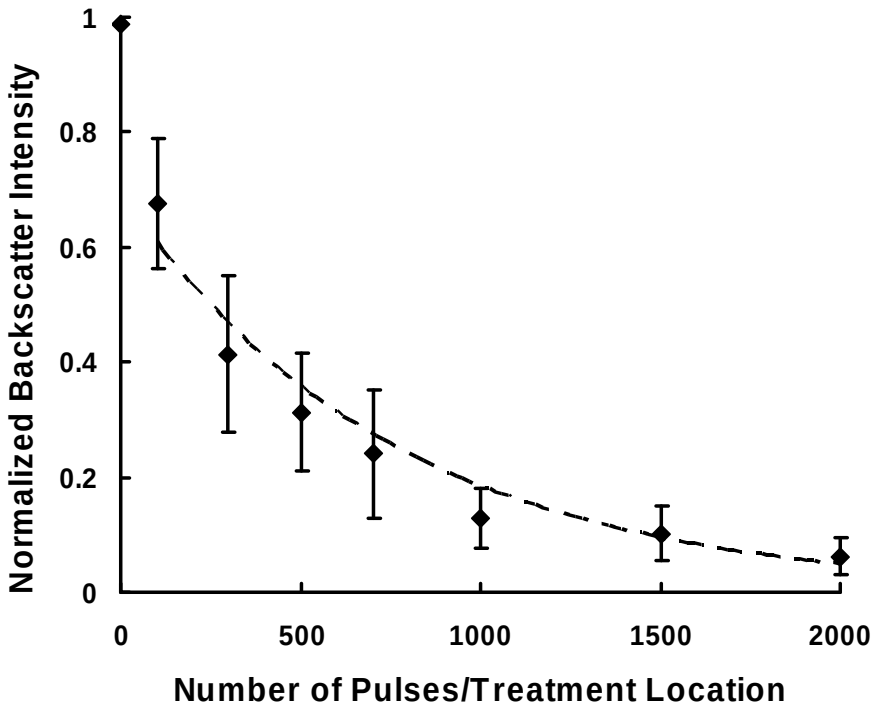

Figure IV-6: Normalized backscatter intensity as a function of number of pulses/treatment location. Data points are expressed in mean ± standard deviation (N=6~9). The normalized backscatter intensity decreases exponentially as the number of pulses increases (Dashed line: $y=0.69e^{-0.001x}$, $R^2=0.94$).

4.3.2 Degree of tissue fractionation assessment

Figure IV-7 illustrates representative H&E slide images of targeted volumes of porcine kidney tissue treated with various numbers of pulses. In an untreated area, all cell nuclei appear normal. In treated areas, cell morphology varied significantly: cells with normal appearing, pyknotic, and/or complete absence of cell nuclei were present. With the lowest number of pulses (e.g., 100-300 pulses per treatment location), subvolumes of acellular debris and disrupted cellular structures were observed in the midst of largely

unfractionated tissue within a treated area. As the number of pulses increased (e.g., 300 - 1000 pulses per treatment location), the subvolume of homogenate was enlarged, resulting in the homogenate surrounding small islands of unfractionated tissue. At the highest pulse numbers (e.g., 1500 - 2000 pulses per treatment location), the treated area was completed fractionated, with no or very few recognizable cellular structures. Immediately surrounding the lesions was a 10 - 100 μm transition zone of cells with pyknotic or absent cell nuclei. The tissue outside the transition zone appeared histologically intact.

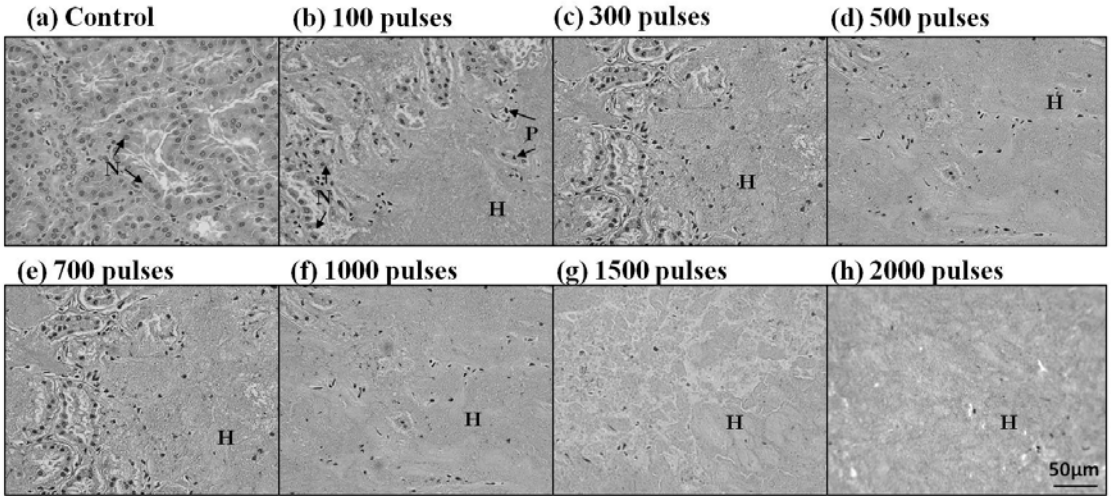

Figure IV-7: H&E stained lesions show progressive tissue fractionation generated with increasing numbers of pulses. In the control (untreated) slide, all cell nuclei appear normal. Following application of histotripsy treatment, the number of normal-appearing cell nuclei (N) decreases significantly, and pyknotic cell nuclei (P) are apparent. Subvolumes of homogenized tissue debris (H) exist in all treated tissues. Larger subvolumes of homogenate are observed as the number of pulses increases.

Quantitative tissue damage was assessed by evaluating the percentage of remaining normal appearing cell nuclei. This percentage decreased with increasing number of pulses, indicating the increasing degree of tissue fractionation (**Figure IV-8**). The remaining normal appearing nuclei decreased substantially to approximately 40% at the lowest number of pulses tested (100 pulses per treatment location) when compared to the untreated areas, and further reduced to nearly zero at 1000 pulses per treatment location and above. Regression analysis showed that this decrease in the percentage of remaining nuclei followed an exponential trend (R^2=0.97).

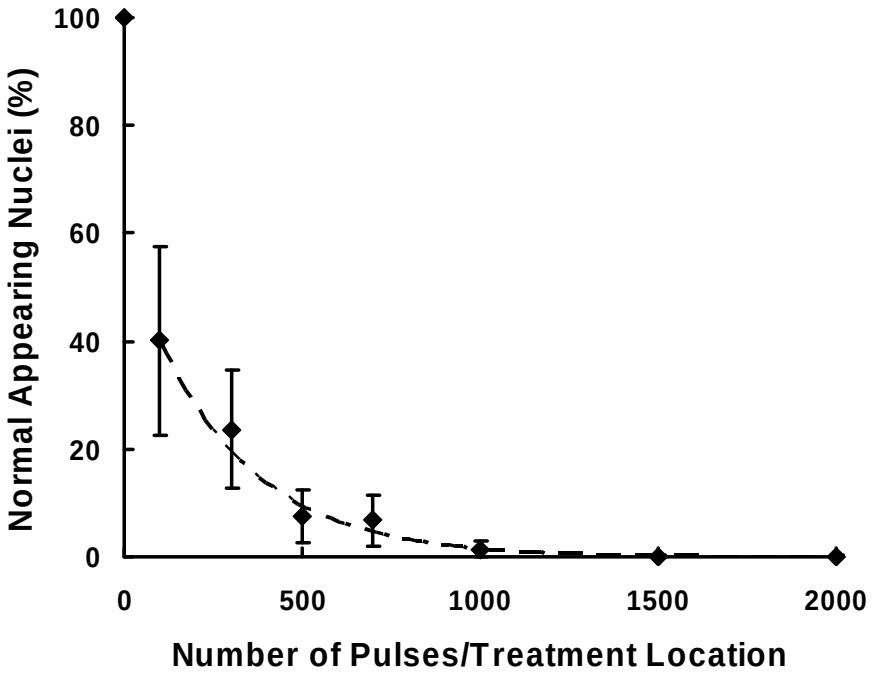

Figure IV-8: Percentages of normal appearing nuclei plotted as functions of the number of treatment pulses. Data is expressed in mean ± standard deviation (N=6~9). The percentage of normal appearing cell nuclei decreases exponentially as the number of pulses increases (Dashed line: $y=57.9e^{-0.004x}$, R^2=0.97).

4.3.3 Correlation between backscatter intensity and degree of tissue fractionation

Qualitatively, more severe histological tissue damage corresponded to lower normalized ultrasound backscatter intensity. The size and shape of the lesion on H&E slides matched those of the hypoechoic area on ultrasound images. Quantitatively, the normalized backscatter intensity was correlated to the degree of tissue fractionation, indicated by the percentage of the remaining normal appearing nuclei (**Figure IV-9**). The normalized backscatter intensity decreased significantly (from 1.0 to 0.7) at the beginning of the treatment progression when the percentage of remaining normal appearing nuclei dropped from 100% to 40%. As the percentage of normal appearing nuclei approached zero, the normalized backscatter intensity decreased to nearly 0.1. The percentage of the remaining normal appearing nuclei decayed linearly as the normalized backscatter intensity decreased. A strong correlation between the percentage of the normal appearing nuclei and the normalized backscatter intensity was found by regression analysis (R^2=0.95).

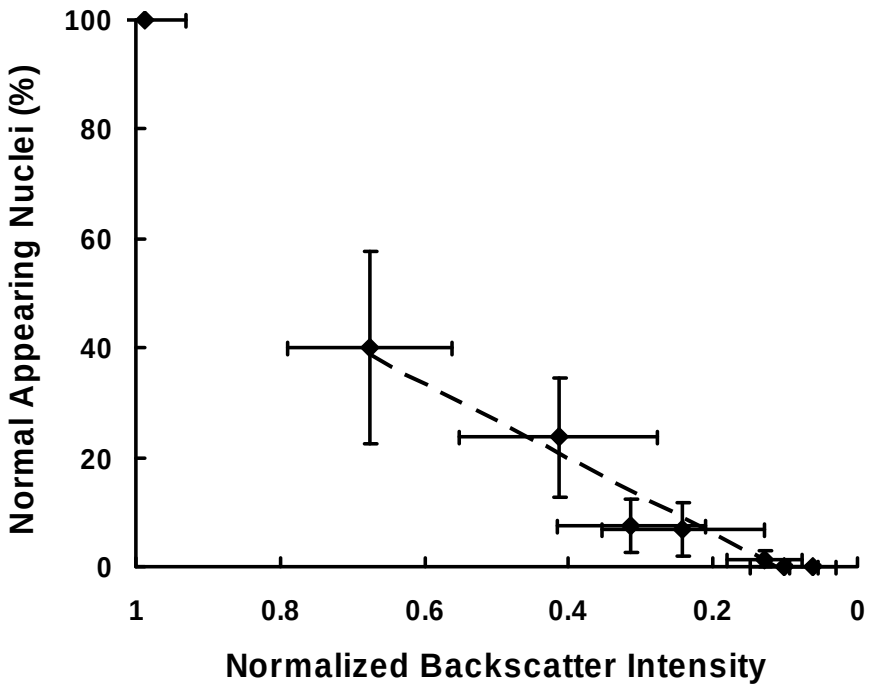

Figure IV-9: Percentages of normal appearing nuclei plotted as functions of the normalized backscatter intensity. Data is expressed in mean ± standard deviation (N=6~9). A strong linear correlation is found between the percentage of normal appearing cell nuclei and the normalized backscatter intensity (Dashed line: y=68.2x-7.5, R^2=0.95). The data point from the untreated tissue (control, normal appearing nuclei = 100%, normalized backscatter intensity =1.0) is excluded for the regression analysis.

4.4 Discussion

We have shown a strong correlation between the normalized backscatter intensity and the percentage of the remaining normal appearing nuclei, i.e., the degree of tissue fractionation. This correlation established an important link between an easily obtained image parameter and physical tissue damage. Based on the correlation, we may predict

the degree of tissue fractionation in the treated area using ultrasound imaging. The ultrasound backscatter data can be collected, not only immediately after treatment, but also during the treatment. At the very least, the therapy pulses may be temporarily stopped for real-time imaging of the treated tissue. The tissue fractionation process can be resumed when the therapy pulses are applied again. More advanced signal processing may allow tissue assessment while the therapy continues. Since the ultrasound backscatter can be collected immediately after the treatment, the backscatter reduction may be an image-based feedback parameter that would allow a clinician to determine when sufficient treatment has occurred.

A threshold value of the normalized backscatter intensity indicative of sufficient treatment may be inferred from the correlation between the percentage of remaining intact nuclei and the normalized backscatter intensity. For any treatment that requires complete tissue removal, such as tumor ablation, a zero survival rate is desired. According to the present study, a normalized backscatter intensity of 0.1 corresponds to zero normal appearing cell nuclei remaining in the target volume. Therefore, a normalized backscatter intensity below 0.1 may inform sufficient treatment. However, this value may be a threshold beyond that required for cell death because the cell death is strictly determined by the morphological change of the cell nucleus. In fact, the cells may be irreversibly damaged to the point of eventual cell death while the cell nuclei temporarily remain morphologically intact. A comprehensive evaluation on the cell or tissue damage and *in vivo* chronic studies are necessary to establish a proper threshold for sufficient treatment. While cell nuclei were used here as an indication of tissue

fractionation and a source of acoustic backscatter, we plan to investigate other cellular components (e.g., cell membrane) in the future.

Bubbles generated by histotripsy may persist for minutes after the treatment. These bubbles result in hyperechoic regions in the treated volume and are the main interference with the evaluation of backscatter intensity. However, this complication occurred in only 3 of 58 lesions produced and signal processing methods may be able to discriminate bubble signals from that of the underlying tissue structure. Further investigation into acoustic techniques for resolving this issue is currently being pursued.

The calculation of the normalized backscatter intensity relies on accurate alignment of the B-mode images before and after treatment. In the *ex vivo* setup, tissue is mounted to the positioning system, and the alignment of images before and after treatment can be achieved easily. In a clinical setting, patients may move during the treatment, which may affect the backscatter analysis. To address this issue, we can identify several reference points on the ultrasound image before the treatment. After the treatment, the imaging plane can be reproduced by moving the imaging probe to the plane defined by these reference points. Alternatively and in case of any deformation, the pre-treatment and post-treatment images could be registered by aligning the reference points on the two images using image registration algorithms [19, 20]. The backscatter intensity analysis can then be performed in the treatment area on the two registered images.

Significant ultrasound backscatter reduction is observed in a highly localized area treated by histotripsy. Ultrasound backscatter is the acoustic waves reflecting off

inhomogeneities in the propagation medium [21]. In biological tissue, the inhomogeneities result from the discontinuities in the acoustic impedance among various tissue microstructures. The literature has identified several possible sources of ultrasonic scattering, including the cell nuclei, collagen, extracellular matrix, or functional tissue elements such as the glomerulus or renal tubules [22-28]. Our histological observations of a completely fractionated tissue showed that very few, if any, of the above scattering structures persisted in the local area completely fractionated by histotripsy. Therefore, the backscatter reduction may occur because the histotripsy pulses mechanically break down the arrangement of tissue structure, resulting in a more homogeneous volume with reduced scatter cross section.

The linear relation found in the present work between the normalized backscatter intensity and the percentage of normal appearing cell nuclei is consistent with the trend predicted from the model of incoherent scattering. One possible explanation is that the cell nuclei might be an important source of sound scattering in tissue. This explanation is suggested since 1) the average size (8 μm) of the cell nucleus is much smaller than the acoustic wavelength of the imaging probe used to collect backscatter signals (150 μm), and 2) the mechanical properties of the cell nuclei are similar to those of the surrounding medium [29]. Thus, weak scattering waves are emitted from individual cell nuclei. Under such conditions, the scattered waves from the cell nuclei can be assumed to cause mostly incoherent scattering. The theoretical model predicts backscatter intensity from incoherent scattering to be linearly proportional to the concentration of scatterers [30], which may explain the linear correlation found in this study. It is worth noting that this model assumes a sparse population of scatterers. Modification is needed for a dense

medium, such as an untreated tissue that contains multiple types of sound scattering structures, because of a more complicated scattering environment and correspondingly different backscattered fields [31-34]. A different trend of backscatter intensity change may be found for untreated or less fractionated tissues. This is probably why the control data point in **Figure IV-9** deviated from the linear fit between the percentage of the cell nuclei and the normalized backscatter intensity. Despite the fact that the incoherent scattering from the cell nuclei could well explain the results, it is also likely that the cell nuclei are just a good indicator of the intact structures responsible for sound scattering.

The median backscatter intensity is used as the first metric for the evaluation of the degree of tissue fractionation. However, higher order statistics can be applied to predict more details on the structural change in tissue. For example, the ultrasound backscatter power spectrum parameters have been shown theoretically and experimentally indicative of the size, shape and concentration of the acoustic scatterers in biological tissues [32-36]. The feasibility of using these higher order statistics to predict the degree of tissue fractionation in histotripsy will be investigated in the future.

4.5 Conclusions

Histotripsy progressively and mechanically fractionates tissue using cavitation. With a sufficient number of pulses, it can completely fractionate tissue to acellular debris. Significant reduction in ultrasound backscatter intensity occurs in the treated tissue volume immediately after the treatment. Normalized ultrasound backscatter intensity is quantitatively correlated with the percentage of normal appearing cell nuclei, i.e., the

degree of tissue fractionation. As tissue fractionation should be related to the cell death or some other clinical outcomes, we believe that the normalized ultrasound backscatter intensity has the potential to be a real-time feedback parameter for histotripsy that allows the prediction of local clinical outcomes, i.e., when a tissue volume has been sufficiently treated. Such a feedback metric is highly desirable, if not essential, for any non-invasive surgical procedure.

4.6 References

[1] K. Kuroda, A. H. Chung, K. Hynynen, and F. A. Jolesz, "Calibration of water proton chemical shift with temperature for noninvasive temperature imaging during focused ultrasound surgery," J. Mag. Reson. Imaging, vol. 8, pp. 175-181, Jan-Feb 1998.

[2] P. E. Huber, J. W. Jenne, R. Rastert, I. Simiantonakis, H. P. Sinn, H. J. Strittmatter, D. von Fournier, M. F. Wannenmacher, and J. Debus, "A new noninvasive approach in breast cancer therapy using magnetic resonance imaging-guided focused ultrasound surgery," Cancer Res., vol. 61, pp. 8441-8447, Dec. 2001.

[3] J. D. Hazle, R. J. Stafford, and R. E. Price, "Magnetic resonance imaging-guided focused ultrasound thermal therapy in experimental animal models: correlation of ablation volumes with pathology in rabbit muscle and VX2 tumors," J. Mag. Reson. Imaging, vol. 15, pp. 185-194, Feb. 2002.

[4] A. Vanne and K. Hynynen, "MRI feedback temperature control for focused ultrasound surgery," Phys. Med. Biol., vol. 48, pp. 31-43, Jan. 2003.

[5] A. N. Amini, E. S. Ebbini, and T. T. Georgiou, "Noninvasive estimation of tissue temperature via high-resolution spectral analysis techniques," IEEE Trans. Biomed. Eng., vol. 52, pp. 221-228, Feb 2005.

[6] C. A. Damianou, N. T. Sanghvi, F. J. Fry, and R. Maass-Moreno, "Dependence of ultrasonic attenuation and absorption in dog soft tissues on temperature and thermal dose," J. Acoust. Soc. Amer., vol. 102, pp. 628-634, Jul. 1997.

[7] Z. Sun and H. Ying, "A multi-gate time-of-flight technique for estimation of temperature distribution in heated tissue: theory and computer simulation," Ultrasonics, vol. 37, pp. 107-122, Feb. 1999.

[8] N. L. Bush, I. Rivens, G. R. ter Haar, and J. C. Bamber, "Acoustic properties of lesions generated with an ultrasound therapy system," Ultrasound Med. Biol., vol. 19, pp. 789-801, 1993.

[9] N. R. Miller, J. C. Bamber, and G. R. ter Haar, "Imaging of temperature-induced echo strain: preliminary in vitro study to assess feasibility for guiding focused ultrasound surgery," Ultrasound Med. Biol., vol. 30, pp. 345-356, Mar. 2004.

[10] R. Righetti, "Elastographic characterization of HIFU-induced lesions in canine livers," Ultrasound Med. Biol., vol. 25, p. 1099, 1999.

[11] T. L. Hall, J. B. Fowlkes, and C. A. Cain, "A real-time measure of cavitation induced tissue disruption by ultrasound imaging backscatter reduction," IEEE Trans. Ultrason., Ferroelect., Freq. Contr., vol. 54, pp. 569-575, Mar 2007.

[12] F. Winterroth, Z. Xu, T.-Y. Wang, J. E. Wilkinson, W. W. Roberts, J. B. Fowlkes, and C. A. Cain, "Tissue Fragmentation Treatment by Pulsed Cavitational Ultrasound Therapy-Histotripsy " in Proc. IEEE Ultrason. Symp., New York, NY, USA, 2007, pp. 144-147.

[13] A. M. Lake, Z. Xu, J. E. Wilkinson, C. A. Cain, and W. W. Roberts, "Renal ablation by histotripsy--does it spare the collecting system?," J Urol, vol. 179, pp. 1150-4, Mar 2008.

[14] S. Umemura and C. A. Cain, "Acoustical evaluation of a prototype sector-vortex phased-array applicator," IEEE Trans. Ultrason., Ferroelect., Freq. Contr., vol. 39, pp. 32-38, Jan. 1992.
[15] T. Hall and C. A. Cain, "A Low Cost Compact 512 Channel Therapeutic Ultrasound System For Transcutaneous Ultrasound Surgery," in Amer. Inst. Phys. Conf. Proc., 2006, pp. 445-449.
[16] J. E. Parsons, C. A. Cain, and J. B. Fowlkes, "Cost-effective assembly of a basic fiber-optic hydrophone for measurement of high-amplitude therapeutic ultrasound fields," J. Acoust. Soc. Amer., vol. 119, pp. 1432-1440, Mar 2006.
[17] AIUM, Acoustic Output Measurement Standard for Diagnostic Ultrasound Equipment. Laurel, MD: AIUM Publications, 1998.
[18] F. A. Duck, Physical properties of tissue : a comprehensive reference book. London: Academic, 1990.
[19] C. R. Meyer, J. L. Boes, B. Kim, P. H. Bland, G. L. Lecarpentier, J. B. Fowlkes, M. A. Roubidoux, and P. L. Carson, "Semiautomatic registration of volumetric ultrasound scans," Ultrasound Med. Biol., vol. 25, pp. 339-347, Mar 1999.
[20] J. F. Krucker, G. L. LeCarpentier, J. B. Fowlkes, and P. L. Carson, "Rapid elastic image registration for 3-D ultrasound," IEEE Trans. Med. Imaging, vol. 21, pp. 1384-1394, Nov 2003.
[21] R. C. Chivers, "The scattering of ultrasound by human tissues--some theoretical models," Ultrasound Med. Biol., vol. 3, pp. 1-13, 1977.
[22] M. O'Donnell, J. W. Mimbs, and J. G. Miller, "Relationship between collagen and ultrasonic backscatter in myocardial tissue," J. Acoust. Soc. Amer., vol. 69, pp. 580-588, Feb 1981.
[23] J. W. Hunt, A. E. Worthington, A. Xuan, M. C. Kolios, G. J. Czarnota, and M. D. Sherar, "A model based upon pseudo regular spacing of cells combined with the randomisation of the nuclei can explain the significant changes in high-frequency ultrasound signals during apoptosis," Ultrasound Med. Biol., vol. 28, pp. 217-226, Feb 2002.
[24] M. C. Kolios, G. J. Czarnota, M. Lee, J. W. Hunt, and M. D. Sherar, "Ultrasonic spectral parameter characterization of apoptosis," Ultrasound Med. Biol., vol. 28, pp. 589-597, May 2002.
[25] R. E. Baddour, M. D. Sherar, J. W. Hunt, G. J. Czarnota, and M. C. Kolios, "High-frequency ultrasound scattering from microspheres and single cells," J. Acoust. Soc. Amer., vol. 117, pp. 934-943, Feb 2005.
[26] A. S. Tunis, G. J. Czarnota, A. Giles, M. D. Sherar, J. W. Hunt, and M. C. Kolios, "Monitoring structural changes in cells with high-frequency ultrasound signal statistics," Ultrasound Med. Biol., vol. 31, pp. 1041-1049, Aug 2005.
[27] C. S. Hall, M. J. Scott, G. M. Lanza, J. G. Miller, and S. A. Wickline, "The extracellular matrix is an important source of ultrasound backscatter from myocardium," J. Acoust. Soc. Amer., vol. 107, pp. 612-619, Jan. 2000.
[28] M. F. Insana, T. J. Hall, and J. L. Fishback, "Identifying acoustic scattering sources in normal renal parenchyma from the anisotropy in acoustic properties," Ultrasound Med. Biol., vol. 17, pp. 613-626, 1991.

[29] T. Kundu, J. Bereiter-Hahn, and I. Karl, "Cell property determination from the acoustic microscope generated voltage versus frequency curves," Biophysical J., vol. 78, pp. 2270-2279, May 2000.
[30] R. F. Wagner, M. F. Insana, and D. G. Brown, "Statistical properties of radio-frequency and envelope-detected signals with applications to medical ultrasound," J. Opt. Soc. Amer. A., vol. 4, pp. 910-922, May 1987.
[31] M. F. Insana, "Modeling acoustic backscatter from kidney microstructure using an anisotropic correlation function," J. Acoust. Soc. Amer., vol. 97, pp. 649-655, Jan 1995.
[32] M. F. Insana, R. F. Wagner, D. G. Brown, and T. J. Hall, "Describing small-scale structure in random media using pulse-echo ultrasound," J. Acoust. Soc. Amer., vol. 87, pp. 179-192, Jan 1990.
[33] F. L. Lizzi, M. Greenebaum, E. J. Feleppa, M. Elbaum, and D. J. Coleman, "Theoretical framework for spectrum analysis in ultrasonic tissue characterization," J. Acoust. Soc. Amer., vol. 73, pp. 1366-1373, 1983.
[34] J. Mamou, M. L. Oelze, W. D. O'Brien, Jr., and J. F. Zachary, "Identifying ultrasonic scattering sites from three-dimensional impedance maps," J. Acoust. Soc. Amer., vol. 117, pp. 413-423, Jan 2005.
[35] M. L. Oelze and W. D. O'Brien, Jr., "Method of improved scatterer size estimation and application to parametric imaging using ultrasound," J. Acoust. Soc. Amer., vol. 112, pp. 3053-3063, Dec 2002.
[36] M. L. Oelze, J. F. Zachary, and W. D. O'Brien, Jr., "Characterization of tissue microstructure using ultrasonic backscatter: theory and technique for optimization using a Gaussian form factor," J. Acoust. Soc. Amer., vol. 112, pp. 1202-1211, Sep 2002.

CHAPTER V. IMAGING FEEDBACK FOR HISTOTRIPSY WITH SHEAR WAVE ELASTOGRAPHY

5.1 Introduction

In the previous chapter, we have demonstrated that ultrasound backscatter intensity can be used to provide feedback metric for the degree of tissue fractionation. This measurement, however, is not sensitive enough to detect the tissue damage at an early stage of the treatments. More sensitive measurement can be achieved with magnetic resonance (MR) T2 weighted imaging [1]. The major drawback of MR is the high cost and the requirement of MR-compatible ultrasound therapy system to provide feedback during the treatments.

Ultrasound elastography may be a cost-effective alternative that detects the histotripsy lesions with high sensitivity [2-8]. This imaging modality measures the tissue elasticity with a spatial resolution comparable to conventional B-mode ultrasound imaging. The general approach for elastography includes: application of stress, estimation of stress-induced strain, and reconstruction of tissue elasticity from the stress-strain relations. The stress can be applied with static or sinusoidal mechanical compression directly exerted on the tissues with mechanical compressors (e.g., [2-4, 9, 10]). However, the mechanical compression limits the applicable imaging range to superficial tissues due

to the difficulty of coupling the force to deep-lying tissues. Furthermore, artifacts may arise from incomplete knowledge of the boundary conditions [11]. As such, an alternative approach has been developed to remotely apply the stress in the deep-lying tissues with acoustic radiation force [6, 12-16]. The acoustic radiation force is generated in the tissues along the propagation path of ultrasound by the momentum transfer from the acoustic wave to the medium via absorption and/or reflection of ultrasound. A short duration (~ms) of focused ultrasound can induce an impulsive 'push' in the focal region, which subsequently launches transient shear waves propagating laterally away from the focal region. Because the velocity and attenuation of the shear waves are directly related to the elasticity and viscosity of the tissues [17], the elasticity can be derived from spatial-temporal recording of the shear waves by direct inversion of the Helmhotz equation [6, 7, 18], or estimation of the local propagation velocity [19-22].

The elastography can provide higher specificity and sensitivity for disease diagnosis [10, 23, 24] due to the high elasticity contrast between diseased and normal tissues [25, 26]. The elastography has been successful in diagnosis of breast cancer [27-29], liver cirrhosis [9], renal disease [23, 30, 31], and in detection of thermal lesions which are stiffened due to protein denature [32-37]. In contrast to thermal therapy which produces stiffened tissues, the histotripsy treatments result in soft homogenized tissues in the treated volume. Such tissue transformation may be detected with high sensitivity using elastography due to the potentially high contrast between the elasticity between normal vs. treated tissues.

In this chapter, we hypothesize that the elasticity of the treated tissues would gradually decrease as the tissues are progressively fractionated with increasing numbers

of therapy pulses. We first investigated the feasibility of imaging the elasticity change using shear wave elastography, where shear waves were induced by an impulsive 'push' generated by the therapeutic array transducer and tracked with high frame rate ultrasound imaging. Next, quantitative correlation between the tissue elasticity (i.e., Young's modulus) and the degree of tissue fractionation was studied. The quantitative correlation between the lesion elasticity and the degree of tissue fractionation, if established, provides a basis for predicting the treatment outcomes with tissue elasticity.

5.2 Materials and Methods

5.2.1 Sample preparation

Experiments were performed on agar-graphite tissue mimicking phantoms and *ex vivo* kidneys. To prepare the agar-graphite tissue mimicking phantoms, agar powder (AG-SP, Lab Scientific, Livingston, NJ) was mixed in deionized water at 0.8% w/v concentration. The mixture was heated in a microwave oven until the agar completely melted in the solution. Next, the graphite powder (Extra Fine Graphite Powder, Mr. Zip, Muskegon, MI) was mixed in the agar solution at 3% w/v concentration. To ensure homogeneous distribution of graphite in the phantom, the agar-graphite solution was stirred with a magnetic stirrer (Cimarec, Thermo Scientific, Asheville, NC) until it was fully solidified. Although the phantom prepared with this protocol appears to be macroscopically homogeneous, it contains 100-200 μm graphite aggregates under microscopic examination. These aggregates can be fractionated into very fine (< 30 μm) debris after the histotripsy treatments. Morphologically, the treated volume also

transforms into paste-like homogenate which never re-solidifies to gel (a sign of mechanical rather than thermal damage).

Freshly excised porcine kidneys were obtained from a local meat processing facility. The kidneys were placed in normal saline at 4˚C with the capsule removed. All samples were used within 48 hours of harvest. Prior to experimentation, the kidneys were submerged in degassed (20 - 30% of normal saturation determined by pO_2) saline at room temperature for ~1 hour. The kidneys were then dissected across the long axis, resulting in two ~ 6 cm thick sections with ~ 6 cm × ~ 5 cm cut surface. The kidney sections were embedded in 0.8% agar gel prepared with normal saline in a polycarbonate holder.

5.2.2 Experimental setup

A 750-kHz therapeutic array transducer (Imasonic, Voray sur l'Ognon, France) was used to generate both the therapy pulses for histotripsy and the 'push' pulses for shear wave imaging. The transducer has a geometric focal length of 12 cm, with an aperture size of 15 cm and a center hole of 5.9 cm in diameter. The array consists of 9 5-mm wide concentric rings, each dissected into two half-ring elements. The amplitude and phase of the driving signal to each element can be individually controlled by a custom-built array driving system, allowing for electronic steering in the axial direction and F/# control of the transmitted ultrasound.

A 5-MHz 128-element linear array imaging probe (L7-4, Philips Healthcare, Andover, MA) connected with a research ultrasound imaging system (V1, Verasonics, Redmond, WA) was used to collect the image data. The imaging system can

simultaneously transmit imaging pulses to 128 channels and receive echo signals from 64 channels a time. The driving voltage, center frequency, duty cycle, pulse length, and delay are adjustable. The received signals are sampled with 12-bit analog-to-digital converters at a programmable rate up to 60 MHz.

The experimental apparatus is shown in **Figure V-1**. The therapeutic transducer was mounted to a manual 3-axis positioning system. The imaging probe was mounted in the experimental tank opposite to the therapeutic array. The beam axis of the therapeutic transducer was aligned to the imaging plane by the following approach. A bubble cloud was induced in the water with brief excitation of the therapeutic transducer. The therapeutic transducer was placed so that the bubble cloud appeared with highest backscatter amplitude and largest spatial extent on the ultrasound images. After the alignment, the phantom or tissue was mounted to a motorized 3-axis positioning system and submerged in the tank approximately at the geometric focus of the therapeutic transducer. For the tissue experiments, the kidneys were placed with the long axis parallel to the ultrasound beam axis. This orientation allows the target volume to be imaged and treated in the cortex area without interference from the collecting system.

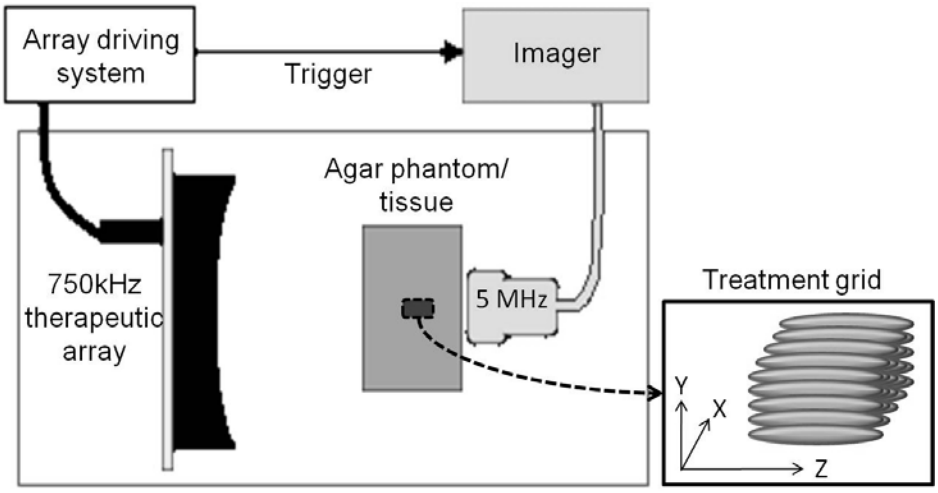

Figure V-1: Experimental setup. The 5 MHz linear array imaging probe and the 750 kHz therapeutic array transducer were mounted on opposite sides of the agar phantoms/tissues in a tank of degassed water (25 - 35% of normal saturation determined by pO_2). The imager was synchronized with the therapeutic array driving system. Lesions were produced by mechanically scanning the therapy focus in a 5×5 grid with 1 mm spacing.

5.2.3 Histotripsy treatments

Histotripsy therapy pulses of 3 cycles in duration were delivered at 50 Hz pulse repetition frequency (PRF) by the therapeutic array transducer. All elements on the array were driven in-phase with equal amplitude, resulting in an F/# 0.8 focal configuration. The pressure field was calibrated with a custom-built fiber optic probe hydrophone (FOPH) with an active element of 100 μm in diameter [38]. The peak negative (P−) and peak positive (P+) pressures were measured −17 and 108 MPa, respectively (**Figure V-2**). Due to attenuation of ultrasound in the agar-graphite phantoms (0.1 dB/cm/MHz [39]) and in the kidneys (1 dB/cm/MHz [40]), the P− pressures at the treatment location were likely ~16.5 MPa in the phantoms, and ~13 MPa in the kidneys. The P+ pressures were

likely decayed more significantly due to nonlinear absorption. The −6-db beamwidths were measured at a reduced P−/P+ pressure of −11/58 MPa. The lateral/axial −6-db beamwidth were 2.6/17.8 mm on the P− pressure profile, and 1.2/7.3 mm on the P+ pressure profile. The beamwidths at higher pressures could not be successfully measured because the cavitation easily occurred and damaged the fiber tip during the pressure profile scan.

Lesions of approximately 7 mm × 7 mm × 14 mm were produced by mechanically scanning the therapy focus in a 5 × 5 grid with 1 mm spacing on the focal plane (**Figure V-1**). To produce different degrees of tissue fractionation, lesions were produced with treatment doses of 0, 100, 200, 300, 500, 1000, 1500, and 2000 therapy pulses per treatment location on the grid. A total of 72 treatments, 9 for each dose, were performed on the agar-graphite tissue phantoms. A total of 64 treatments, 8 for each dose, were performed on the *ex vivo* kidneys. After the treatments, the samples were moved 15 mm laterally so that the elasticity imaging was conducted with the shear waves excited from outside and propagating across the lesions.

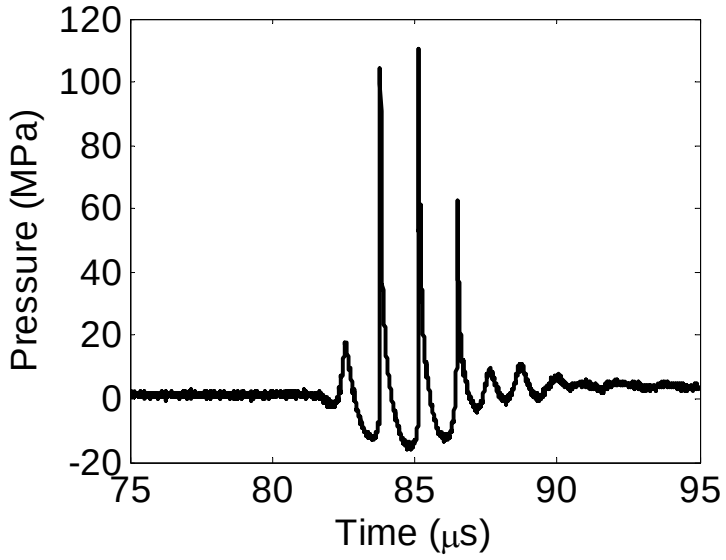

Figure V-2: Pressure waveform of the 3-cycle 750-kHz therapy pulse measured in the free field. The P−/P+ pressure was 17/108 MPa.

5.2.4 Shear wave elasticity imaging

The shear wave elasticity imaging approach used in this study is similar to those described in the literature [13, 29]. To generate a quasi-planar shear wave, three ultrasound 'pushing' beams were sequentially fired by the therapeutic array transducer focused at z = +5, 0, and −5 mm with respect to the geometric focus (i.e., z = 120mm). A 2-μs delay was inserted between push beams to allow the array driving system to update the new focal location. For each pushing beams, the outer 5 rings were shut off, resulting in a F/#-1.2 focal configuration. The pulse parameters and the measured pressure fields of the three beams were summarized in **Table V-1**.

Table V-1: Pulse parameters for acoustic radiation force generation under free field conditions.

		Push beam 1	Push beam 2	Push beam 3
Focal location		z = 125 mm	z = 120 mm	z = 115 mm
−6 db beamwidths on P− pressure profile (lateral/axial)		3.4 / 34.7 mm	3.6 / 31.5 mm	3.1 / 29.7 mm
−6 db beamwidths on P+ pressure profile (lateral/axial)		1.8 / 23.0 mm	1.6 / 20.0 mm	1.6 / 17.8 mm
P−/P+ Pressure*	phantom experiments	-5 / 14 MPa	-5 / 15 MPa	-5 / 16 MPa
	ex vivo tissue experiments	-6 / 30 MPa	-6 / 34 MPa	-7 / 36 MPa
Pulse duration	phantom experiments	133 μs	133 μs	133 μs
	ex vivo tissue experiments	200 μs	200 μs	200 μs
I_{SPPA}**	phantom experiments	1.3 kW/cm^2	1.5 kW/cm^2	1.6 kW/cm^2
	ex vivo tissue experiments	2.3 kW/cm^2	2.5 kW/cm^2	2.8 kW/cm^2

* The pressures at the treatment locations were expected lower than these measurements due to sound attenuation. Given a mean propagation distance of 3 cm, and attenuation coefficients of 0.1 dB/cm/MHz in the agar-graphite phantoms [39], and 1 dB/cm/MHz in the kidneys [40], the P− pressures were estimated ~5 MPa both in the phantom and the *ex vivo* experiments.

** I_{SPPA}: Spatial peak pulse average intensity.

To track the propagation of the shear waves at a high frame rate, ultrasound plane wave imaging [7] was performed. The imaging system generated a plane wave to illuminate the entire imaging field by simultaneously transmitting the imaging pulse from all elements on the imaging probe. The system then started recording the backscatter signals immediately after the plane wave was transmitted. As the system can only receives signals from 64 channels a time, 2 successive transmit-receive cycles, each lasting for 77 μs, were conducted to collect the backscatter signals from the 38 mm × 38

mm field of view. A total of 73 frames were captured: one reference frame acquired 1 ms before the pushing beams, and 72 frames acquired at a rate of 3000 frames per second from 1 ms after the pushing beams (**Figure V-3**). The total imaging duration lasted for 24 ms.

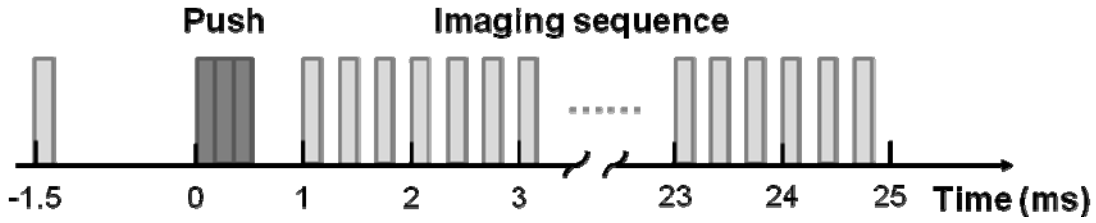

Figure V-3: Timeline of the shear wave imaging. The 'push' was induced by acoustic radiation force from 3 sequentially fired focused beams delivered by the therapeutic transducer. A total of 73 images, 1 reference image before and 72 frames after the push, were acquired. Each frame was acquired with 2 transmit-receive cycles, each lasting for 77 µs. Successive frames were acquired at 3000 fps, resulting in a total imaging duration of 24 ms.

The channel data were collected and processed off-line. Conventional delay-and-sum beamforming with a F/# 1.5 dynamic receive focusing was applied to produce the beamformed radio-frequency (RF) images. The 1-D correlation based speckle tracking algorithm [41] was then applied on the beamformed RF data to estimate the local tissue displacement. The RF data were segmented into 1.5 mm regions with 75% overlap along the axial direction. The cross correlation function of the RF segments from consecutive frames was calculated. The position of the maximum of the cross correlation function was obtained by locating the phase zero crossing around the maximum magnitude of the function. This position determined the tissue displacement between the consecutive frames.

The above processing produced a series of spatial-temporal displacement images (e.g., **Figure V-4** and **Figure V-7**). which allows the estimation of the shear wave propagation velocity in each local area, (x, z), with a time-of-flight algorithm [19, 29]. For each location (x, z), the temporal displacement profiles at two points across the location, $u(x-\Delta x, z, t)$ and $u(x+\Delta x, z, t)$, were extracted from the spatial-temporal displacement images. The propagation time, Δt, between the two points was obtained from the location of the maximum of the cross correlation function of the two displacement profiles, $u(x-\Delta x, z, t)$ and $u(x+\Delta x, z, t)$. The propagation velocity was calculated as $v_s = 2 \cdot \Delta x / \Delta t$. To improve to quality of measurement, an average propagation velocity was calculated from multiple estimates with different spacing, Δx. In this study, the average velocity was calculated from 3 pairs of points with Δx = 0.6 – 0.9 mm. This set the resolution of the final elasticity map to be approximately 1.8 mm. Finally, the Young's modulus was calculated by

$$E = 3\,\mu = 3\,\rho\,v_s^2$$

where E is the Young's modulus, μ is shear modulus, and ρ is the density of the medium (assumed 1000 kg/m^3 for the phantoms and the tissues).

The imaging process was repeated 3 times for the lesions created in the agar-graphite phantoms, and 9 times for those created in the kidneys. An average was obtained from the repeated measurements. A median Young's modulus was calculated for each lesion in an 8 × 6 mm region approximately in the center of the lesions.

To validate the elasticity measured with ultrasound imaging, the elasticity of the untreated samples was also measured with a custom-built elastometer [42]. The phantoms

or the kidney cortex were cut into 1 cm cubes and placed on an electronic balance. An aluminum rod with 8-mm diameter flat end was brought in contact with the samples. The rod was pressed into the samples step by step with a known step size. The scale reading was recorded to estimate the applied force for each step. A linear fit was applied to the stress-strain curves in the low strain (<10%) regime. The slope of the linear fit was determined as the Young's modulus of the samples.

5.2.5 Histological examination

After the treatments and the elasticity imaging, the tissues were fixed in 10% neutral buffered formalin and prepared for hematoxylin & eosin (H&E) staining. Histological sections of 4 μm thickness were made at 500 μm intervals through the lesion center with slices oriented in parallel with the ultrasound imaging plane. The sections were examined with a bright field microscope at a 400× magnification.

To evaluate the degree of tissue fractionation, the percentage of structurally intact cell nuclei remaining in the treated area was calculated. The cell nuclei were selected because they are a common indicator of cell or tissue damage. Moreover, they appeared more resistant to histotripsy damage than other cellular components, thus serving as a good indication of histotripsy damage [43, 44]. The calculation follows the process described in our previous publication [43]. In brief, images of five 320 μm × 240 μm regions in the lesion area were captured. The locations of the five regions form a cross pattern with 1.5 mm span in 4 directions and centered approximately at the lesion center. The numbers of structurally intact cell nuclei were counted for the five images. An

average of the five counts was obtained and normalized to the average count from an untreated area (control), producing a percentage of remaining structurally intact cell nuclei. This percentage may represent the degree of tissue fractionation caused by histotripsy.

5.3 Results

5.3.1 Experiments on agar-graphite phantoms

Figure V-4 shows the temporal displacement field induced in the phantoms by the shear waves. Displacement of several tens of μm was detected in the push location after the pushing beams were delivered. The shear waves were launched from the push location and propagated outward in the lateral direction. The shear waves appeared to have quasi-planar wavefronts as they propagated across an untreated area (control, **Figure V-4a**). The shear waves appeared to propagate at a lower velocity in a treated area, leading to a curved wavefront (e.g., **Figure V-4b** and **c**). The propagation velocity decreased as the treatment doses increased. At doses higher than 1000 pulses/location, the propagation was so slow that the shear waves could not propagate across the treated area within the 24-ms observation period.

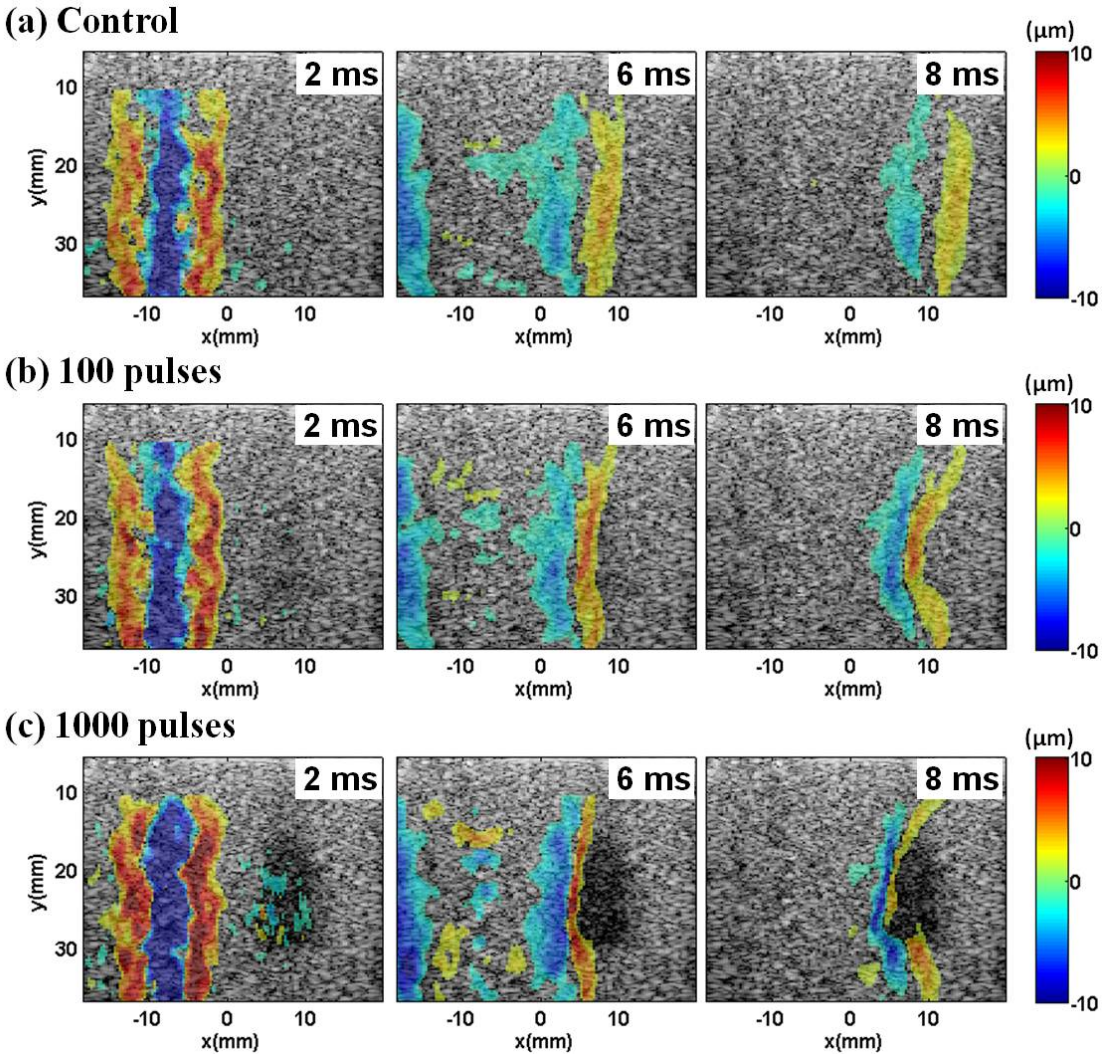

Figure V-4: Displacement images acquired at different times after the shear wave generation in the phantoms. The positive and negative displacements indicate directions of motions toward and away from the imaging probe, respectively. The shear waves were generated in the left part of the field of view, centered at around *x* = −8 mm, and propagated away from the 'push' center in opposite directions. The shear waves were significantly slowed down as they propagated across the lesions, resulting in curved wavefronts as shown in panels (b) and (c). The curvature increased with increasing treatment doses. At doses higher than 1000 pulse/location, the shear waves almost appeared to stop propagating in the lesion area, and did not propagate across the entire lesion within the 24-ms observation period.

The B-mode and the elasticity images of a representative lesion treated with increasing doses were shown in **Figure V-5**. As treatment dose increased, the treated area became increasingly hypoechoice on the B-mode images. Correspondingly, significant decrease in the Young's modulus was observed, indicating a softer area produced by histotripsy. The treated area was more easily identified on the elasticity images compared to the B-mode images, particularly at low doses (e.g., 100 pulses per treatment location). The elasticity in the majority of the treated area was successfully measured except for some regions in the far end opposite to the location of shear wave generation. Unsuccessful or noisy measurements were obtained in these regions especially when high treatment doses were applied. This is likely because the shear waves were unable to propagate across a sufficiently fractionated volume.

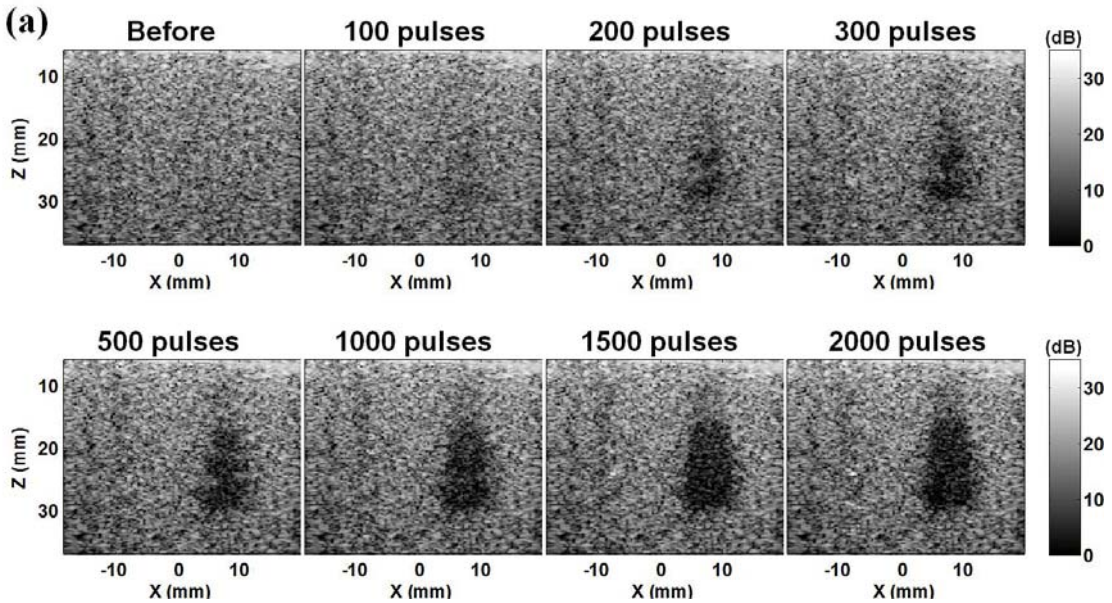

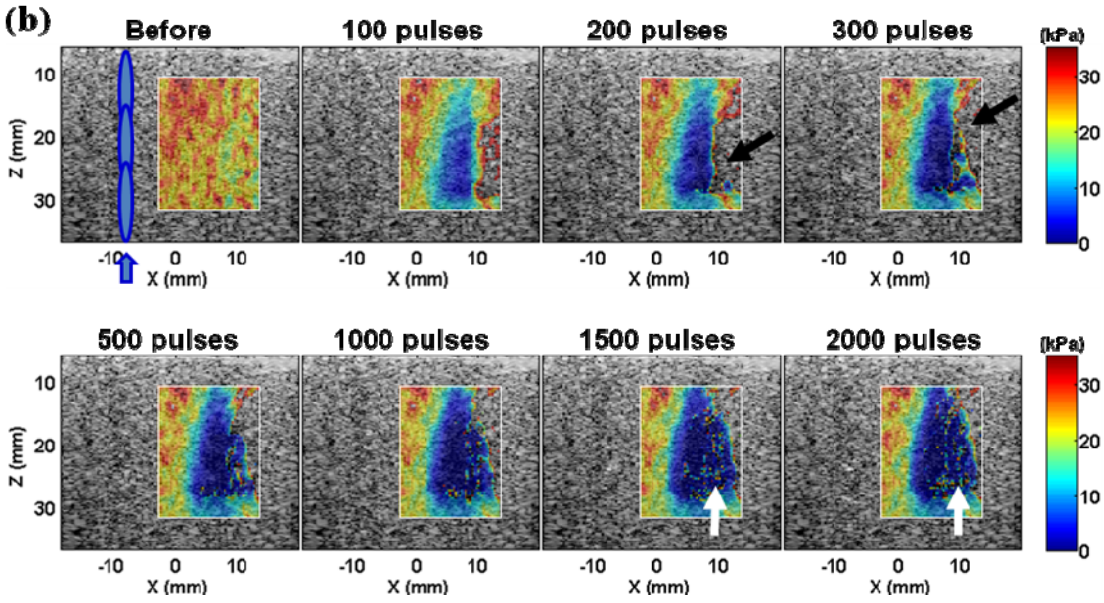

Figure V-5: (a) B-mode and (b) elasticity images of a representative lesion produced in the agar-graphite phantoms with increasing numbers of pulses per treatment location. The treated volume became increasingly hypoechoice with increasing numbers of therapy pulses. Correspondingly, the Young's modulus decreased in the treated volume. The elasticity images presented higher contrast when the treatment dose was low (e.g., 100 pulses). The elasticity in some areas by the lesion and opposite to the push location (e.g., the areas indicated by black arrows) could not be measured. Noticeable noise was also present in the far end of the lesion (e.g., the areas indicated with the white arrows). These likely occurred because the shear waves were unable to propagate across the significantly fractionated volume.

The elasticity, or the Young's modulus, of the treated area decreased exponentially with increasing treatment doses (R^2 = 0.99, **Figure V-6**). This decrease leveled off when the treatment dose was higher than 500 pulses per treatment location. The Young's modulus of the untreated agarose phantoms measured with shear wave elastography was comparable with that measured with the elastometer, i.e., 26.6 ± 2.6 kPa (N = 7).

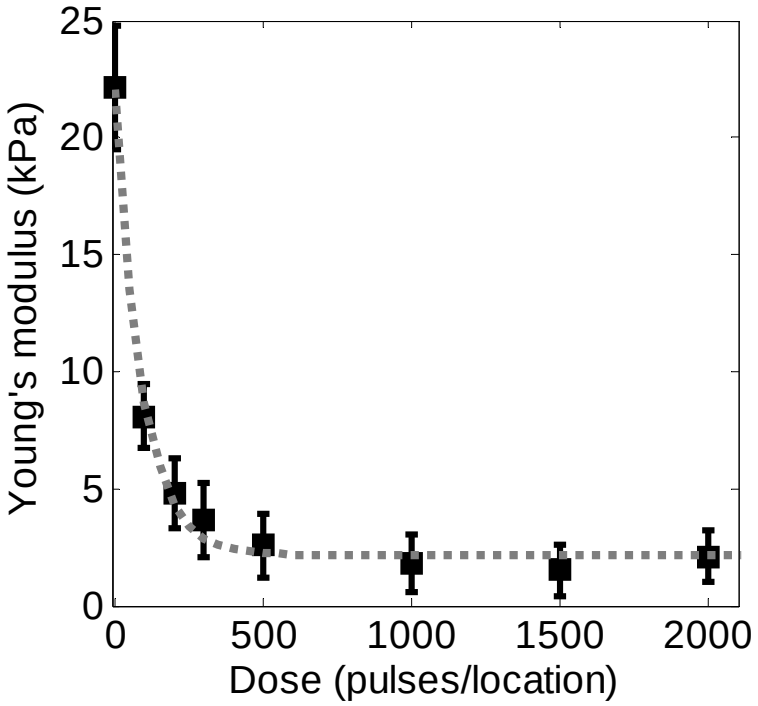

Figure V-6: The Young's modulus of the lesions produced in the phantoms decreased exponentially with increasing treatment doses. Each data point represents the mean ± standard deviation from 9 independent treatments. The dashed line represents the exponential fit with the dose centered at zero mean and scaled to unit standard deviation, i.e., $y = 0.01 \cdot e^{-8.1 \cdot ((x - 700) / 729)} + 2.18$, $R^2 = 0.99$.

5.3.2 *Experiments on ex vivo kidneys*

Figure V-7 shows the temporal displacement field induced in the tissues by the shear waves. Similar to the phenomena observed in the phantom study (**Figure V-4**), shear waves were launched from the push location and propagated laterally. The shear waves slowed down in the treated area, and could not propagate across the lesion when the lesion was created with higher doses (>1000 pulses/location). Comparing the waveforms in the phantoms (**Figure V-4**), the shear waves in the tissues appeared to spread wider and attenuate faster as they propagate across the medium (**Figure V-7**). It is

worth noting that cavitation could have been induced at the push location by the pushing beams, e.g., the bright spots indicated by the arrows in **Figure V-7.**

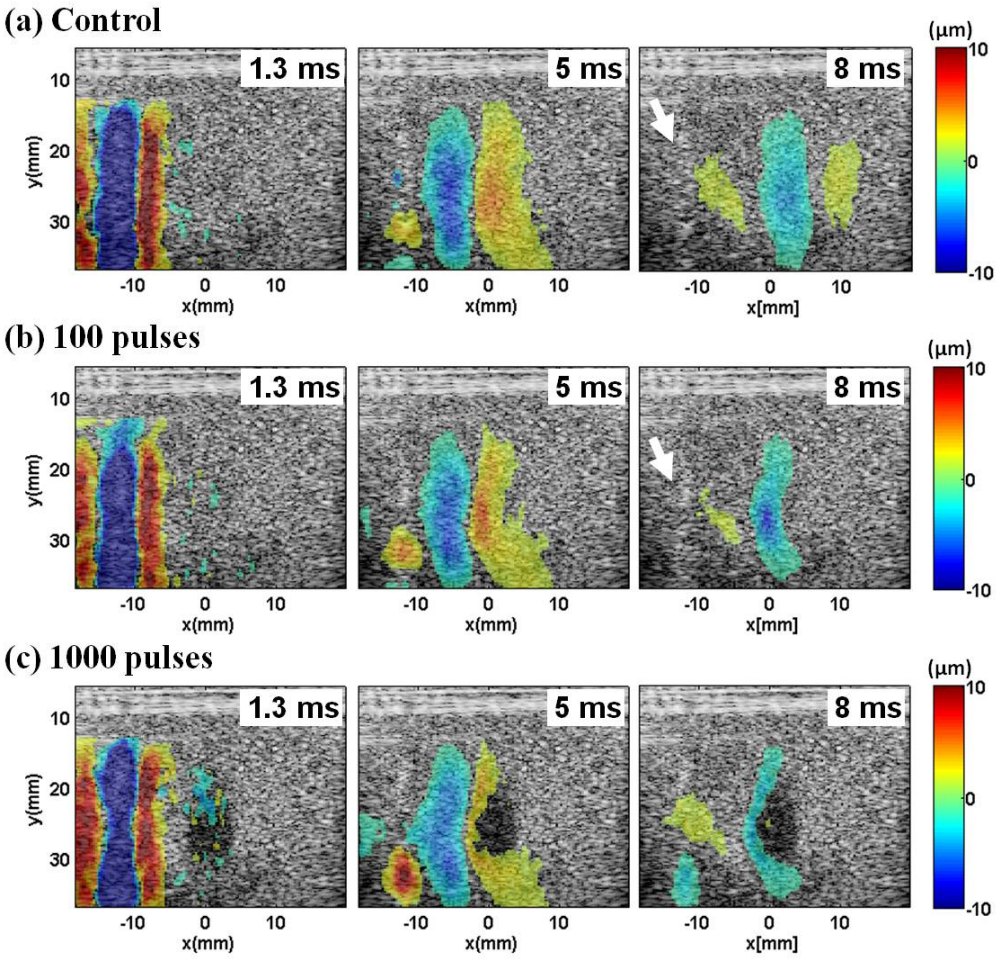

Figure V-7: Displacement images acquired at different times after the shear wave generation in the *ex vivo* kidneys. The positive and negative displacements indicate directions of motions toward and away from the imaging probe, respectively. Compared to the shear waves generated in the phantoms, the shear waves generated in the kidneys appeared more dispersive and attenuated faster. The shear waves slowed down in the lesion area, resulting in curved wavefronts as shown in panels (b) and (c). The curvature increased with increasing treatment doses. At doses higher than 1000 pulse/location, the shear waves could not propagate across the entire lesion within the 24-ms observation period. Bright spots, likely cavitation bubbles, were observed in the push location after the pushing beams were delivered (examples indicated by the white arrows).

The B-mode and the elasticity images of a representative lesion treated with increasing numbers of pulses were shown in **Figure V-8**. The treated volume was identified as an increasing hypoechoic area on the B-mode images, and a softer area with decreased Young's modulus on the elasticity images. The treated area was more easily identified on the elasticity images than on the B-mode images at low doses (e.g., < 500 pulses per treatment location). Unsuccessful or noisy measurements were obtained in the far end of the lesion opposite to the location of shear wave generation because the shear waves could not propagate well across the fractionated volume. Despite of these interferences, the lesions depicted on the B-mode and elasticity images corresponded well with their morphological appearance (**Figure V-9**).

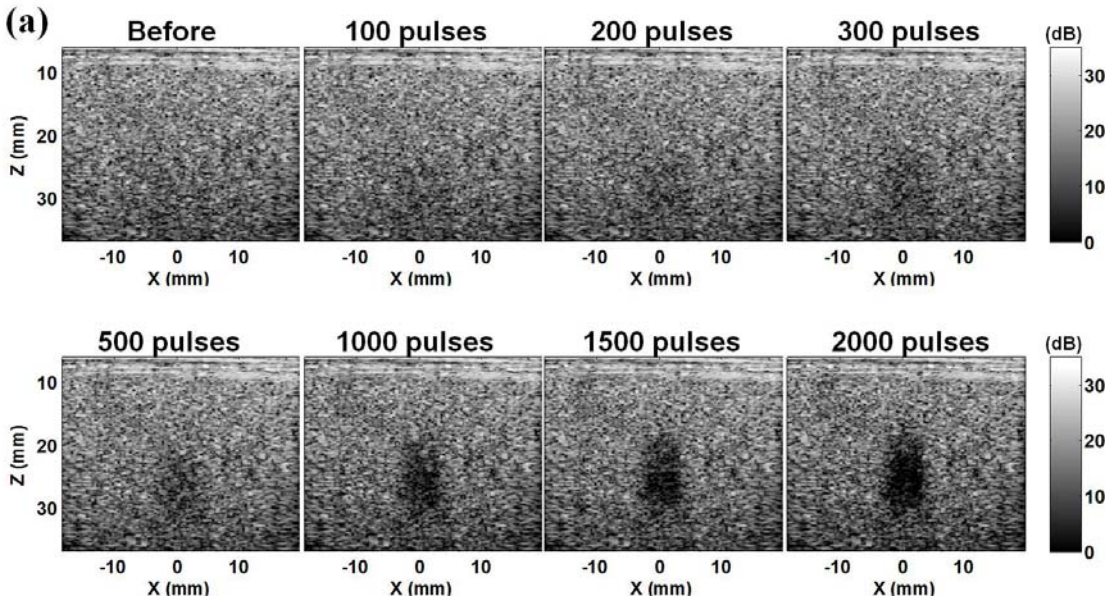

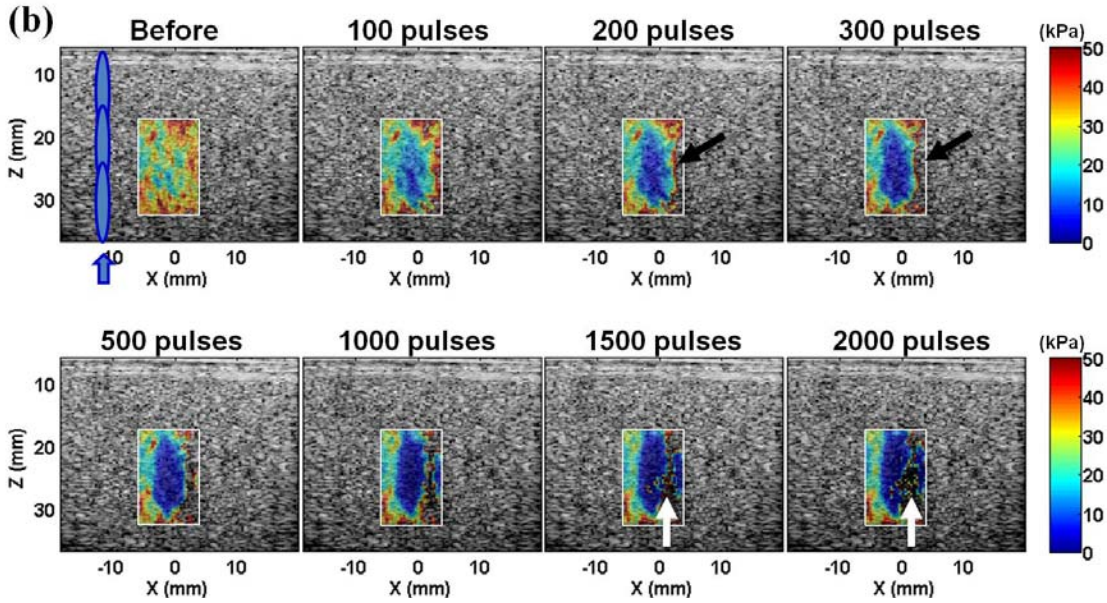

Figure V-8: (a) B-mode and (b) elasticity images of a representative lesion produced in the *ex vivo* kidneys with increasing numbers of pulses per treatment location. Both the backscatter and the Young's modulus decreased with increasing numbers of pulses. The lesions were more easily detected on the elasticity images at low doses (< 500 pulses). The elasticity in some areas opposite to the push location (e.g., the areas indicated by black arrows) could not be measured. Noticeable noise was present in the far end of the lesion (e.g., the areas indicated with the white arrows). These likely occurred because the shear waves were unable to propagate across the significantly fractionated volume.

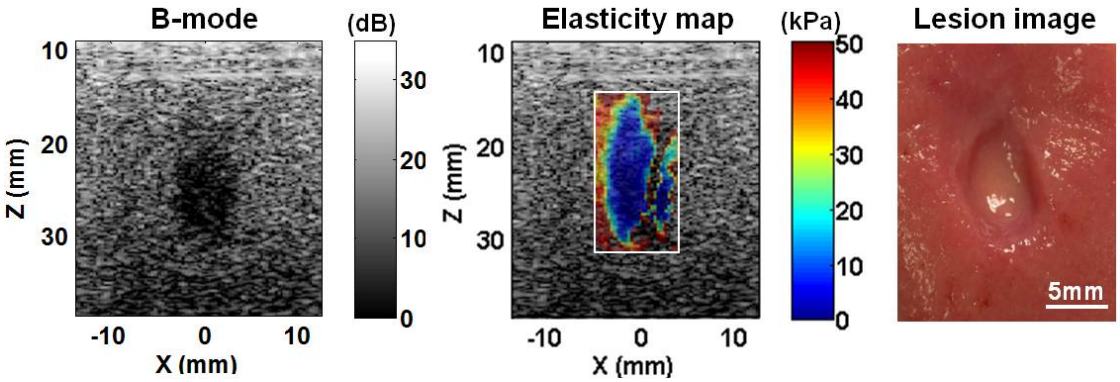

Figure V-9: The B-mode image, elasticity map, and gross morphology of a representataive lesion produced in the kidneys. The size and shape of the lesion depicted on the B-mode and elasticity images corresponded well with those observed from the morphological appearance.

The Young's modulus of the treated area decreased exponentially with increasing treatment doses (R^2 = 0.99, **Figure V-10**). This decrease leveled off when the treatment dose was higher than 1000 pulses per treatment location. The Young's modulus of the untreated kidney cortex measured with shear wave elastography was comparable with that measured with the elastometer, i.e., 30.2 ± 4.5 kPa (N=8).

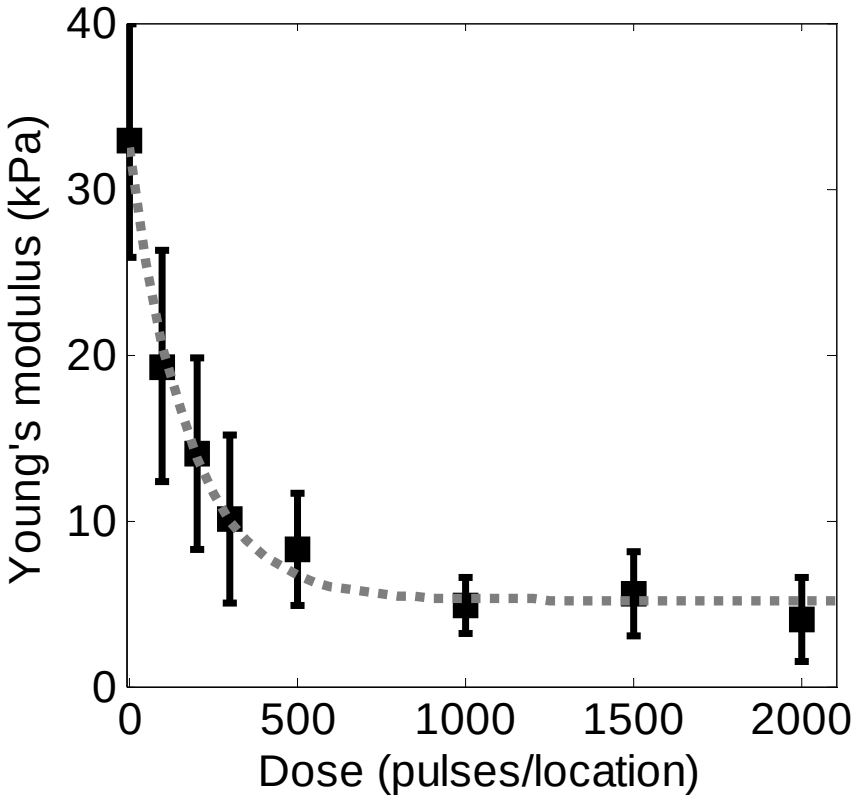

Figure V-10: The Young's modulus of the lesions produced in the *ex vivo* kidneys decreased exponentially with increasing treatment doses. Each data point represents the mean ± standard deviation from 8 independent treatments. The dashed line represents the exponential fit with the dose centered at zero mean and scaled to unit standard deviation, i.e., $y = 0.47 \cdot e^{-4.23 \cdot ((x - 700) / 729)} + 5.20$, $R^2 = 0.99$.

5.3.3 Histological examinations

Representative histological sections of the lesions produced with increasing numbers of pulses are shown in **Figure V-11**. In the control, all tissues structures and cell nuclei appeared structurally intact. In the treated area, damage to both the tissue structures and the cellular components were observed. Increasingly more damage was observed with increasing numbers of therapy pulses. At low doses, a small part of the tissues were damaged while most part remained structurally intact. Some damaged (pyknotic or fragmented) cell nuclei were observed. As the numbers of pulses increased, a larger part of the tissues were damaged and more damaged cell nuclei were found. With a dose higher than 1000 pulses per treatment location, the treated volume appeared to be completely homogenized with no recognizable tissue structures and very few fragments of nuclear material, if present.

The degree of tissue fractionation as examined with the percentage of remaining intact cell nuclei is plotted against the treatment doses in **Figure V-12**. The percentage of remaining intact nuclei decreased exponentially with increasing numbers of therapy pulses ($R^2 = 0.99$). This percentage was further correlated to the Young's modulus of the treated tissues (**Figure V-13**).). A linear correlation was found between the percentage of remaining intact nuclei and the lesion Young's modulus ($R^2 = 0.91$).

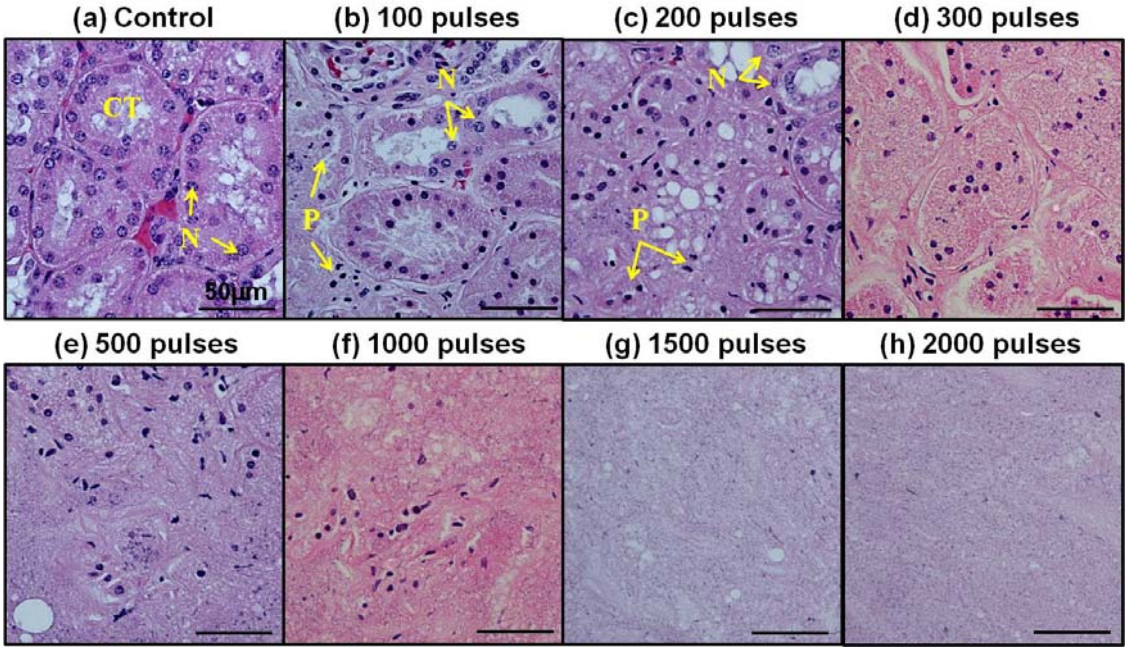

Figure V-11: Histological sections of the lesions stained with H&E. In the control, the tissues structures (e.g., convoluted tubules (CT)) appeared structurally intact. Normal appearing cell nuclei (NN) were observed in all regions. In the treated area, damage to the tissue structures and cellular components were observed. The degrees of damage increased with increasing therapy doses. At low doses, a small part of the tissues were damaged (e.g., the left part in panel (b)) while most part remained structurally intact. Some damaged (pyknotic or fragmented) cell nuclei (DN) were observed. As the numbers of pulses increased, more damage occurred to both the tissue structures and the cell nuclei. With a dose higher than 1000 pulses per treatment location, the treated volume appeared to be completely homogenized with no recognizable tissue structures and very few nuclei fragments, if present.

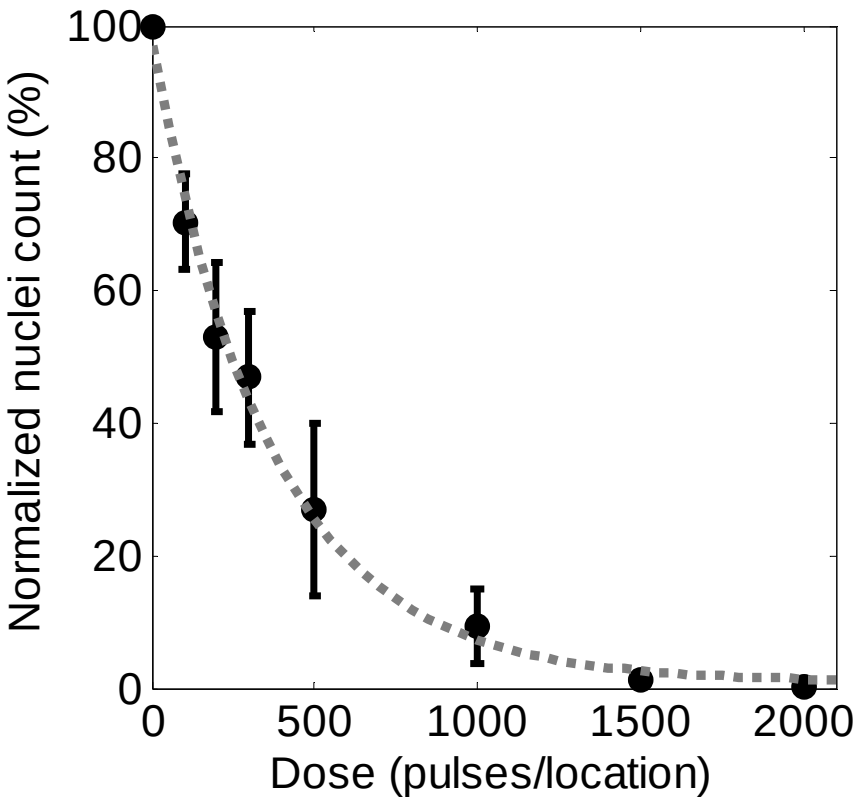

Figure V-12: Percentage of structurally intact cell nuclei remaining in the treated area. Each data point represents the mean ± standard deviation from 8 independent treatments. The dashed line represents the exponential fit with the dose centered at zero mean and scaled to unit standard deviation, i.e., $y = 0.14 \cdot e^{-1.98 \cdot ((x - 700) / 729)} + 0.01$, $R^2 = 0.99$.

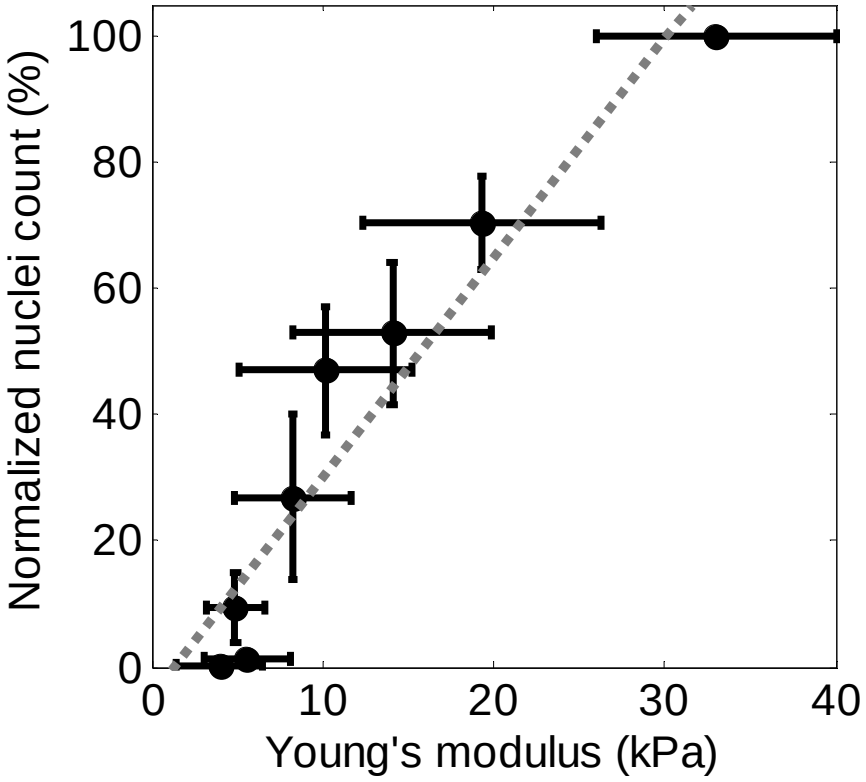

Figure V-13: Correlation between the percentage of remaining structurally intact cell nuclei and the Young's modulus. Each data point represents the mean ± standard deviation from 8 independent treatments. The dashed line represents the linear fit, $y = 0.03 \cdot x - 0.05$, $R^2 = 0.91$.

5.4 Discussion

The elastography appears to be a more sensitive measurement for detecting tissue fractionation in the early stage of the treatments compared to another imaging feedback metric, backscatter reduction [43, 45]. This is evidenced by the better contrast of the lesion in the elasticity images than in the B-mode images, especially when the lesion was created with low therapy doses. For example, the lesions produced with 100 pulses per

treatment location are more easily identified in the elasticity images than in the B-mode images, both in the phantom study (**Figure V-5**) and in *ex vivo* tissue study (**Figure V-8**). The capability of detecting tissue fractionation at the beginning of the treatment is critical for precise targeting, analysis, and optimization of the treatments.

In addition to higher sensitivity, the elastography can compensate for the discrepancy of feedback with backscatter reduction *in vivo*. Our experience in the *in vivo* studies has shown that the backscatter reduction is apparent during and within several minutes after the treatments. The backscatter intensity may increase again several minutes later, possibly because the blood coagulated in the treated volume. In this situation, the lesions may still be detectable with elastography since the newly formed blood clot is likely very soft (Young's modulus ~2 kPa [46]) compared to normal tissues.

A good correlation was found in the present work between the tissue elasticity and the degree of tissue fractionation as indicated by the damage to the cell nuclei. The change in the tissue elasticity, however, could be more directly related to the damage to the connective structures in the tissue (e.g., the extracellular matrix) responsible for tissue elasticity. It is possible that a stronger correlation may be found between the tissue elasticity and the degree of damage to these structures. In spite of such possibility, the correlation found in the present work remains an important result which has significant clinical implications. The correlation suggests that the tissue elasticity can be a very useful indicator for predicting the treatment outcomes produced by histotripsy because the injury to the cell nuclei are highly relevant to tissue damage and many other clinical situations.

The Young's moduli measured with shear wave elastography corresponded well with those measured with the elastomer. These measurements are also comparable to several results reported in the literature. For instance, the Young's modulus of the tissue phantoms measured in this study is comparable to that reported in [47] (20 – 30 kPa). The Young's modulus of the *ex vivo* kidney cortex is comparable to results from [48-50] (20 - 40 kPa), although higher than results from [51, 52] (7 - 15 kPa). The higher elasticity obtained in the present work likely occurs for a similar reason discussed by other researchers [29]. The present work estimated the elasticity based on the group velocity of the shear waves induced by an impulse excitation. The waves contain a wide band of frequencies (center frequency = 130 - 220 Hz, -15 dB frequency band = 30 - 500 Hz). In a non-dispersive medium, each frequency should travel at the same velocity as the group velocity. In the tissues, however, the strong dispersion causes higher frequencies to travel at higher velocities. Therefore, the elasticity estimated from the group velocity could be higher than that estimated from the velocity of shear waves induced by a single lower frequency, (e.g., 90 Hz in [52]).

The mechanism of acoustic radiation force generation in the current work may be very different from that in most elastography setups for diagnostic purposes (e.g., [6, 13, 29, 53]). The acoustic radiation force could be generated via absorption and/or reflection of ultrasound in the tissues. In the setup for diagnostic purpose, the radiation force is generated primarily through absorption. To enhance the absorption within the safety regulations, the radiation force is commonly generated by ultrasound with a higher frequency (5 - 10 MHz), limited pressure (< 5 MPa), and long duration (300 – 600 μs). In the current work, the acoustic radiation force is generated by ultrasound with similar

duration (450 – 600 μs) but a lower frequency (750 kHz) and a slightly higher pressure (5 - 6 MPa). The radiation force caused by the absorption could be low compared to other diagnostic setups because the absorption decreases with decreasing frequencies. However, the combination of low frequency, high pressure, and long pulse duration could have increased the likelihood of cavitation. The acoustic radiation force could be generated from the strong reflection from the cavitation bubbles. This is supported by the observation of cavitation bubbles generated in the push location after the push pulses were delivered (Figure V-7). These bubbles produced noticeable damage on the histological sections of the tissues. Therefore, we envision this setup to be applied within the target volume where the push location will be ablated eventually.

One issue of imaging the histotripsy lesions with shear wave elastography is that the shear waves may not be able to propagate across a sufficiently fractionated volume. This makes it difficult to outline the entire lesion, especially on the far end opposite to the shear wave excitation location. This issue may be addressed with an image compounding technique shown in **Figure V-14**. Two elasticity images were obtained separately with shear waves excited from the left or right side of the lesion. Using a simple image registration algorithm applied on the B-mode images, the two elasticity images can be combined to provide an elasticity map of the entire lesion.

Challenges may exist when applying the current setup for image feedback in *in vivo* situations in real time. For example, the computation for an elasticity image currently takes several minutes. This time may be significantly reduced by optimizing the data processing algorithms, allowing for close-to-real-time feedback. Another challenge may arise from significant degradation of the image quality in deep-lying tissues, which could

affect the accuracy of tissue displacement tracking. The challenges and solutions will be investigated in the future.

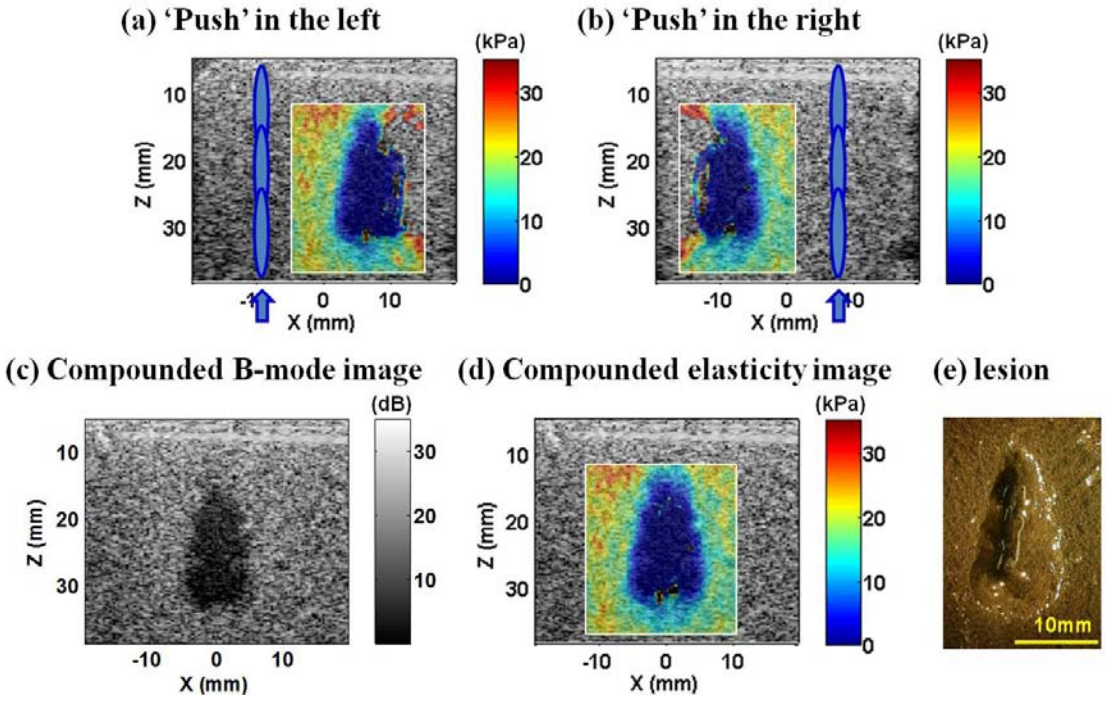

Figure V-14: Image compounding applied on a lesion produced in the tissue phantoms. Panels (a) and (b) show the lesion elasticity images produced with shear waves generated on the left and right sides of the lesions, respectively. Using a simple image registration algorithm, the two images were compounded to form the full lesion images (panels (c) and (d)). The compounded image better outlined the entire lesion as confirmed with the lesion morphology (panel (e)).

5.5 Conclusions

Tissues treated with histotripsy become increasingly softer as they are fractionated by increasing numbers of therapy pulses. This tissue transformation process can be detected with high sensitivity using shear wave elastography. The created lesions depicted on the elasticity images correspond well with their morphological appearance. Strong correlation exists between the lesion elasticity and the degree of tissue fractionation as examined by the percentage of remaining structurally intact cell nuclei. Since damage to the cell nuclei is directly related to cell death, tissue injury, and many other clinical outcomes, this correlation provides basis for predicting histotripsy treatment outcomes from tissue elasticity change, allowing for a clinician to determine when sufficient treatment has occurred.

5.6 References

[1] T. L. Hall, "Histotripsy: Non-invasive ultrasound surgery," University of Michigan, Ann Arbor, 2007.

[2] K. J. Parker, S. R. Huang, R. A. Musulin, and R. M. Lerner, "Tissue response to mechanical vibrations for "sonoelasticity imaging"," *Ultrasound Med Biol,* vol. 16, pp. 241-6, 1990.

[3] J. Ophir, I. Cespedes, H. Ponnekanti, Y. Yazdi, and X. Li, "Elastography: a quantitative method for imaging the elasticity of biological tissues," *Ultrason Imaging,* vol. 13, pp. 111-34, Apr 1991.

[4] M. O'Donnell, A. R. Skovoroda, B. M. Shapo, and S. Y. Emelianov, "Internal displacement and strain imaging using ultrasonic speckle tracking," *IEEE Trans Ultrason Ferroelectr Freq Control,* vol. 41, pp. 314-325, 1994.

[5] R. Muthupillai, D. J. Lomas, P. J. Rossman, J. F. Greenleaf, A. Manduca, and R. L. Ehman, "Magnetic resonance elastography by direct visualization of propagating acoustic strain waves," *Science,* vol. 269, pp. 1854-7, Sep 29 1995.

[6] K. Nightingale, M. S. Soo, R. Nightingale, and G. Trahey, "Acoustic radiation force impulse imaging: in vivo demonstration of clinical feasibility," *Ultrasound Med Biol,* vol. 28, pp. 227-35, Feb 2002.

[7] L. Sandrin, M. Tanter, S. Catheline, and M. Fink, "Shear modulus imaging with 2-D transient elastography," *IEEE Trans Ultrason Ferroelectr Freq Control,* vol. 49, pp. 426-35, Apr 2002.

[8] Z. Wu, L. S. Taylor, D. J. Rubens, and K. J. Parker, "Sonoelastographic imaging of interference patterns for estimation of the shear velocity of homogeneous biomaterials," *Phys Med Biol,* vol. 49, pp. 911-22, Mar 21 2004.

[9] L. Sandrin, B. Fourquet, J. M. Hasquenoph, S. Yon, C. Fournier, F. Mal, C. Christidis, M. Ziol, B. Poulet, F. Kazemi, M. Beaugrand, and R. Palau, "Transient elastography: a new noninvasive method for assessment of hepatic fibrosis," *Ultrasound Med Biol,* vol. 29, pp. 1705-13, Dec 2003.

[10] T. A. Krouskop, T. M. Wheeler, F. Kallel, B. S. Garra, and T. Hall, "Elastic moduli of breast and prostate tissues under compression," *Ultrason Imaging,* vol. 20, pp. 260-74, Oct 1998.

[11] J. Ophir, S. K. Alam, B. Garra, F. Kallel, E. Konofagou, T. Krouskop, and T. Varghese, "Elastography: ultrasonic estimation and imaging of the elastic properties of tissues," *Proc Inst Mech Eng H,* vol. 213, pp. 203-33, 1999.

[12] A. P. Sarvazyan, O. V. Rudenko, S. D. Swanson, J. B. Fowlkes, and S. Y. Emelianov, "Shear wave elasticity imaging: a new ultrasonic technology of medical diagnostics," *Ultrasound Med Biol,* vol. 24, pp. 1419-35, Nov 1998.

[13] J. Bercoff, M. Tanter, and M. Fink, "Supersonic shear imaging: a new technique for soft tissue elasticity mapping," *IEEE Trans Ultrason Ferroelectr Freq Control,* vol. 51, pp. 396-409, Apr 2004.

[14] M. Fatemi and J. F. Greenleaf, "Probing the dynamics of tissue at low frequencies with the radiation force of ultrasound," *Phys Med Biol,* vol. 45, pp. 1449-64, Jun 2000.

[15] W. F. Walker, F. J. Fernandez, and L. A. Negron, "A method of imaging viscoelastic parameters with acoustic radiation force," *Phys Med Biol,* vol. 45, pp. 1437-47, Jun 2000.
[16] K. R. Nightingale, M. L. Palmeri, R. W. Nightingale, and G. E. Trahey, "On the feasibility of remote palpation using acoustic radiation force," *J Acoust Soc Am,* vol. 110, pp. 625-34, Jul 2001.
[17] Y. C. Fung, *Mechanical properties of living tissues*, 1988.
[18] J. L. Gennisson and G. Cloutier, "Sol-gel transition in agar-gelatin mixtures studied with transient elastography," *IEEE Trans Ultrason Ferroelectr Freq Control,* vol. 53, pp. 716-23, Apr 2006.
[19] J. McLaughlin and D. Renzi, "Shear wave speed recovery in transient elastography and supersonic imaging using propagating fronts," *Inverse Problems,* vol. 22, p. 681, 2006.
[20] M. L. Palmeri, M. H. Wang, J. J. Dahl, K. D. Frinkley, and K. R. Nightingale, "Quantifying hepatic shear modulus in vivo using acoustic radiation force," *Ultrasound Med Biol,* vol. 34, pp. 546-58, Apr 2008.
[21] S. Chen, M. W. Urban, C. Pislaru, R. Kinnick, Y. Zheng, A. Yao, and J. F. Greenleaf, "Shearwave dispersion ultrasound vibrometry (SDUV) for measuring tissue elasticity and viscosity," *IEEE Trans Ultrason Ferroelectr Freq Control,* vol. 56, pp. 55-62, Jan 2009.
[22] M. Muller, J. L. Gennisson, T. Deffieux, M. Tanter, and M. Fink, "Quantitative viscoelasticity mapping of human liver using supersonic shear imaging: preliminary in vivo feasibility study," *Ultrasound Med Biol,* vol. 35, pp. 219-29, Feb 2009.
[23] S. Y. Emelianov, M. A. Lubinski, W. F. Weitzel, R. C. Wiggins, A. R. Skovoroda, and M. O'Donnell, "Elasticity imaging for early detection of renal pathology," *Ultrasound Med Biol,* vol. 21, pp. 871-83, 1995.
[24] W. C. Yeh, P. C. Li, Y. M. Jeng, H. C. Hsu, P. L. Kuo, M. L. Li, P. M. Yang, and P. H. Lee, "Elastic modulus measurements of human liver and correlation with pathology," *Ultrasound Med Biol,* vol. 28, pp. 467-74, Apr 2002.
[25] L. A. Frizzell and E. L. Carstensen, "Shear properties of mammalian tissues at low megahertz frequencies," *J Acoust Soc Am,* vol. 60, pp. 1409-11, Dec 1976.
[26] S. A. Goss, R. L. Johnston, and F. Dunn, "Comprehensive compilation of empirical ultrasonic properties of mammalian tissues," *J Acoust Soc Am,* vol. 64, pp. 423-57, Aug 1978.
[27] J. Bercoff, S. Chaffai, M. Tanter, L. Sandrin, S. Catheline, M. Fink, J. L. Gennisson, and M. Meunier, "In vivo breast tumor detection using transient elastography," *Ultrasound Med Biol,* vol. 29, pp. 1387-96, Oct 2003.
[28] M. F. Insana, C. Pellot-Barakat, M. Sridhar, and K. K. Lindfors, "Viscoelastic imaging of breast tumor microenvironment with ultrasound," *J Mammary Gland Biol Neoplasia,* vol. 9, pp. 393-404, Oct 2004.
[29] M. Tanter, J. Bercoff, A. Athanasiou, T. Deffieux, J. L. Gennisson, G. Montaldo, M. Muller, A. Tardivon, and M. Fink, "Quantitative assessment of breast lesion viscoelasticity: initial clinical results using supersonic shear imaging," *Ultrasound Med Biol,* vol. 34, pp. 1373-86, Sep 2008.

[30] N. S. Shah, S. A. Kruse, D. J. Lager, G. Farell-Baril, J. C. Lieske, B. F. King, and R. L. Ehman, "Evaluation of renal parenchymal disease in a rat model with magnetic resonance elastography," *Magn Reson Med,* vol. 52, pp. 56-64, Jul 2004.
[31] W. F. Weitzel, K. Kim, J. M. Rubin, H. Xie, and M. O'Donnell, "Renal advances in ultrasound elasticity imaging: measuring the compliance of arteries and kidneys in end-stage renal disease," *Blood Purif,* vol. 23, pp. 10-7, 2005.
[32] F. L. Lizzi, R. Muratore, C. X. Deng, J. A. Ketterling, S. K. Alam, S. Mikaelian, and A. Kalisz, "Radiation-force technique to monitor lesions during ultrasonic therapy," *Ultrasound Med Biol,* vol. 29, pp. 1593-605, Nov 2003.
[33] S. Bharat, U. Techavipoo, M. Z. Kiss, W. Liu, and T. Varghese, "Monitoring stiffness changes in lesions after radiofrequency ablation at different temperatures and durations of ablation," *Ultrasound Med Biol,* vol. 31, pp. 415-22, Mar 2005.
[34] T. Varghese, J. A. Zagzebski, and F. T. Lee, Jr., "Elastographic imaging of thermal lesions in the liver in vivo following radiofrequency ablation: preliminary results," *Ultrasound Med Biol,* vol. 28, pp. 1467-73, Nov-Dec 2002.
[35] R. Righetti, F. Kallel, R. J. Stafford, R. E. Price, T. A. Krouskop, J. D. Hazle, and J. Ophir, "Elastographic characterization of HIFU-induced lesions in canine livers," *Ultrasound Med Biol,* vol. 25, pp. 1099-113, Sep 1999.
[36] T. Wu, J. P. Felmlee, J. F. Greenleaf, S. J. Riederer, and R. L. Ehman, "Assessment of thermal tissue ablation with MR elastography," *Magn Reson Med,* vol. 45, pp. 80-7, Jan 2001.
[37] B. J. Fahey, R. C. Nelson, S. J. Hsu, D. P. Bradway, D. M. Dumont, and G. E. Trahey, "In vivo guidance and assessment of liver radio-frequency ablation with acoustic radiation force elastography," *Ultrasound Med Biol,* vol. 34, pp. 1590-603, Oct 2008.
[38] J. E. Parsons, C. A. Cain, and J. B. Fowlkes, "Cost-effective assembly of a basic fiber-optic hydrophone for measurement of high-amplitude therapeutic ultrasound fields," *J. Acoust. Soc. Am.,* vol. 119, pp. 1432-1440, Mar 2006.
[39] M. M. Burlew, E. L. Madsen, J. A. Zagzebski, R. A. Banjavic, and S. W. Sum, "A new ultrasound tissue-equivalent material," *Radiology,* vol. 134, pp. 517-20, Feb 1980.
[40] F. A. Duck, *Physical properties of tissue : a comprehensive reference book*. London: Academic, 1990.
[41] M. A. Lubinski, S. Y. Emelianov, and M. O'Donnell, "Speckle tracking methods for ultrasonic elasticity imaging using short-time correlation," *IEEE Trans Ultrason Ferroelectr Freq Control,* vol. 46, pp. 82-96, 1999.
[42] R. Q. Erkamp, P. Wiggins, A. R. Skovoroda, S. Y. Emelianov, and M. O'Donnell, "Measuring the elastic modulus of small tissue samples," *Ultrason Imaging,* vol. 20, pp. 17-28, Jan 1998.
[43] T.-Y. Wang, Z. Xu, F. Winterroth, T. L. Hall, J. B. Fowlkes, E. D. Rothman, W. W. Roberts, and C. A. Cain, "Quantitative Ultrasound Backscatter for Pulsed Cavitational Ultrasound Therapy - Histotripsy," *IEEE Trans. Ultrason. Ferroelectr. Freq. Control.,* vol. 56, pp. 995-1005, 2009.
[44] F. Winterroth, Z. Xu, T. Y. Wang, J. E. Wilkinson, J. B. Fowlkes, W. W. Roberts, and C. A. Cain, "Examining and analyzing subcellular morphology of renal tissue treated by histotripsy," *Ultrasound Med Biol,* vol. 37, pp. 78-86, Jan 2011.

[45] T. L. Hall, J. B. Fowlkes, and C. A. Cain, "A real-time measure of cavitation induced tissue disruption by ultrasound imaging backscatter reduction," *IEEE Trans. Ultrason., Ferroelect., Freq. Contr.,* vol. 54, pp. 569-575, Mar 2007.

[46] S. C. Roy, M. Paulose, and C. A. Grimes, "The effect of TiO2 nanotubes in the enhancement of blood clotting for the control of hemorrhage," *Biomaterials,* vol. 28, pp. 4667-72, Nov 2007.

[47] T. J. Hall, M. Bilgen, M. F. Insana, and T. A. Krouskop, "Phantom materials for elastography," *IEEE Trans Ultrason Ferroelectr Freq Control,* vol. 44, pp. 1355-1365, Nov. 1997 1997.

[48] M. Cooper, X. Zhen, E. D. Rothman, A. M. Levin, A. P. Advincula, J. B. Fowlkes, and C. A. Cain, "Controlled ultrasound tissue erosion: the effects of tissue type, exposure parameters and the role of dynamic microbubble activity," in *Ultrasonics Symposium, 2004 IEEE*, 2004, pp. 1808-1811 Vol.3.

[49] A. Hostettler, D. George, Y. Remond, S. A. Nicolau, L. Soler, and J. Marescaux, "Bulk modulus and volume variation measurement of the liver and the kidneys in vivo using abdominal kinetics during free breathing," *Comput Methods Programs Biomed,* vol. 100, pp. 149-57, Nov. 2010 2010.

[50] N. Nitta and T. Shiina, "Estimation of Nonlinear Elasticity Parameter of Tissues by Ultrasound," *Jpn. J. Appl. Phys.,* vol. 41, pp. 3572-2578, May 2002 2002.

[51] C. Amador, M. W. Urban, L. V. Warner, and J. F. Greenleaf, "In vitro renal cortex elasticity and viscosity measurements with Shearwave Dispersion Ultrasound Vibrometry (SDUV) on swine kidney," in *31st Annual International Conference of the IEEE EMBS*, Minneapolis, Minnesota, USA, 2009, pp. 4428-4431.

[52] L. Warner, M. Yin, R. L. Ehman, and L. O. Lerman, "Kidney Stiffness Measured in an Animal Model of Unilateral Renal Arterial Stenosis Using 2D MR Elastography," in *Proc. Intl. Soc. Mag. Reson. Med.*, 2009, p. 406.

[53] B. J. Fahey, K. R. Nightingale, S. A. McAleavey, M. L. Palmeri, P. D. Wolf, and G. E. Trahey, "Acoustic radiation force impulse imaging of myocardial radiofrequency ablation: initial in vivo results," *IEEE Trans Ultrason Ferroelectr Freq Control,* vol. 52, pp. 631-41, Apr 2005.

CHAPTER VI. IMAGING FEEDBACK FOR HISTOTRIPSY WITH SHEARWAVE PROPAGATION CHARACTERISTICS

6.1 Introduction

As shown in the previous chapters, histotripsy has significant potential to be developed into an image-guided modality for noninvasive ultrasound tissue ablation therapy. The ultrasound backscatter intensity decreased monotonically with increasing degrees of tissue damage [1, 2]. Because these ultrasound parameters are related to the size and concentration of the ultrasound scatterers [3], the change in these imaging parameters likely occurs as a direct result of the tissue fractionation caused by histotripsy. The ultrasound backscatter parameters, however, are not sensitive enough to detect lesions at an early stage of the treatments. More sensitive measurements can be provided with elasticity imaging or MR imaging. Using ultrasound shear wave elastography, we have detected significant decrease in the tissue elasticity even when a small therapy dose was delivered [4]. Using MR imaging, we have observed apparent change in the treated area in the T2-weighted images due to significant increase in the T2 relaxation time [5].

An interesting phenomenon was observed in our previous study where the lesion elasticity was mapped with shear wave elastography: the shear waves slowed down when they propagated across a tissue volume treated with histotripsy, and could cease to

propagate in a sufficiently fractionated volume [4]. This observation motivates the study presented here. We hypothesize that the shear waves would decay and eventually disappear if they are excited in a region progressively fractionated by histotripsy. This decay would result in apparent change in the shear wave propagation pattern, which can be characterized by the shear wave-induced displacement fields. Correlation between the characteristic change in the propagation pattern and the degree of tissue fractionation, if existing, may allow for interrogation of the treatment outcomes.

This chapter investigates the characteristic change of the shear waves generated in the target treatment volume as the volume is progressively fractionated with histotripsy. The shear waves were excited with acoustic radiation force of the focused ultrasound beams generated by the therapy transducer. First, to provide overview of the shear wave propagation pattern, the displacement fields induced by the shear waves were measured with ultrasound high speed plane wave imaging [6, 7]. Next, the temporal displacement profiles at a location in the shear propagation path were measured with ultrasound M-mode imaging. Finally, the characteristics (peak-to-peak displacements and time to peak displacement) of the temporal displacement profiles were calculated and correlated with the degree of tissue damage as examined via histology.

Although the feedback method presented here does not provide a full 2-D lesion image as other feedback methods do, it can be advantageous in several aspects. First, it may be as sensitive as the full frame elasticity imaging in detecting tissue change at an early stage of the treatments. Second, the computation is significantly reduced compared to full frame elasticity imaging, increasing likelihood of providing feedback information in real time. Third, the feedback metrics developed in this study can be implemented with

standard ultrasound M-mode imaging currently available on most systems. No special equipment is needed. Lastly, because the target volume is to be fractionated eventually, the intensity and duration of the pushing beams may be increased beyond the safety restraints imposed on ultrasound imaging, providing higher signal to noise ratio for the measurements.

6.2 Materials and Methods

6.2.1 Sample preparation

Experiments were performed on agar-graphite tissue mimicking phantoms and *ex vivo* porcine kidneys. The agar-graphite phantoms were agar-based hydrogel prepared with 0.8% agar (AG-SP, Lab Scientific, Livingston, NJ) and 3% graphite powder (Extra Fine Graphite Powder, Mr. Zip, Muskegon, MI). The porcine kidneys were obtained from a local processing facility. Freshly excised kidneys were preserved in normal saline at 4˚C and used within 48 hours of harvest. Prior to experimentation, the kidneys were placed in degassed (20% of normal saturation determined by pO_2) saline to allow for equilibrium of the temperature and gas concentration. The kidneys were then sectioned across the long axis into approximately 6 cm × 5 cm × 6 cm sections and embedded in 0.8% agar gel in a polycarbonate holder. Detailed description of the phantom and tissue preparation can be found in our previous publication [8].

6.2.2 Ultrasound generation and calibration

A 750-kHz therapeutic array transducer (Imasonic, Voray sur l'Ognon, France) was used to deliver both the therapy pulses and the 'push' pulses for shear wave generation. The transducer has a geometric focal length of 12 cm, with an aperture size of 15 cm and a center hole of 5.9 cm in diameter. The array is driven by a custom-built driving system that controls the driving amplitude and phase of each individual element. In this study, the array delivered both the therapy pulses and the 'push' pulses with all elements driven in-phase with equal amplitude, acting as a F/# 0.8 single element transducer.

The pressure fields of the therapy pulses and the push pulses were calibrated with a custom-built fiber optic probe hydrophone (FOPH) with an active element of 100 μm in diameter [9]. The pressure waveforms are shown in **Figure VI-1**. The peak negative (P−) and peak positive (P+) pressures, spatial peak pulse average intensity (I_{SPPA}), and the beam profiles were measured and summarized in **Table 1**.

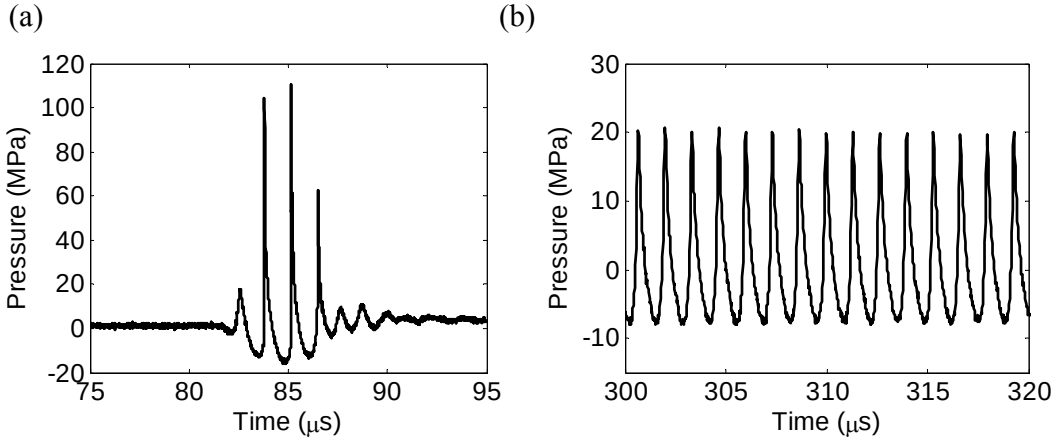

Figure VI-1: Pressure waveforms of (a) therapy pulse and (b) a segment of the push pulse measured under free field conditions.

Table VI-1: Pulse parameters of the therapy and the push pulses. Both pulses were generated by the 750-kHz therapy transducer with a F/# 0.8 focal configuration.

	Therapy pulses	Push pulses
P−/P+ pressure	-17/108 MPa*	-8/20 MPa*
Duration	3 cycles (4 μs)	200 cycles (267 μs)
I_{SPPA}	24.8 kW/cm^2	3.6 kW/cm^2
-6 dB beamwidths on the P− pressure profile**	2.6 mm (lateral) 17.8 mm (axial)	2.7 mm (lateral) 18.5 mm (axial)
-6 dB beamwidths on the P+ pressure profile**	1.2 mm (lateral) 7.3 mm (axial)	1.5 mm (lateral) 12.5 mm (axial)

* The pressures at the treatment location was expected lower due to acoustic attenuation (0.1 dB/cm/MHz in the graphite phantoms [10] and 1 dB/cm/MHz in the kidneys [11]). Given the 3 cm average penetration depth in this study, the P− pressure of the therapy pulse was likely 16.5 MPa in the phantoms and 13 MPa in the kidneys; the P− pressure of the push pulse was likely 8 MPa in the phantoms and 6 MPa in the kidneys. The P+ pressure was expected to decay more significantly due to nonlinear absorption.

** The beam profiles were measured at P−/P+ pressures of -11/58 MPa for the therapy pulse, and at -8/16 MPa for the push pulse. The beamwidths at experimental pressure levels could not be successfully measured because cavitation easily occurred and damaged the fiber tip during the pressure profile scan.

6.2.3 Image-guided histotripsy treatments

Histotripsy treatments were performed with the therapy pulses delivered at 50 Hz pulse repetition frequency (PRF). Image guidance and treatment feedback was provided before, during, and after the treatments with a 5-MHz linear array (L7-4, Philips Healthcare, Andover, MA) connected to a research ultrasound imaging system (V1, Verasonics, Redmond, WA). The imaging probe was mounted opposite to the therapeutic array (**Figure VI-2**).

Prior to the treatments, the imaging plane was aligned with the central axis of the therapeutic array by the following approach. A bubble cloud was generated in the water

by brief excitation of the therapeutic array. The imaging probe was positioned such that the maximal extent of the bubble cloud appeared on the image with the cloud's central axis approximately perpendicular to the imaging probe.

After the alignment, the phantoms or tissues were mounted to a motorized 3-axis positioning system and placed at the geometric focus of the therapeutic transducer between the therapy and image transducers. Lesions of approximately 7 mm × 7 mm × 14 mm were produced by mechanically scanning the therapy focus in a 5 × 5 grid with 1 mm spacing on the focal plane (**Figure VI-2**).

For the phantom experiments, the lesions were created with 2000 pulses per treatment location. The treatments were paused at 0, 100, 200, 300, 500, 1000, 1500, and 2000 pulses per treatment location for shear wave imaging (described in the following section). A total of 8 treatments were performed.

For the *ex vivo* tissue experiments, the lesions were created with 100, 200, 300, 500, 1000, 1500, or 2000 pulses per treatment location. Shear wave imaging was performed before and after the treatments. A total of 54 treatments, 6 - 9 for each dose, were performed on the *ex vivo* kidneys with the target volumes located in the cortex area. Selected treatments with 2000 pulses per treatment location were paused at 0, 100, 200, 300, 500, 1000, 1500, and 2000 pulses per treatment location during the treatments for shear wave imaging.

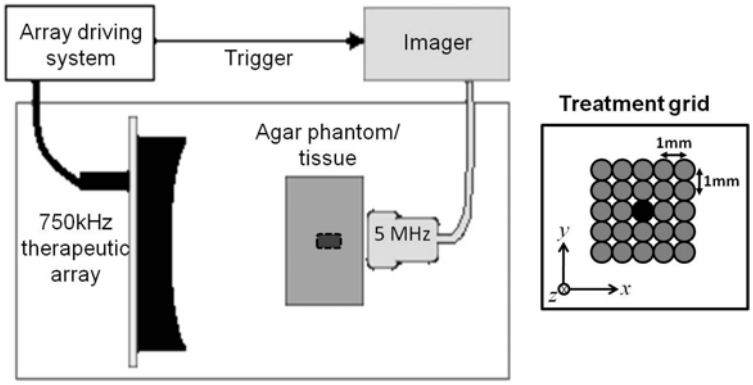

Figure VI-2: A schematic of the experimental setup. Experiments were performed in a tank of degassed (25 - 35% of gas saturation as determined by pO_2) water. The 750-kHz therapeutic transducer and the 5-MHz imaging probe were positioned on the opposite sides of the experimental samples, with the imaging plane aligned with the central axis of the therapeutic transducer. The 5×5 treatment grid is shown in the right panel with the 'push' location labeled in black.

6.2.4 Shear wave imaging

The shear waves were monitored with two imaging modes: 1) full frame mapping of the displacement field with ultrasound plane wave imaging [6, 7], and 2) M-mode imaging of the temporal displacement profile at a single location 10 mm lateral to the push source.

For full frame shear wave imaging, a plane wave was transmitted to illuminate the 38 mm × 38 mm field of view by simultaneously exciting all elements on the imaging probe. The echo signals were collected immediately after the transmitted pulse was completed. Because the imaging system can only simultaneously receive echo signals from 64 channels a time, two transmit-receive cycles were performed to reconstruct an image of the entire field of view. A total of 73 frames were acquired at a rate of 3000 frames per second, including 1 reference frame before the push beams and 72 frames

after the push beams. The total imaging duration lasted for ~25 ms. The collected raw channel data were stored and processed off-line with the following approach. The channel data were first delayed and summed at each location in the field of view, producing beamformed radio-frequency (RF) images. Dynamic receive focus with an F/# 1.5 configuration and a hanning window apodization were applied in the beamforming process. A correlation based 1-D speckle tracking technique was then applied to estimate the shear wave induced displacement in the axial direction [12]. The RF signals were transformed into analytical signals for speckle tracking. Each A-line was segmented into 1.5 mm regions with 75% overlap. For each region, the complex cross correlation function between the analytical signals from successively acquired frames was calculated. The peak correlation was located by searching the phase zero crossing of the phase near the maximum magnitude. The location of the peak correlation then determined the relative displacement between successive frames.

For single location shear wave detection, the shear wave induced displacement vs. time profile at a location lateral to the treatment volume with approximately 10 mm offset was monitored with M-mode imaging. The imaging array transmitted the imaging pulses focused at the monitor location with an F/#-2 focal configuration at an imaging PRF of 3000 Hz. To track the local displacement, the received signals were processed with beamforming and speckle tracking algorithms similar to those described earlier. The A-line signals were beamformed with an F/# 2.0 dynamic receive focus. A segment was gated from each A-line in a 1.5 mm region centered at the monitor location. The segments from successively acquired A-lines were cross correlated, allowing for estimation of the displacement. The temporal displacement profiles were obtained from 3

separate pushes delivered at a repetition rate of 1 Hz. The average profile was calculated and displayed immediately after the processing was completed (typically within a few seconds).

The peak-to-peak displacement and the relative time to peak displacement were calculated for the temporal displacement profiles measured with M-mode imaging. The averaged profiles were first upsampled 4 times with low pas interpolation. On the upsampled profiles, the peak-to-peak displacement was calculated as the difference between the peak positive (toward the imaging probe) and the peak negative (away from the imaging probe) displacements. The time to peak displacement was defined as the arrival time of the peak positive or peak negative displacement at the monitor location after the push pulse was fired. The relative time to peak displacement was further calculated by subtracting the time to peak displacement measured before the treatments from that measured after the treatments.

6.2.5 Morphological and histological examination of the lesions

Morphological examination was performed on selected lesions produced with the highest dose (i.e., 2000 pulses/location) in the phantoms and the tissues. The lesions were bisected transversely to reveal the cross sections approximately corresponding to the imaging plane. The fractionated debris, if present, can be visually identified as homogenized paste. This paste was irrigated away to reveal the homogenized volume.

Histological examination was conducted for the lesions produced in the tissues. The lesions were fixed and prepared for H&E staining. Histological sections of 4 μm

thickness were made at 500 μm intervals through the lesion with slices oriented in parallel with the ultrasound imaging plane. Quantitative examination of the degrees of histological damage was performed by calculating the percentage of the structurally intact cell nuclei in the lesions [2]. The number of structurally intact cell nuclei was counted in five selected regions in the treated area. An average count was obtained from the five counts. The average count was then divided by that in an untreated (control) area, producing the percentage of the remaining intact cell nuclei in the lesions.

6.3 Results

6.3.1 Phantom experiments

Full frame imaging

Representative B-mode images and shear displacement fields induced by acoustic radiation force applied in the treatment volume are illustrated in **Figure VI-3**. The treatment volume was easily identified as a hypoechoic area on the B-mode images. The lesion appeared increasingly hypoechoic with increasing numbers of therapy pulses (**Figure VI-3a**). The displacement fields were significantly altered when the volume was progressively fractionated with the therapy pulses. Before the treatments (control), spherically shaped shear waves were excited around the focus of the push beams and propagated laterally away from the push location. The propagation slowed down as the target volume was treated with a small to intermediate number of therapy pulses. The propagation slowed down more significantly in the region closer to the therapy transducer (i.e., the 'head' of the tadpole shaped lesion volume), resulting in a distorted shear

wavefront. The shear waves were never fully excited around the push region when the target volume was treated with a sufficiently high dose, although small-scale shear waves were occasionally induced locally at the proximal and/or the distal ends of the lesions (circled region at time = 4 ms in the 3rd row in **Figure VI-3b**).

It is observed that bubbles were generated and translated by the push pulses. Afterward, they could toward the therapy transducer, or migrated in the treatment volume over the course of several milliseconds. The bubble motion likely contributed to the large and noisy displacements detected in the treatment volume (shown in **Figure VI-3b**).

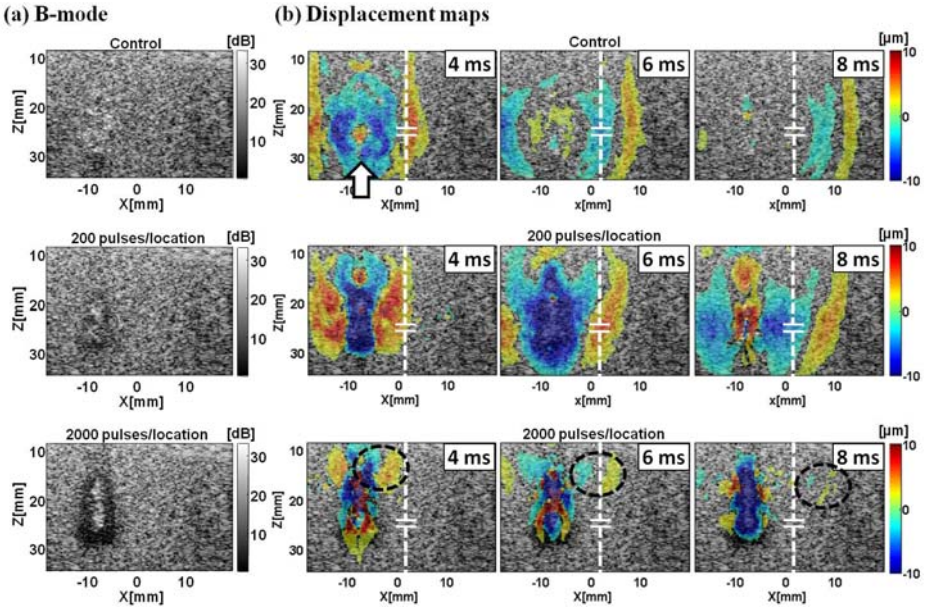

Figure VI-3: Representative (a) B-mode images acquired at 1 ms, and (b) displacement maps acquired at 4, 6, and 8 ms after the push pulse was fired. On the B-mode images, the treatment volume became increasing hypoechoic with increasing numbers of therapy pulses. Bubbles (hyperechoic clusters) were generated in the push location. On the displacement maps, spherically shaped shear waves were observed to propagate laterally away from the push location in the control. The propagation slowed down when a small therapy dose (200pulses/location) was applied, and ceased when a high dose (2000 pulses/location) was applied. The positive or negative displacements indicate directions of motions toward or away from the imaging probe.

M-mode imaging

Representative temporal displacement profiles detected at a location 10mm lateral to the lesion with M-mode imaging are shown in **Figure VI-4**. Before the treatment (control), maximum displacement of ~7 μm was reached approximately 5 ms after the push pulse was delivered. When the lesion was treated with a small dose (i.e., 100 pulses/treatment location), the maximum displacement remained unchanged, but the time to peak displacement was delayed. As the treatment dose was increased, the maximum displacement decreased, and the time to the peak relative displacement increased.

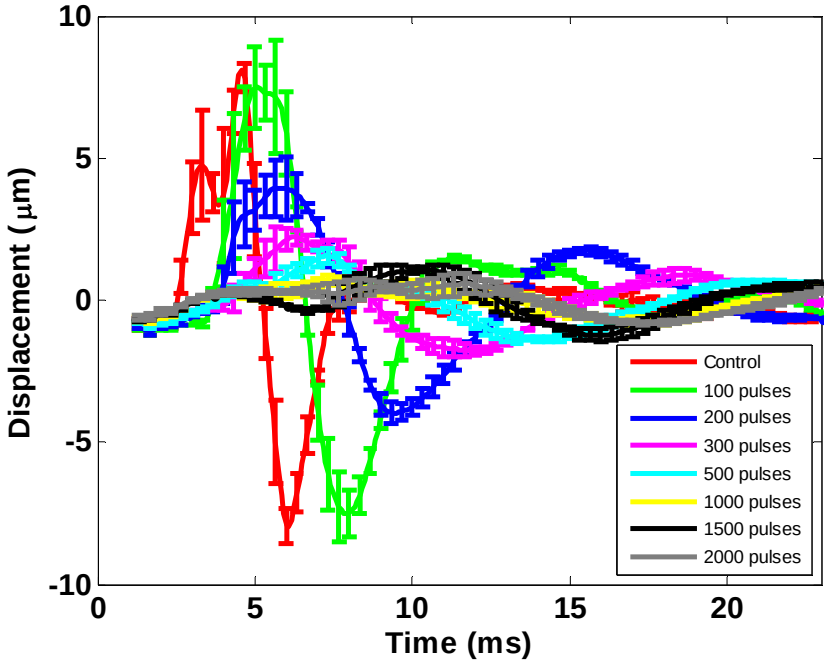

Figure VI-4: Representative temporal displacement profiles in the tissue phantoms. The profiles were recorded at a location lateral to the lesion with 10 mm offset with M-mode imaging (scanline and focus marked in Figure VI-3). Data are expressed in mean ± standard deviation of the displacements induced by 3 separate push pulses. The push pulses were fired at time 0. Before the treatments, the shear waves induced a maximum relative displacement of approximately 7 μm in either direction of motion. At a low dose (e.g., 100 pulses/treatment location), the maximum relative displacement remained unchanged, but the time to peak relative displacement was delayed. As the treatment doses increased, the maximum relative displacement decreased, and the time to the peak relative displacement increased.

The peak-to-peak displacement and the relative time to peak displacement were calculated from the temporal displacement profiles and shown in **Figure VI-5**. The peak-to-peak displacement decreased exponentially with increasing therapy doses. The relative time to peak displacement increased with increasing therapy doses in an exponential saturation trend. This trend was the same for the time to peak positive and the time to peak negative displacements. In this study, the relative time to peak negative displacement was illustrated and used for subsequent studies.

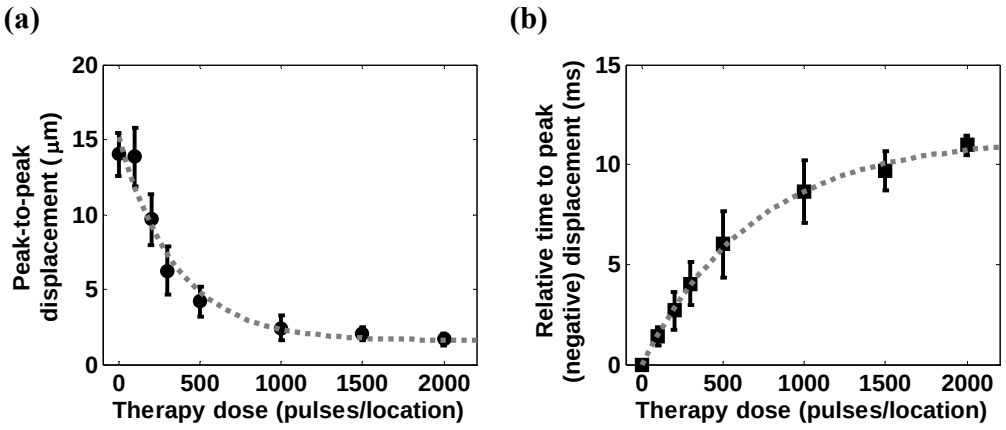

Figure VI-5: (a) The peak-to-peak displacement and (b) the relative time to peak negative displacement for the temporal displacement profiles measured at different therapy doses. Data represent mean ± standard deviation (N = 8). The peak-to-peak displacement decreased exponentially with increasing therapy doses. The dashed line is the exponential fit with the therapy dose centered at zero mean and scaled to unit standard deviation, i.e., $y = 1.82 \cdot e^{-2.10 \cdot ((x-700)/729)} + 1.58$ ($R^2 = 0.96$). The relative time to peak negative displacement increased in an exponential saturation trend. The dashed line is the exponential fit with the therapy dose centered at zero mean and scaled to unit standard deviation, i.e., $y = 7.67 - 3.96 \cdot e^{-0.68 \cdot ((x-700)/729)}$ ($R^2 = 0.99$).

6.3.2 Ex vivo tissue experiments

Full frame imaging

Representative B-mode images and shear displacement fields induced in the *ex vivo* tissues are shown in **Figure VI-6**. On the B-mode images, the treatment volume became increasing hypoechoic with increasing numbers of therapy pulses. Bubbles were generated by the push pulses and appeared as the hyperechoic clusters in the push location. The displacement maps in **Figure VI-6b** showed that the generation and the propagation of the shear waves were significantly changed as the target volume was treated with increasing numbers of therapy pulses. Before the treatments, the shear waves were excited and propagated away in the lateral direction before the treatments. The propagation slowed down when the target volume was treated with a low to intermediate number of pulses. The shear waves could not be excited when the target volume was treated with a sufficiently high therapy dose.

It is observed that the bubbles persisted in the treatment volume during the entire 25-ms imaging period. These bubbles were translated away from the transducer by the push pulses. Subsequent to the translation, they could quickly rebound back to their original positions within a few ms when the target volume was treated with a low to intermediate therapy dose, or slowly migrated in the treatment volume for > 10 ms when a sufficiently high dose was applied. Because the bubbles are strong reflectors for ultrasound, both the main lobes and the side lobes of the bubble images were detectable in the field of view on the images obtained with plane wave imaging. As the bubbles moved in the treatment volume, their side lobe images shifted as well as the main lobe images. The shift of the side lobes could cause artifacts in the regions lateral to the true

bubble locations (e.g., those indicated by the arrows in the 3rd row in **Figure VI-6b**). These artifacts were particularly noticeable at higher doses when the bubbles migrated over a longer period.

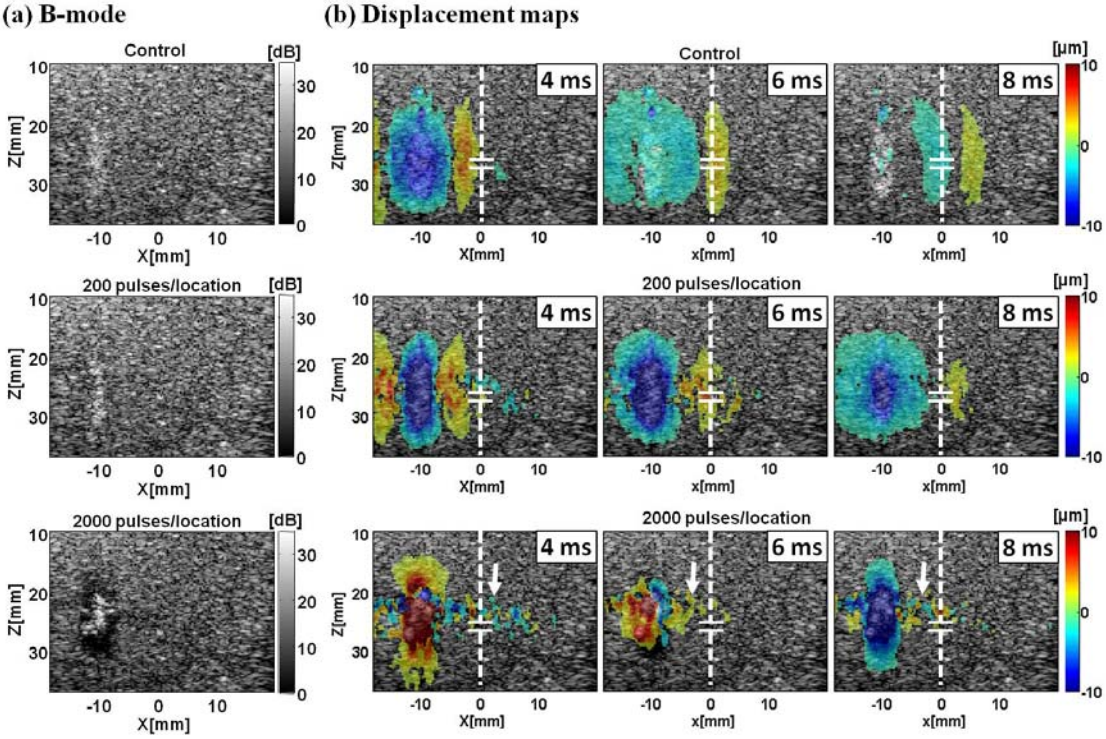

Figure VI-6: Representative (a) B-mode images acquired at 1 ms, and (b) displacement maps acquired at 4, 6, and 8 ms after the push pulse was fired. On the B-mode images, the treatment volume became increasing hypoechoic with increasing numbers of therapy pulses. Bubbles were generated by the push pulses and appeared as the hyperechoic clusters in the push location. On the displacement maps, the shear waves were excited and propagated away in the lateral direction before the treatments (1st row). The propagation slowed down when a small dose was applied (2nd row). The shear waves could not be excited when a sufficiently high therapy dose was delivered (3rd row). Noted that artifacts, possibly caused from the side lobes of the bubble images, are present (indicated by the arrows in the 3rd).

M-mode imaging

Representative temporal displacement profiles detected at a location 10mm lateral to the lesion with M-mode imaging are shown in **Figure VI-7**. Before the treatment (control), maximum displacement of ~4 μm was reached approximately 3 ms after the push pulse was fired. The maximum displacement decreased as the tissues were treated with increasing numbers of therapy pulses. Correspondingly, the time to the peak relative displacement increased with increasing numbers of therapy pulses.

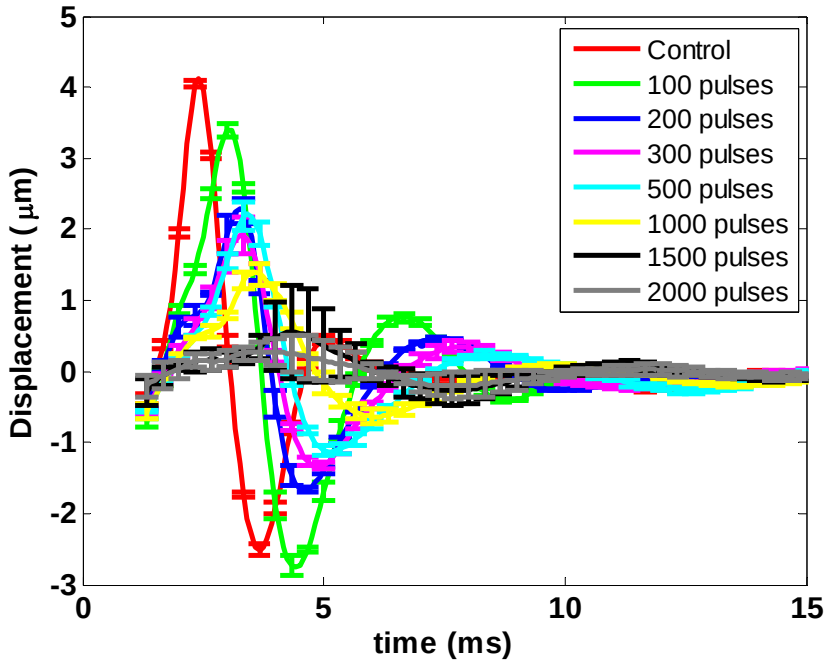

Figure VI-7: Representative temporal displacement profiles in the *ex vivo* kidneys. The profiles were recorded at a location lateral to the lesion with 10 mm offset with M-mode imaging (scanline and focus marked in Figure VI-6). Data are expressed in mean ± standard deviation of the displacements induced by 3 separate pushes. The push pulses were fired at time 0. Before the treatments, the shear waves induced a maximum relative displacement of ~4 μm. As the treatment doses increased, the maximum relative displacement decreased, and the time to the peak displacement increased.

The peak-to-peak displacement and the relative time to peak negative displacement were calculated and shown in **Figure VI-8**. The peak-to-peak displacement decreased exponentially with increasing therapy doses. The relative time to peak displacement increased with increasing therapy doses in an exponential saturation trend.

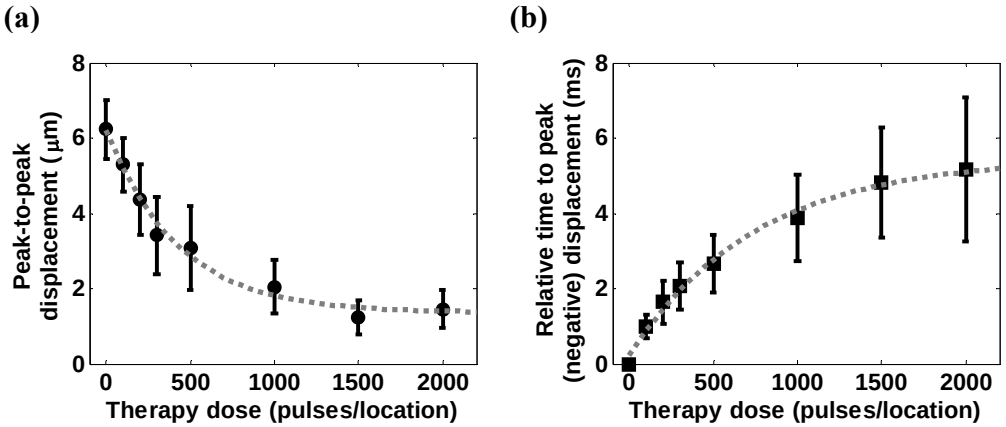

Figure VI-8: (a) The peak-to-peak displacement and (b) the relative time to peak negative displacement for the temporal displacement profiles measured in the *ex vivo* kidneys treated with different therapy doses. Data represent mean ± standard deviation from 6 - 9 experiments each dose. The peak-to-peak displacement decreased exponentially with increasing therapy doses (dashed line: $y = 0.94 \cdot e^{-1.71 \cdot ((x-700)/729)} + 1.36$, $R^2 = 0.99$). The relative time to peak negative displacement increased in an exponential saturation trend (dashed line: $y = 5.47 - 2.07 \cdot e^{-0.97 \cdot ((x-700)/729)}$, $R^2 = 0.99$).

6.3.3 Lesion morphology and histology

The phantoms were fractionated to very fine 'paste-like' homogenate in the treatment volume. The homogenate remained paste-like long (~hours) after the treatments and never resolidified to the gel status, indicating that the phantoms were disrupted mechanically rather than thermally. The homogenate could be easily irrigated out to reveal a smooth cavity (**Figure VI-9a**). The size and shape of the cavity approximately

matched with those of the hypoechoic area on the B-mode images (3rd row in **Figure VI-3a**). Similarly, the tissues were fractionated to 'paste-like' homogenate (**Figure VI-9b**, left), which could be easily irrigated out to reveal a smooth cavity (**Figure VI-9b**, right). The size and shape of the cavity approximately matched with those of the hypoechoic area on the B-mode images (3rd row in **Figure VI-6a**).

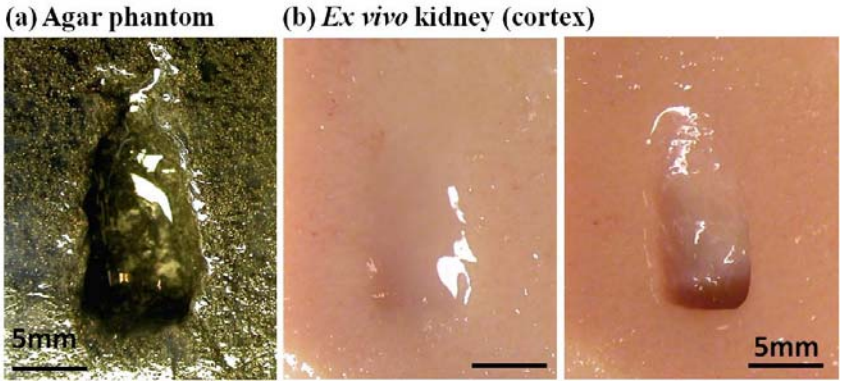

Figure VI-9: Representative morphological images of the lesions produced in (a) agar phantom and (b) *ex vivo* kidneys after treatments with 2000 pulses/treatment location. The phantom or tissues were fractionated to "paste-like" homogenate in the treated volume (e.g., the left picture in panel (b)). The homogenate could be easily irrigated out to reveal a smooth cavity (panel (a) and the right picture in panel (b)).

Representative histology of the lesions treated with increasing therapy pulses are shown in **Figure VI-10**. In the control, all tissue and cellular structures appeared structurally intact. When a small dose (100 – 200 pulses/treatment location) was applied, disrupted tissue structures were present in the treatment volume. While most cells appeared normal structurally intact with normal appearing cell nuclei, cells with condensed or fragmented nuclei were present. As the therapy doses were increased (e.g., 300 – 1000 pulses/treatment location), more tissue structures and cells were damaged.

Areas of tissue homogenized appeared in the treatment volume, and the area increased with increasing therapy doses. At sufficiently high doses (>1000 pulses/treatment location), the treated volume appeared completely homogenized with no recognizable tissue structures and very few, if present, fragments of nuclear material. The tissues outside the treatment volume appeared structurally intact. A transition zone of ~100 μm with incompletely fractionated structures was present between the homogenized volume and the surrounding intact tissues.

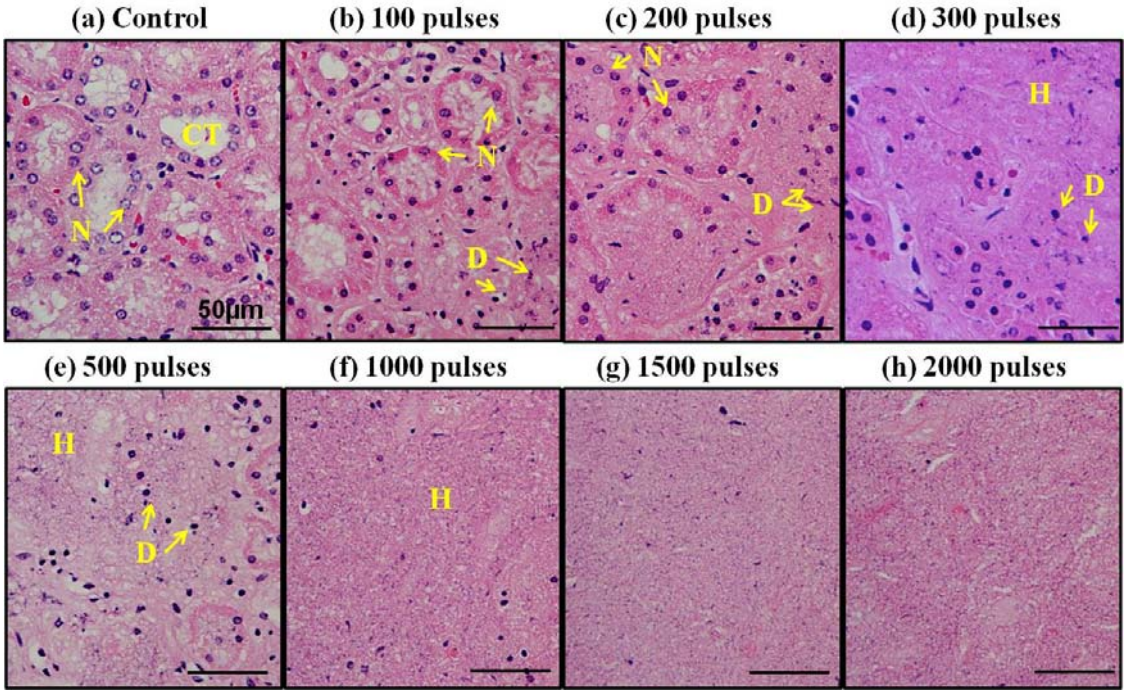

Figure VI-10: Representative histological sections of the lesions produced with therapy doses from 0 (control) to 2000 pulses per treatment location. In the control, all tissue structures (e.g., the collecting tubules (CT)) and cells appeared structurally intact. When a small therapy dose was applied, subvolumes of disrupted tissues and acellular debris were observed. While most cells appeared structurally intact with normal appearing cell nuclei (N), damaged cells (D) with condensed, fragmented or absence of nuclei, were present. As the treatment doses were increased, more tissue structures and cells were fractionated, producing areas of tissue and cellular homogenate (H). At sufficiently high doses (>1000 pulses/treatment location), the treated volume appeared completely homogenized.

The percentage of the normal appearing cell nuclei in the treatment volume was calculated and plotted against the therapy doses in **Figure VI-11**. This percentage decreased exponentially with increasing doses (R^2 = 0.99), and reached nearly zero at 1500 pulses per treatment location.

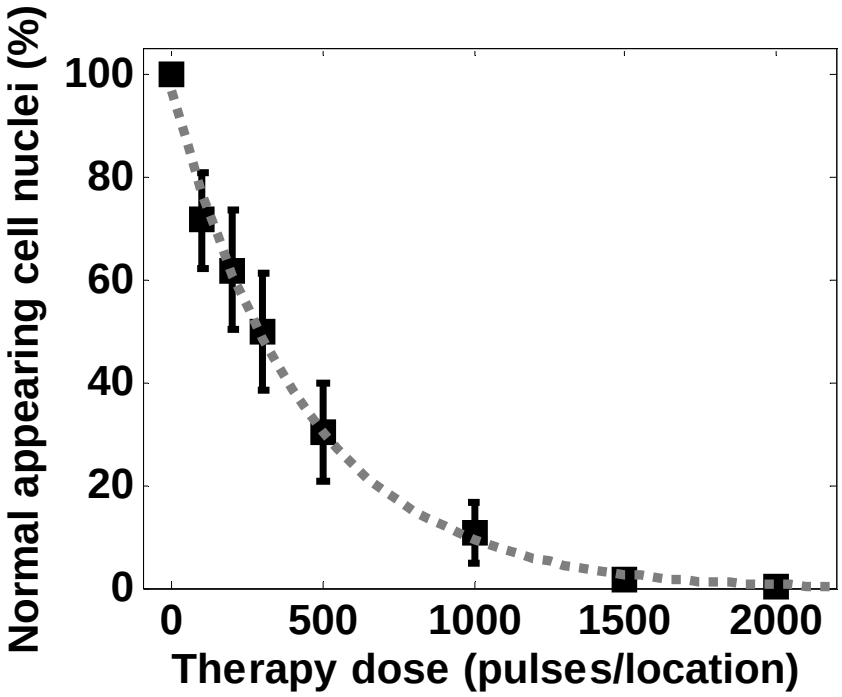

Figure VI-11: Percentage of normal appearing cell nuclei remaining in the lesions against the therapy doses. Data represent mean ± standard deviation from 6 – 9 experiments for each dose. The percentage decreased exponentially with increasing therapy doses. Dashed line: $y = 0.19 \cdot e^{-1.68 \cdot ((x-700)/729)} - 0.0036$ **(R^2 = 0.99).**

To evaluate the feasibility of using the parameters derived from the temporal displacement profiles as feedback for the degree of tissue damage, the percentage of normal appearing cell nuclei was correlated with the peak-to-peak displacement and the relative time to peak negative displacement (**Fig. 12**). The percentage of normal

appearing cell nuclei decreased linearly with decreasing peak-to-peak displacement (R^2 = 0.98) and increasing relative time to peak negative displacement (R^2 = 0.97).

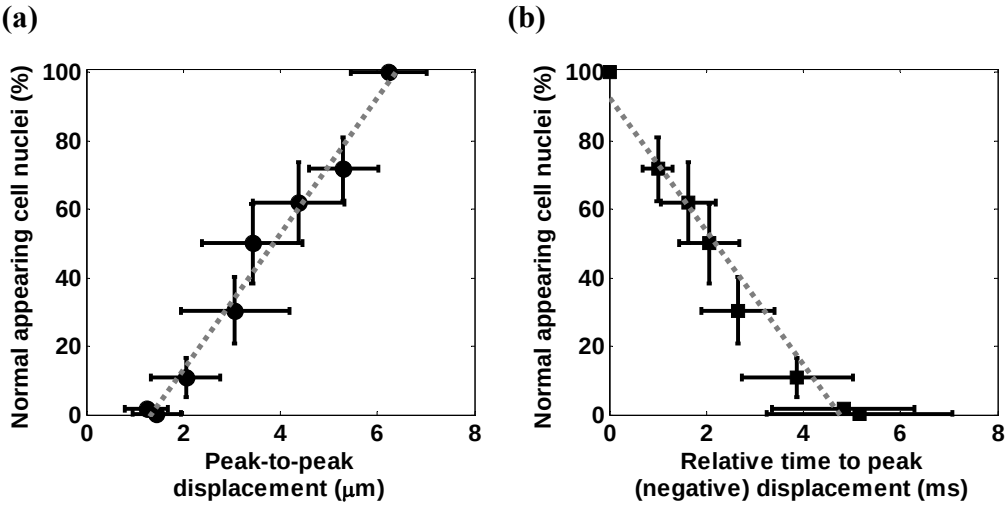

Figure VI-12: Percentage of normal appearing cell nuclei as functions of (a) peak-to-peak displacement, and (b) relative time to peak negative displacement of the temporal displacement profiles measured at the monitor location (10mm lateral to the lesion). The percentage of normal appearing cell nuclei decreased with decreasing peak-to-peak displacement and increasing relative time to peak negative displacement. Strong linear correlations were found for both functions. Data represent mean ± standard deviation from 6 - 9 experiments each. Dashed line in panel (a): $y = 0.20 \cdot x - 0.26$ ($R^2 = 0.98$). Dashed line in panel (b): $y = -0.19 \cdot x + 0.92$ ($R^2 = 0.97$).

6.4 Discussion

Small peak-to-peak displacements were measured even when the tissues were 100% damaged as examined via histology (see **Figure VI-12a**). The small tissue displacements likely coupled from the small-scale shear waves induced at the proximal and/or the distal ends of the lesions with respect to the therapy transducer (e.g., **Figure**

VI-3b). The small-scale shear waves were probably induced because the focal region of the ultrasonic pushing beam was longer than that of the therapy pulses (as evidenced in **Table VI-1**). The acoustic radiation force applied to the insufficiently homogenized regions near the lesion boundaries could induce the small scale shear waves in the local area. This suggests that the minimum size of the lesion volume to be interrogated for treatment outcomes should be larger than the focal volume of the pushing beam. Our preliminary tests indicated the lesions created by the 5×5 treatment grid used in this study to be an appropriate unit for interrogation with this method.

In practical applications, this feedback approach presented here may be performed before and intermittently during the treatments until sufficient treatments have occurred. For instance, the treatment may be temporally paused for the shear wave displacement profile measurements. The profiles are compared to that obtained before the treatments. The treatments continue until no shear waves are detected. The short intermittent pause (a few seconds) should have very minimal effects on the treatment progression since the histotripsy is a mechanical disruption process. It is noted that the bubbles generated by the pushing beams caused noticeable damage as examined via histology. This damage is acceptable in the current study since the push location is to be fractionated eventually.

One potential challenge of this feedback method is that the measured displacements and time may differ in different organs due to the difference in their viscoelasticity properties. Patient-to-patient difference may also exist even for the same organ. Despite the potential variance in the absolute measurements, the trends (i.e., exponential decay in the peak-to-peak displacements and exponential saturation of the time to peak displacement) are expected to hold. Therefore, the treatments may continue

until the saturation of both parameters is observed in order to ensure successful treatments. Such over-treatment procedures should produce few deleterious effects since the histotripsy process is often self-limiting to a natural structure (e.g., the collecting system in the kidneys [13]).

The bubbles generated by the push pulses could sometimes complicate the measurements of the displacement fields in the regions lateral to the bubble locations. With plane wave imaging, the main lobe and the side lobe images of point targets are both present within the field of view (e.g., shown in [14]). Because the bubbles are strong reflectors for ultrasound compared to the phantom or the tissues, both the main lobe and the side lobes of the bubbles could appear in the images acquired in this study. The main lobe of the bubble image appeared in the treatment volume as very bright (hyperechoic) spots, and the side lobe appeared in the regions lateral to the bubbles in the field of view. As the bubbles translated in the treatment volume, the side lobe signals moved as well as the main lobe signals. This may cause motion artifacts in the lateral regions (e.g., 3rd row in **Figure VI-6b**). The side lobe signals can be suppressed with improved beamforming algorithms. In this study, hanning window apodization was applied in the receive beamforming algorithm to suppress the side lobe signals by ~35 dB. This removed a large part of the artifacts, but was still ineffective when large clusters of bubbles were excited. Further improvements may be achieved with more sophisticated algorithms such as those developed in the literature [14].

On the other hand, the bubbles generated by the push pulses may be used as a convenient tracking object for elasticity imaging. Many researchers have demonstrated that the displacement in response to the external force, either mechanical push or acoustic

radiation force, can be used to gauge the elasticity for disease diagnosis or treatment evaluation [15-20]. However, if the target tissues are seated deeply in the body, it is likely that the image quality would be significantly degraded. Tracking the tissue displacement from the tissue speckle patterns may be difficult with poor image quality. In this case, the bubbles may become convenient tracking object since they may remain clearly identified in deep seated tissues. Tracking the displacement of the bubbles could be equivalent to tracking that of the tissues, allowing elasticity estimation in deep seated tissue. Investigation on the feasibility of this method is underway.

6.5 Conclusions

This study demonstrates that the propagation of the shear waves, indicated by the temporal displacement profiles, changes significantly when the tissues at the push location are progressively fractionated by histotripsy. Such change can be easily detected with conventional ultrasound M-mode imaging. Quantitative measurements (i.e., the peak-to-peak displacements and the time to peak displacement) extracted from the temporal displacement profiles decrease or increase monotonically, and eventually saturate, with increasing doses. More importantly, the decrease or increase of these measurements is strongly correlated with the degree of tissue damage. These results indicate that the shear temporal displacement profiles contain abundant information about the degree of tissue fractionation. Monitoring the shear temporal displacement profiles may be an applicable feedback strategy for evaluating the efficacy of histotripsy treatments in real time.

6.6 References

[1] T. L. Hall, J. B. Fowlkes, and C. A. Cain, "A real-time measure of cavitation induced tissue disruption by ultrasound imaging backscatter reduction," IEEE Trans. Ultrason., Ferroelect., Freq. Contr., vol. 54, pp. 569-575, Mar 2007.

[2] T.-Y. Wang, Z. Xu, F. Winterroth, T. L. Hall, J. B. Fowlkes, E. D. Rothman, W. W. Roberts, and C. A. Cain, "Quantitative Ultrasound Backscatter for Pulsed Cavitational Ultrasound Therapy - Histotripsy," IEEE Trans. Ultrason. Ferroelectr. Freq. Control., vol. 56, pp. 995-1005, 2009.

[3] F. L. Lizzi, M. Greenebaum, E. J. Feleppa, M. Elbaum, and D. J. Coleman, "Theoretical framework for spectrum analysis in ultrasonic tissue characterization," J. Acoust. Soc. Amer., vol. 73, pp. 1366-1373, 1983.

[4] T.-Y. Wang, T. L. Hall, Z. Xu, J. B. Fowlkes, and C. A. Cain, "Imaging Feedback of Histotripsy Treatments With Ultrasound Transient Elastography," in Proc. IEEE Ultrason. Symp., Orlando, USA, 2011 (accepted).

[5] T. L. Hall, "Histotripsy: Non-invasive ultrasound surgery," University of Michigan, Ann Arbor, 2007.

[6] L. Sandrin, M. Tanter, S. Catheline, and M. Fink, "Shear modulus imaging with 2-D transient elastography," IEEE Trans Ultrason Ferroelectr Freq Control, vol. 49, pp. 426-35, Apr 2002.

[7] M. Tanter, J. Bercoff, L. Sandrin, and M. Fink, "Ultrafast compound imaging for 2-D motion vector estimation: application to transient elastography," IEEE Trans Ultrason Ferroelectr Freq Control, vol. 49, pp. 1363-74, Oct 2002.

[8] T.-Y. Wang, T. L. Hall, Z. Xu, J. B. Fowlkes, and C. A. Cain, "Imaging Feedback of Histotripsy Treatments with Ultrasound Shear Wave Elasticity Imaging," (in preparation).

[9] J. E. Parsons, C. A. Cain, and J. B. Fowlkes, "Cost-effective assembly of a basic fiber-optic hydrophone for measurement of high-amplitude therapeutic ultrasound fields," J. Acoust. Soc. Am., vol. 119, pp. 1432-1440, Mar 2006.

[10] M. M. Burlew, E. L. Madsen, J. A. Zagzebski, R. A. Banjavic, and S. W. Sum, "A new ultrasound tissue-equivalent material," Radiology, vol. 134, pp. 517-20, Feb 1980.

[11] F. A. Duck, Physical properties of tissue : a comprehensive reference book. London: Academic, 1990.

[12] M. A. Lubinski, S. Y. Emelianov, and M. O'Donnell, "Speckle tracking methods for ultrasonic elasticity imaging using short-time correlation," IEEE Trans Ultrason Ferroelectr Freq Control, vol. 46, pp. 82-96, 1999.

[13] A. M. Lake, Z. Xu, J. E. Wilkinson, C. A. Cain, and W. W. Roberts, "Renal ablation by histotripsy--does it spare the collecting system?," J. Urol., vol. 179, pp. 1150-1154, Mar 2008.

[14] I. K. Holfort, F. Gran, and J. A. Jenson, "Plane wave medical ultrasound imaging using adaptive beamforming," Proc. IEEE Ultrason. Symp., pp. 288-292, Oct., 2008 2008.

[15] F. Kallel, R. J. Stafford, R. E. Price, R. Righetti, J. Ophir, and J. D. Hazle, "The feasibility of elastographic visualization of HIFU-induced thermal lesions in soft tissues," Ultrasound in Medicine & Biology, vol. 25, pp. 641-647, 1999.
[16] M. Fatemi and J. F. Greenleaf, "Probing the dynamics of tissue at low frequencies with the radiation force of ultrasound," Phys Med Biol, vol. 45, pp. 1449-64, Jun 2000.
[17] K. R. Nightingale, M. L. Palmeri, R. W. Nightingale, and G. E. Trahey, "On the feasibility of remote palpation using acoustic radiation force," J Acoust Soc Am, vol. 110, pp. 625-34, Jul 2001.
[18] F. L. Lizzi, R. Muratore, C. X. Deng, J. A. Ketterling, S. K. Alam, S. Mikaelian, and A. Kalisz, "Radiation-force technique to monitor lesions during ultrasonic therapy," Ultrasound Med Biol, vol. 29, pp. 1593-605, Nov 2003.
[19] M. F. Insana, C. Pellot-Barakat, M. Sridhar, and K. K. Lindfors, "Viscoelastic imaging of breast tumor microenvironment with ultrasound," J Mammary Gland Biol Neoplasia, vol. 9, pp. 393-404, Oct 2004.
[20] R. R. Bouchard, M. L. Palmeri, G. F. Pinton, G. E. Trahey, J. E. Streeter, and P. A. Dayton, "Optical tracking of acoustic radiation force impulse-induced dynamics in a tissue-mimicking phantom," J Acoust Soc Am, vol. 126, pp. 2733-45, Nov 2009.

CHAPTER VII. SUMMARY AND FUTURE WORK

7.1 Summary

This thesis demonstrates that histotripsy, a cavitation-based tissue fractionation process, can produce highly precise lesions with very high dose efficiently with appropriate manipulation of the cavitation nuclei distribution. Specifically, two innovative treatment strategies have been developed to provide better control of the lesion development process:

1) The first strategy produces highly confined lesions with a size smaller than the natural focal region using a focal zone sharpening technique which spatially controls of the bubble cloud generated by histotripsy. While damage in the periphery was suppressed, complete fractionation in the treatment center was achieved.
2) The second strategy produces complete and homogeneous tissue fractionation with passive removal of cavitation memories. Well-defined lesions with very few collateral damages can be obtained with dramatically fewer pulses.

The two treatment strategies have been validated both in RBC phantoms and in *ex vivo* tissues.

As homogeneous lesions can be produced, prediction of the clinical outcomes based on several ultrasound tissue characterization methods can be made without concerns about misleading metrics causing from inhomogeneous fractionation. Three specific imaging feedback approaches have been developed in this thesis.

1) Backscatter intensity analysis: Significant and exponential decrease in ultrasound backscatter intensity occurs in the treated tissue volume immediately after the treatment. The normalized ultrasound backscatter intensity can be quantitatively correlated with the percentage of the remaining intact cell nuclei examined via histology with a strong correlation coefficient.
2) Tissue elasticity imaging: The lesions can be distinguished with higher contrast and higher sensitivity on elasticity images rather than standard B-mode images. Significant and exponential decrease in the lesion elasticity can be measured with shear wave elasticity imaging. Strong correlation exists between the lesion elasticity and the percentage of the remaining intact cell nuclei examined via histology.
3) Shear displacement profile characterization: The temporal displacement profiles of the shear waves induced in the progressively fractionated volume changes significantly as the tissues are fractionated with increasing numbers of pulses. Such change can be easily detected with conventional ultrasound M-mode imaging nearly in real time. Quantitative measurements (i.e., the peak-to-peak displacements and the time to peak displacement) extracted from the temporal displacement profiles are strongly correlated with the percentage of the remaining intact cell nuclei examined via histology.

As the percentage of the remaining intact cell nuclei is directly related with the cell death, the degree of tissue fractionation, or other clinical outcomes, the feedback metrics developed here may be used as quantitative indicators of the treatment outcomes, i.e., when a tissue volume has been sufficiently treated. Such a feedback metric is highly desirable, if not essential, for any non-invasive surgical procedure.

7.2 Future Work

7.2.1 Robust and active control of cavitation nuclei

The two specific examples of histotripsy treatment control shown in this thesis imply more general and robust applications. For example, cavitation nuclei preconditioning is currently developed for protection of the peripheral region immediately surrounding the treatment center. This technique may be used for a more general application: active protection of an arbitrarily selected area. We may design special pulses to remove the cavitation nuclei in the selected area. This local area would likely have higher cavitation threshold, thus resistant to cavitational damage. The cavitation nuclei removing pulses can also be applied to actively remove the cavitation memories in the treatment volume. The nuclei removing pulses would be interleaved into the regular therapy pulse sequence. They would remove the residual memories immediately after each thereapy pulse. As soon as the cavitation memory is removed, the next therapy pulse can be delivered. Therefore, the time interval between successive pulses for the memory effect to disappear may be substantially reduced. The total treatment time would be significantly decreased.

Searching for the appropriate pulsing parameters may be difficult. Fortunately, recent studies about the inception mechanism of the bubble clouds [1] and computer simulation of the histotripsy bubble dynamics [2, 3] provide guidance for the potential acoustic parameters.

7.2.2 In vivo validation of imaging feedback metrics

The feedback methods developed in this thesis have been demonstrated in the *in vitro* setup, and should be validated for *in vivo* situations. In the *in vivo* situation, challenges may arise from degradation of the image quality, especially when the target organs are seated deeply in the body. Detecting the backscatter intensity change could be difficult due to the poor image contrast. Tracking the tissue displacement from the tissue speckle patterns may be difficult. In addition, challenges may also come from the biological responses that do not occur *in vitro*. For example, our experience in the *in vivo* experiments indicates that the backscatter reduction only persists for several minutes after the treatments. The backscatter intensity increases again when the blood flow and coagulate in the treatment volume. The time window during which backscatter intensity reduction can be measured may be short. These issues should be studied in the future.

7.3 References

[1] A. D. Maxwell, T. Y. Wang, C. A. Cain, J. B. Fowlkes, O. A. Sapozhnikov, M. R. Bailey, and Z. Xu, "Cavitation clouds created by shock scattering from bubbles during histotripsy," J. Acoust. Soc. Am., 2011 (in press).

[2] W. Kreider, M. R. Bailey, O. A. Sapozhnikov, V. A. Khokhlova, and L. A. Crum, "The dynamics of histotripsy bubbles," in Int. Symp. Therapeutic Ultrasound, Tokyo, Japan, 2010.

[3] A. D. Maxwell, C. A. Cain, J. B. Fowlkes, and Z. Xu, "Inception of Cavitation Clouds by Scattered Shockwaves," in Proc. IEEE Ultrason. Symp., 2010, pp. 108-111.